The Pennsylvania State University

The Graduate School

Materials Science and Engineering

PULSED LASER DEPOSITION OF xBiScO$_3$-(1-x)BaTiO$_3$ THIN FILMS FOR LEAD FREE DIELECTRIC APPLICATIONS

A Thesis in

Materials Science and Engineering

by

Daniel Scott Tinberg

© 2006 Daniel Scott Tinberg

Submitted in Partial Fulfillment
of the Requirements
for the Degree of

Master of Science

December 2006

I grant The Pennsylvania State University the non-exclusive right to use this work for the University's own purposes and to make single copies of the work available to the public on a not-for-profit basis if copies are not otherwise available.

Daniel Scott Tinberg

The thesis of Daniel S. Tinberg was reviewed and approved* by the following:

Susan Trolier-McKinstry
Professor of Ceramic Science and Engineering
Thesis Advisor

Clive A. Randall
Professor of Materials Science and Engineering

Ian M. Reaney
Professor of Engineering Materials
The University of Sheffield
Special Signatory

James P. Runt
Chair, Intercollege Graduate Degree Program in
Materials Science and Engineering
Professor of Polymer Science

*Signatures are on file in the Graduate School.

We approve the thesis of Daniel Scott Tinberg.

Date of Signature

_________________________ _______________

Susan Trolier-McKinstry
Professor of Ceramic Science and Engineering
Thesis Advisor

_________________________ _______________

Clive A. Randall
Professor of Materials Science and Engineering

_________________________ _______________

Ian M. Reaney
Professor of Engineering Materials
The University of Sheffield

_________________________ _______________

James P. Runt
Chair, Intercollege Graduate Degree Program in
Materials Science and Engineering
Professor of Polymer Science

Abstract

The field of high volumetric efficiency capacitors is dominated by ferroelectric materials such as $BaTiO_3$ due to the large temperature-stable permittivities that are shown over a wide frequency range. In thin films, lead-based ferroelectrics have found significant use in non-volatile memory and piezoelectric applications. The large size, high polarizability, and lone pair electrons of the Pb^{2+} cation leads to high permittivity and piezoelectric constants. However, there are toxicity and environmental concerns implicit in processing of lead-based perovskites. The development of $BiScO_3$-$PbTiO_3$ and its high room temperature permittivity and piezoelectric responses suggests that reduced lead compositions which are Bi-based may provide high polarizabilities in both bulk and in thin film form. To this end, a lead-free system based on $BiScO_3$-$BaTiO_3$ was predicted, based on a tolerance factor approach, to show a morphotropic phase boundary in the system, which should enhance the polarizability.

To verify this prediction, pulsed laser deposition was used to grow $xBiScO_3$-$(1-x)BaTiO_3$ thin films on (100) $SrRuO_3/LaAlO_3$ and Pt-coated Si substrates. Pulsed laser deposition was chosen because it allowed the film composition to be changed readily. The deposition parameters were studied to determine the effect on perovskite phase formation. It was found that the perovskite structure was stable for compositions of x=0.2-0.6 in epitaxial films, with a reduced stability range in polycrystalline films. From lattice parameter measurements, the morphotropic phase boundary occurred at x ~0.4.

The film permittivity was investigated as a function of frequency, dc bias and temperature. An increase in permittivity found at a composition of x~0.4-0.45, which corresponds to the location of the morphotropic phase boundary. All films showed some measure of frequency dependence, with increasing dispersion seen for increasing $BiScO_3$ concentrations. All films showed a broad permittivity maximum with temperature, with a value of ~800 occurring over a 100°C temperature range at the morphotropic phase boundary. Additionally, the permittivity at the morphotropic phase boundary was shown to decrease by a factor of 2 as the thickness dropped from ~600 nm to ~50 nm. An analysis of the inverse capacitance as a function of thickness shows that this decrease can be partially attributed to an effective interfacial layer. Lastly, at high fields, the films showed a finite hysteresis, with a room temperature remanent polarization of ~9 $\mu C/cm^2$ for fields in excess of 1 MV/cm.

Table of Contents

List of Figures vii
List of Tables xii
Acknowledgements xiii
1.0 Introduction 1
1.1 Applications of Dielectric Thin Films 1
1.2 Objective of the Thesis 2
2.0 Literature Review 4
2.1 Dielectric Materials 4
2.1.1 Ferroelectric Phenomena 9
2.1.2 Permittivity of Ferroelectric Thin Films Compared to Bulk Materials 15
2.2 Examples of Dielectric Materials 22
2.2.1 The Perovskite Structure 22
2.2.2 Morphotropic Phase Boundaries 24
2.2.3 Bismuth Doped Perovskites 28
2.2.4 Bismuth Based Perovskites 29
2.3 Physical Vapor Deposition 30
2.3.1 Evaporation 31
2.3.2 Sputtering 32
2.3.3 Pulsed Laser Deposition 33
2.4 Thin Film Growth 38
2.4.1 Epitaxial Growth 40
2.4.2 Polycrystalline Growth 42
2.4.3 Stress Development in Thin Films 45
2.4.4 Thin Film Characterization 47
3.0 Experimental Procedure 51
3.1 Compositions of Interest 51
3.2 Target Preparation 53
3.3 Vacuum System 54
3.4 Pulsed Laser Deposition of $xBiScO_3$-$(1-x)BaTiO_3$ Thin Films 57
3.5 Structural Characterization 59
3.5.1 2-Circle X-Ray Diffraction 59
3.5.2 4-Circle X-Ray Diffraction 59
3.6 Morphological Characterization 61
3.7 Electrical Property Measurements 61
4.0 Results and Discussion 65
4.1 X-ray Characterization of $xBiScO_3$-$(1-x)BaTiO_3$ Thin Films 65
4.1.1 $SrRuO_3$ Deposition and $xBiScO_3$-$(1-x)BaTiO_3$ Perovskite Phase Formation 65
4.1.2 Lattice Parameter Analysis 71
4.1.3 Deposition Parameter Study 73
4.1.4 Thickness Dependence Study 84
4.2 Dielectric Properties of $xBiScO_3$-$(1-x)BaTiO_3$ Thin Films 88
4.2.1 Dielectric Properties vs. Film Composition 89
4.2.2 Dielectric Properties vs. Film Thickness 102

4.3 Dielectric Hysteresis of $xBiScO_3$-(1-x)$BaTiO_3$ Thin Films 106
5.0 Conclusions and Recommendations for Future Work 111
5.1 Summary and Conclusions 111
5.2 Future Work 112
5.2.1 Increasing the Remanent Polarization 112
5.2.2 Alternative Bismuth Perovskites 114
6.0 References 116

List of Figures

Fig. 2.1. Polarization descriptions for different polarization mechanisms. (a) electronic, (b) ionic, (c) dipolar and (d) space charge polarizability. After von Hippel [16]. 5

Fig. 2.2. Schematic of ε' and ε'' as a function of frequency [15]. 7

Fig. 2.3. Polarization response for paraelectric and ferroelectric materials. 9

Fig. 2.4. Permittivity vs. temperature for $BaTiO_3$. After Smolenskii [18]. 10

Fig. 2.5. Schematic of (a) 180° and (b) non-180° domain walls, where the arrows denote the direction of the spontaneous polarization. 11

Fig. 2.6. RMS Polarization and permittivity vs. temperature for (a) normal ferroelectric undergoing a first order phase transition, (b) normal ferroelectric undergoing a second order phase transition, and (c) relaxor ferroelectric [28]. 12

Fig. 2.7. (a) Permittivity vs. temperature and (b) Vogel-Fulcher analysis for $Pb(Sc_{1/2},Ta_{1/2})O_3$ [29]. 13

Fig. 2.8. Polarization hysteresis loops for $Pb(Mg_{1/3}Nb_{2/3})O_3$ with increasing temperature [30]. 14

Fig. 2.9. Permittivity vs. temperature for $(Ba_{0.7},Sr_{0.3})TiO_3$ in bulk and thin film form [12]. 15

Fig. 2.10. Dielectric constant of $BaTiO_3$ as a function of hydrostatic pressure for different temperatures [1]. 16

Fig. 2.11. Phase diagram for $SrTiO_3$ showing how in-plane strain can induce a ferroelectric phase in incipient ferroelectric material [34]. 17

Fig. 2.12. Permittivity vs. grain size for bulk $BaTiO_3$. Circles represent bulk grain size and triangles represent thin film data. After Shaw et al. [12]. 18

Fig. 2.13. Permittivity vs. temperature of $Ba_{0.7}Sr_{0.3}TiO_3$ thin films on Pt-coated Si plotted for different thicknesses [35]. 19

Fig. 2.14. (a) Schematic of the interface model and (b) inverse capacitance density vs. thickness plotted for different temperatures for $Ba_{0.7}Sr_{0.3}TiO_3$ films [12]. 21

Fig. 2.15. (a) Permittivity vs. temperature and (b) temperature coefficient of capacitance as a function of firing temperature for bismuth zinc niobate thin films [42]. 22

Fig. 2.16. Schematic of cubic perovskite unit cell along with tetragonal and rhombohedral ferroelectric distortions of the perovskite unit cell. 23

Fig. 2.17 Schematic of polarization directions for cubic (none), tetragonal (<001> directions), and rhombohedral perovskite systems (<111> directions). 25

Fig. 2.18 (a) Phase diagram for PZT and (b) room temperature permittivity as a function of composition. P_C is the prototype cubic perovskite phase, F_T, F_R, F_M are the ferroelectric tetragonal, rhombohedral (high temperature HT and low temperature LT) and monoclinic, phases respectively and A_O is the antiferroelectric orthorhombic phase. After Jaffe, Cook, and Jaffe [44] and Noheda [49]. 26

Fig. 2.19. Permittivity vs. temperature for (a) bulk and (b) thin film $BiScO_3$-$PbTiO_3$ at the MPB [9, 51]. 28
Fig. 2.20 Variation of the transition temperature as a function of composition for $Ba_{1-x}Bi_{2x/3}TiO_3$ ceramics [55]. 29
Fig. 2.21. Schematic of sputter deposition. After Smith [74]. 33
Fig. 2.22. Schematic of a pulsed laser deposition system 34
Fig. 2.23. Schematic of thermal cycle during a laser strike on the target [78]. (a) absorption of the laser radiation, (b) propagation of melt front and evaporation of material, (c) recoil of thermal shockwave and (d) solidification of the surface. 35
Fig. 2.24. Time lapsed CCD images of laser plume expanding into vacuum (a-f) and 100 mTorr O_2 (g-j) [79]. 37
Fig. 2.25. Schematic of particulate generation in pulsed laser deposition. 38
Fig. 2.26. Schematic of (a) Frank-Van der Merwe growth, (b) ideal step flow growth, (c) Volmer-Weber growth and (d) Stranski-Krastanov growth. The dark circles in (a) and (b) represent vapor deposited atoms. After Smith [74] 39
Fig. 2.27. Schematic of misfit dislocations in epitaxial films [74]. 41
Fig. 2.28. Schematic of the four zones of thin film growth [74]. 42
Fig. 2.29. Composite structure zone model for polycrystalline films [75]. 43
Fig. 2.30. Schematic of ion bombardment on growing films showing (a) resputtering, (b) forward sputtering, and (c) implantation. After Smith [74]. 45
Fig. 2.31. Schematic of lattice mismatch between film and substrate (a) film and substrate lattices prior to deposition, (b) film lattice constrained to substrate, and (c) misfit dislocation relieving stress in the film. After Smith [74]. 46
Fig. 2.32. Schematic of a common x-ray diffraction setup. 49
Fig. 2.33. Schematic of mosaic tilt in a thin film. 50
Fig. 3.1. Calculated tolerance factor for the $x$$BiScO_3$-(1-$x$) $BaTiO_3$ system. 52
Fig. 3.2. X-ray diffraction pattern from a $0.4BiScO_3$-$0.6BaTiO_3$ target showing multiple phases present. 54
Fig. 3.3. Schematic of pulsed laser deposition setup used for these experiments [80]. 55
Fig. 3.4. Schematic of heater block used in this project. 56
Fig. 3.5. Schematic of a typical 4-circle x-ray diffractometer setup. 60
Fig. 3.6. Schematic of thin film capacitors used in this study. 62
Fig. 4.1. X-ray diffraction pattern for $SrRuO_3$ deposited on $LaAlO_3$. Here and throughout the chapter, unless otherwise noted, all perovskite peaks are indexed in terms of a pseudocubic unit cell. 66
Fig. 4.2 X-ray diffraction patterns for $0.2BiScO_3$-$0.8BaTiO_3$ (BSBT) on $SrRuO_3/LaAlO_3$. (a) θ-2θ scan of the 100 peaks and (b) ϕ scan of 101 peaks showing 4 fold symmetry characteristic of in-plane alignment. 67
Fig. 4.3. a) Compilation of x-ray patterns for $x$$BiScO_3$-(1-$x$)$BaTiO_3$ on 68

(100)$SrRuO_3$/$LaAlO_3$ and b) 101 ϕ scan for $0.6BiScO_3$-$0.4BaTiO_3$ thin film.
Fig. 4.4. (a) 0.2 $BiScO_3$-$BaTiO_3$ on Pt-coated Si. The $W_{L\alpha}$ line is due to contamination of the Cu x-ray source from the W filament. (b) compilation of x-ray patterns for $x$$BiScO_3$-(1-$x$)$BaTiO_3$ films with x= 0.2-0.6 on Pt-coated Si. Starred peaks correspond to a second phase. 69
Fig. 4.5. Scanning electron micrographs illustrating the difference in morphology of the polycrystalline ((a) and (c)) vs. epitaxial films ((b) and (d)). 70
Fig. 4.6. X-ray diffraction patterns for a $0.4BiScO_3$-$0.6BaTiO_3$ film (triangles) deposited at 700°C and 100 mTorr O_2/O_3 on $SrRuO_3$/$LaAlO_3$ (squares/circles). (a) 100 family and (b) 101 family of planes and FWHM for the (c) 200 peak and (d) 101 peak. Starred peaks stem from the substrate holder. 71
Fig. 4.7. Nelson-Riley plots for epitaxial $0.4BiScO_3$-$0.6BaTiO_3$ films deposited at 700°C and 100 mTorr O_2/O_3 (a) 100 family and (b) 101 family of planes. 72
Fig. 4.8. X-ray diffraction patterns for $0.4BiScO_3$-$0.6BaTiO_3$ as a function of substrate temperature on (a) $SrRuO_3$/$LaAlO_3$ and (b) Pt-coated Si. 74
Fig. 4.9. Out-of-plane lattice parameter as a function of substrate temperature for epitaxial $0.4BiScO_3$-$0.6BaTiO_3$ thin films deposited at an ambient pressure of 100 mTorr O_2/O_3 and a target-substrate distance of 8 cm. 76
Fig. 4.10. Scanning electron micrograph of the surface of $0.4BiScO_3$-$0.6BaTiO_3$/SRO/LAO thin films as a function of deposition temperature. Particles on the surface were used to facilitate focusing. 77
Fig. 4.11. (a) Out of plane lattice parameter as a function of chamber pressure for a $0.4BiScO_3$-$0.6BaTiO_3$ thin film deposited at 700°C and (b) Full-Width at Half Maximum (FWHM) for $0.4BiScO_3$-$0.6BaTiO_3$ films deposited at 700°C at various chamber pressures. 78
Fig. 4.12. Scanning electron microscope images of the surface of $0.4BiScO_3$-$0.6BaTiO_3$/SRO/LAO thin films as a function of deposition pressure. 80
Fig. 4.13. Measured lattice parameter as a function of composition for films deposited at 700°C and 100 mTorr O_2/O_3. End member lattice parameters were taken from Maria [43] and Inaguma [47]. 81
Fig. 4.14. FWHM for different composition of films deposited at 700°C and 100 mTorr O_2/O_3. 82
Fig. 4.15. Scanning electron micrographs of x$BiScO_3$-(1-x)$BaTiO_3$ on thin films deposited on SRO/LAO at 700°C and 100 mTorr O_2/O_3. 83
Fig. 4.16. Unit cell volume as a function of composition for $x$$BiScO_3$-(1-$x$)$BaTiO_3$ thin films. The solid line represents Vegard's Law. End member lattice parameters were taken from Maria [43] and Inaguma [47]. 84
Fig. 4.17. Thickness as a function of deposition time for $0.4BiScO_3$-$0.6BaTiO_3$ thin films. 85
Fig. 4.18. (a) Lattice parameters and (b) unit cell volume as a function of thickness for $0.4BiScO_3$-$0.6BaTiO_3$ thin films. 86

Fig. 4.19. Scanning electron micrographs as a function of thickness for $0.4BiScO_3$-$0.6BaTiO_3$/SRO/LAO thin films deposited at 700°C and 100 mTorr O_2/O_3 88
Fig. 4.20. Optical microscope image of top electrodes used in this thesis. 89
Fig. 4.21. (a) Permittivity vs. frequency for a $0.4BiScO_3$-$0.6BaTiO_3$ /SRO/LAO thin film and (b) $\varepsilon_r(f)/\varepsilon_r$(1 kHz) vs. frequency showing increasing frequency dependence with increasing $BiScO_3$ concentration. 90
Fig. 4.22. (a) Permittivity vs. temperature for a $0.4BiScO_3$-$0.6BaTiO_3$/ SRO/LAO thin film at various frequencies and (b) T_{Max} $xBiScO_3$-(1-x)$BaTiO_3$/SRO/LAO thin films at 10 kHz. 91
Fig. 4.23 Permittivity as a function of temperature and at different frequencies for $x$$BiScO_3$-(1-$x$)$BaTiO_3$/SRO/LAO thin films. (a) x=0.2, (b) x=0.35, (c) x=0.4, (d) x=0.45, and (e) x=0.6 for frequencies ranging from 100 Hz to 1 MHz. 92
Fig. 4.24. Loss tangent as a function of temperature measured at different frequencies for $x$$BiScO_3$-(1-$x$)$BaTiO_3$/SRO/LAO thin films. (a) x=0.2, (b) x=0.35, (c) x=0.4, (d) x=0.45, and (e) x=0.6 for frequencies ranging from 100 Hz to 1 MHz. 93
Fig. 4.25. Resistivity of a $0.4BiScO_3$-$0.6BaTiO_3$/SRO/LAO thin film as a function of 1/T. 95
Fig. 4.26. Permittivity and loss tangent at 10 kHz as a function of composition for $x$$BiScO_3$-(1-$x$)$BaTiO_3$ thin films with thicknesses around 100 nm at varying temperatures. 96
Fig. 4.27. Phenomenologically derived values for permittivity and the Curie constant of $Pb(Zr_{1-x}Ti_x)O_3$ as a function of composition at a temperature of 600°C. Equations taken from Haun [109]. 97
Fig. 4.28 Plot of natural log of the relaxation time as a function of T_m for a $0.4BiScO_3$-$0.6BaTiO_3$/SRO/LAO thin film. Solid line is the Vogel-Fulcher fit to the data. 99
Fig. 4.29. Vogel-Fulcher fitting parameters as a function of composition (a) activation energy, E_a, (b) relaxation time τ_o, (c) characteristic temperature, T_f, and (d) the T_m in the loss data at 10 kHz. 100
Fig. 4.30. Relaxation time for various compositions within the PMN-PT system [110]. 102
Fig. 4.31. Permittivity and loss tangent as a function of thickness for $0.4BiScO_3$-$0.6BaTiO_3$ thin films. 103
Fig. 4.32. Inverse of the capacitance density as a function of thickness for a $0.4BiScO_3$-$0.6BaTiO_3$ thin film. 104
Fig. 4.33. Permittivity and loss tangent as a function of DC bias field for a $0.4BiScO_3$-$0.6BaTiO_3$/SRO/LAO thin film. 106
Fig. 4.34. Polarization hysteresis loop for a $0.4BiScO_3$-$0.6BaTiO_3$ thin film on (100) $SrRuO_3/LaAlO_3$. 107
Fig. 4.35. (a) Remanent polarization and (b) coercive field as a function of temperature for a $0.4BiScO_3$-$0.6BaTiO_3$/SRO/LAO thin film. 108
Fig. 4.36. Hysteresis loops for $0.2BiScO_3$-$0.8BaTiO_3$/SRO/LAO measured at -175°C under different electric fields 109

Fig. 4.37. Hysteresis loops for $xBiScO_3$-(1-x)$BaTiO_3$/SRO/LAO measured at -175 °C. 110
Fig. 5.1 Polarization hysteresis loops for $PbZr_{0.4}Ti_{0.6}O_3$ on MgO (α_T= 13 ppm/°C), Al_2O_3 (α_T =7.4 ppm/°C) and Si (α_T= 4 ppm/°C)three different substrates showing the effect of stress on remanent polarization [125]. 113
Fig. 5.2. X X-ray diffraction pattern for a $0.9BiAlO_3$-$0.1PbTiO_3$ thin film on (100) $LaAlO_3$. Circles represent film peaks. 115

List of Tables

Table 2.1. Tolerance Factor and Crystal Structure for Selected Perovskites. 24
Table 2.2. Selected Properties of Bismuth-Containing Perovskites Thin Films. 30
Table 3.1. Ionic Radii Used for Tolerance Factor Calculations. 51
Table 3.2. List of Deposition Parameters Used in the Study. 58
Table 4.1 τ_o values for several different compositions of perovskites. 101

Acknowledgements

I would like to thank my advisor, Dr. Susan Trolier-McKinstry, for giving me the opportunity to work in her group. It has been a pleasure to study under her and every discussion is valuable. I want to thank all the members of the STM group for their help over the past two years. In particular, I would like to thank Junling Wang and Srowthi S.N. Bharadwaja for their assistance on the pulsed laser deposition system. My thanks go out to the staff at MRL for their valuable assistance whenever it was needed. My appreciation goes out towards Dr. Rich Eitel and Craig Stringer for their useful advice, numerous discussions and well-timed distractions. Lastly, I need to thank my parents, Ted and Jan Tinberg, for teaching me the value of an education, and for their constant support and encouragement.

1.0 Introduction

This chapter outlines the thesis. The uses of dielectric thin films as well as the movement towards Pb-free films are discussed. Lastly, the objectives of the thesis are stated.

1.1 Applications of Dielectric Thin Films

Dielectric thin films have found a variety of uses in both dynamic and non-volatile memories [1-3], decoupling capacitors, and embedded capacitors [4, 5]. For applications requiring high capacitance, ferroelectrics are useful because they often have large permittivities as well as large remanent polarizations. Thus, most multilayer capacitors are based on ferroelectric $BaTiO_3$. For thin film ferroelectrics, lead containing compositions have found significant use in ferroelectric random access memories and in piezoelectric applications [6]. However due to the toxicity of lead, processing and disposal of lead-based electronics raises concerns [7]. Thus, there is interest in exploring lead-free and lead-reduced compounds in theses applications. For example, development of lead-reduced morphotropic phase boundary ceramics (particularly those involving bismuth) have received much attention lately [8, 9].

For bulk capacitors, use of lead-containing ferroelectrics is discouraged [10, 11]. $BaTiO_3$-based materials, including modified $BaTiO_3$, $(Ba_{1-x}Sr_x)TiO_3$, and $Ba(Ti_{1-x}Zr_x)O_3$ are widely utilized. In following this approach, $(Ba_{1-x}Sr_x)TiO_3$ (BST) thin films have been explored. Unfortunately, however, BST thin films processed at temperatures $\leq 800°C$ (which is typical for films on Si) have substantially lower permittivities than

those of bulk materials of the same composition. Moreover, the permittivity is a strong function of thickness due to a combination of size effects and effective interfacial layers [12]. This has led to the development of new morphotropic phase boundary systems which should enhance permittivities even at small thicknesses. Thus, there is interest in being able to enhance the permittivity of lead-free thin film dielectrics, particularly at small film thicknesses. The approach adopted in this work is to explore $BaTiO_3$-based morphotropic phase boundaries.

1.2 Objective of the Thesis

The purpose of this thesis is twofold:

1) To investigate the deposition parameters needed to produce single phase perovskite thin films of $x\mathrm{BiScO_3}$-$(1-x)\mathrm{BaTiO_3}$. Pulsed laser deposition was chosen as the deposition technique because it allowed the film composition to be changed readily. This study focused on investigating the effects of substrate temperature, deposition pressure, and film composition on the crystal quality of the film. X-ray diffraction was used to determine how various deposition conditions affected the lattice parameters of the films. Additionally, structural indications for the location of the morphotropic phase boundary in the $x\mathrm{BiScO_3}$-$(1-x)\mathrm{BaTiO_3}$ were sought.

2) Characterization of the dielectric properties of $x\mathrm{BiScO_3}$-$(1-x)\mathrm{BaTiO_3}$ thin films. Measurements were performed to determine the effects of frequency and DC bias. Permittivity measurements as a function of temperature were performed to investigate the transition temperature of the films. Through dielectric measurements as a function of composition, the location of the morphotropic phase boundary was confirmed. Lastly,

the thickness dependence on permittivity was investigated to determine if the lone pair electrons on the Bi^{3+} ion stabilize the permittivity to smaller thicknesses.

2.0 Literature Review

The chapter reviews dielectric materials of interest for capacitors and their properties in both bulk and thin film form. An overview of physical vapor deposition techniques, thin film growth, and thin film characterization is discussed.

2.1 Dielectric Materials

A dielectric material is an electrical insulator. When an electric field $\vec{E}$ is applied to a dielectric, the material polarizes, developing a dielectric displacement $\vec{D}$ [13]. The total dielectric displacement of a material comes from orientation of dipoles as well as creation of dipoles due to the displacement of space charges, ions and electrons in a material [14]. A schematic of the possible polarization mechanisms is shown in Fig. 2.1. The dielectric displacement of a material is defined in equation 2.1;

$$\vec{D} = \varepsilon_o \vec{E} + \vec{P}_t \quad (2.1),$$

where $\vec{P}_t$ is the total polarization of the material and ε_o is the permittivity of free space. The total polarization of the material, a sum of the polarizations due to the electronic, ionic, space charge and dipoles in the material is given by equation 2.2;

$$\vec{P}_t = \varepsilon_o \varepsilon_r \vec{E} + \vec{P}_s \quad (2.2),$$

where ε_r is the relative permittivity and $\vec{P}_s$ is the spontaneous polarization (which is non-zero in pyroelectric materials). Combining these two equations, the total dielectric response of a material can be described as:

$$\vec{D} = \varepsilon_o (1 + \varepsilon_r) \vec{E} + \vec{P}_s = \varepsilon_o \chi \vec{E} + \vec{P}_s \quad (2.3).$$

where χ is the dielectric susceptibility.

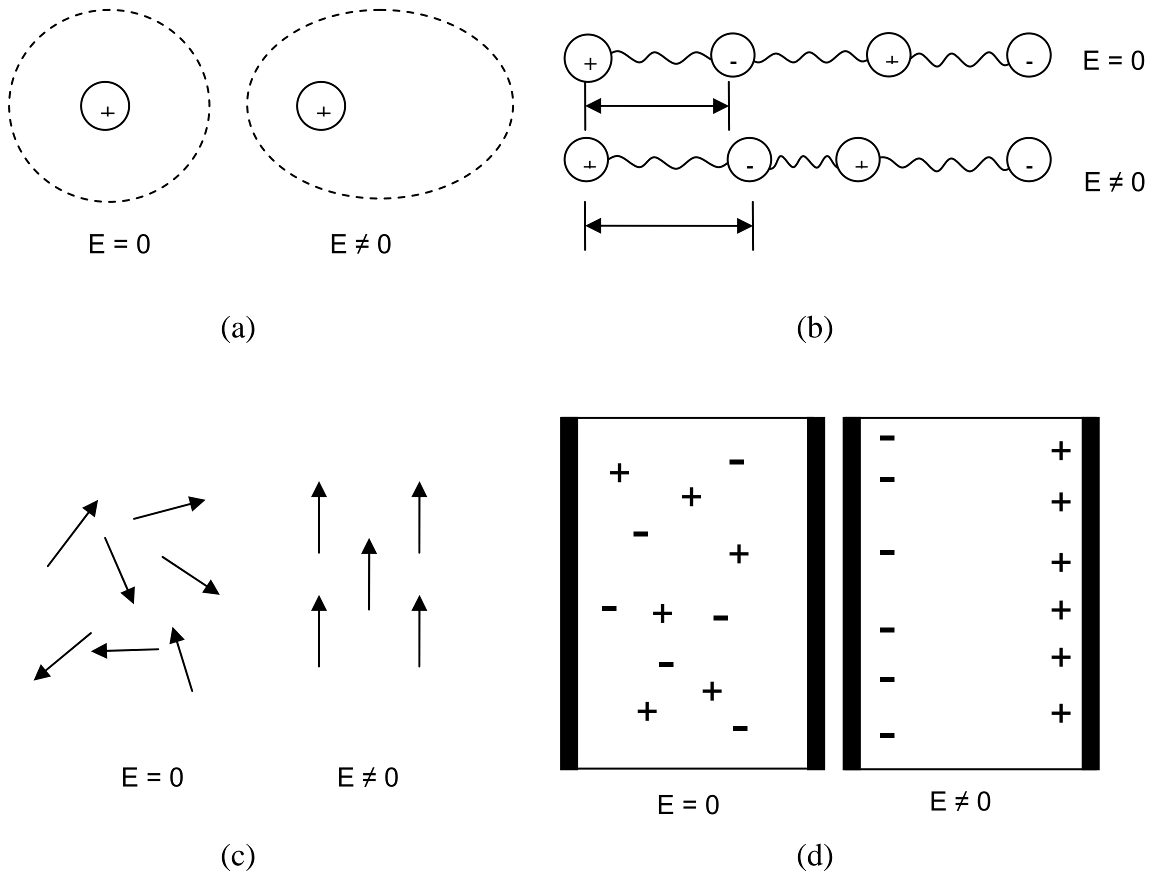

Fig. 2.1. Polarization descriptions for different polarization mechanisms. (a) electronic, (b) ionic, (c) dipolar and (d) space charge polarizability. After von Hippel [15].

For capacitor applications, high permittivity, temperature-stable materials with low loss tangents are desired [2]. It is important to recognize that ε_r is a complex quantity which can be written as;

$$\varepsilon^* = \varepsilon' - j\varepsilon'' \quad (2.4),$$

where ε^* is the complex permittivity, ε' and ε'' are the real and imaginary contributions to permittivity and j is the $\sqrt{-1}$ [14]. The loss tangent of the material is related to the real and imaginary parts of the complex permittivity as described in equation 2.5;

$$\tan\delta = \frac{\varepsilon''}{\varepsilon'} \quad (2.5),$$

where $\tan\delta$ is the loss tangent.

The permittivity of a material often shows a strong frequency dependence when measured from 1 Hz to 10^{15} Hz. This is due to the response of the four polarization mechanisms mentioned earlier. When an alternating field is applied, the polarization mechanisms respond as governed by equation 2.2. However, when the frequency becomes too high for space charges to follow, the total polarization of the material is reduced and the material is said to undergo a dielectric relaxation [16]. The imaginary part of permittivity is increased at the dielectric relaxation frequency because the polarization response lags behind the field, thus causing an increase in the loss. Likewise, as the frequency is increased, other polarization mechanisms can no longer follow the electric field. A schematic of the dielectric dispersion and the correlated loss peaks is shown in Fig. 2.2.

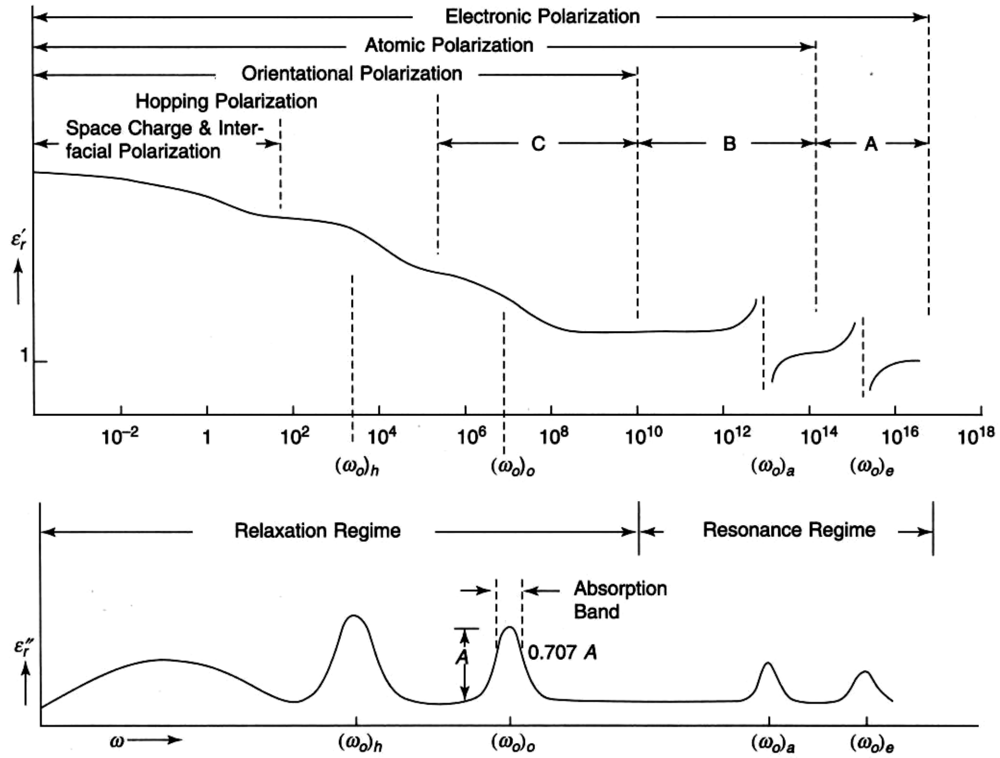

Fig. 2.2. Schematic of ε' and ε'' as a function of frequency [14].

When a material is electronically polarized, the electron clouds surrounding the nuclei are displaced, creating a dipole between the center of positive charge in the atomic nucleus and the net center of negative charge of the electron cloud. When the electric field is removed, the cloud moves back to its equilibrium position and no net dipole moment is typically observed [14]. The loss peaks shown in Fig. 2.2 are directly linked to the time constants associated with the relaxation or resonance in the material.

For capacitor applications, there is frequently a trade-off between the achievable permittivity and its temperature dependence. Dielectrics with low to moderate permittivities primarily exhibit ionic and electronic polarizabilities. Paraelectric

materials with higher permittivities occur above a ferroelectric-paraelectric transition. Paraelectric materials often exhibit non-linear, non-hysteretic dielectric behavior with increasing electric field.

Ferroelectric materials have a spontaneous polarization which can be switched between crystallographically defined equilibrium states by a realizable electric field. Many ferroelectrics have high permittivities. Ferroelectric materials exhibit non-linear, hysteretic dielectric responses to electric fields, with a non-zero polarization at zero applied electric field [1]. A schematic of the polarization response of paraelectric and ferroelectric materials is given in Fig. 2.3. A ferroelectric hysteresis loop has several notable features including a remanent polarization (the vertical intercept on the graph) which is the polarization left after a sufficiently large field is removed, and a coercive field (the horizontal intercepts on the graph) which is the electric field at which the net polarization is zero.

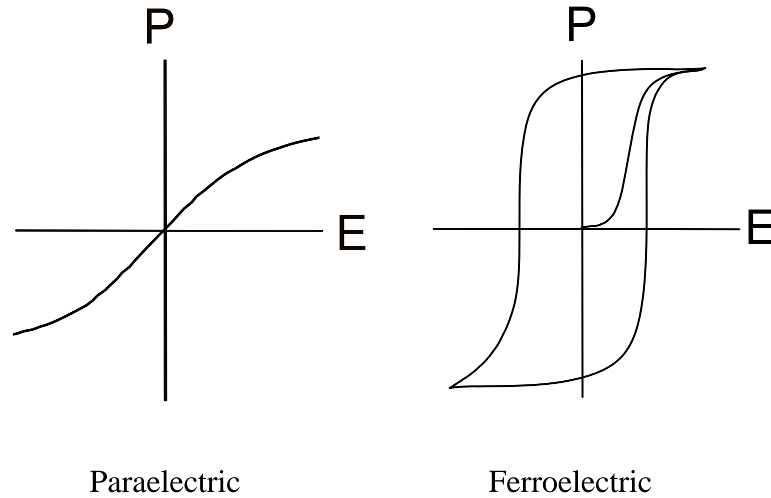

Paraelectric Ferroelectric

Fig. 2.3. Polarization response for paraelectric and ferroelectric materials.

2.1.1 Ferroelectric Phenomena

Ferroelectric phenomena exist in two different types of materials. The first type develops ferroelectricity from an order-disorder transition, where local dipoles exist both above and below the transition temperature [1, 17]. Above T_C, the dipoles are randomized so that no net P_S exists; below the transition temperature the local dipoles order over long length scales and produce a finite spontaneous polarization. The second family is the displacive ferroelectrics. Here there is a paraelectric prototype state that can be defined with no net polarization. In displacive ferroelectrics, ferroelectricity develops when there is a collective displacements of atoms (e.g. by off-centering of ions from a high symmetry position) inducing a dipole moment [13].

For normal ferroelectrics, the permittivity values do not depend much on frequency below 1 GHz; they are, however, a strong function of temperature. Peaks in the dielectric constant also occur at polymorphic phase transitions in a material such as in $BaTiO_3$ (shown in Fig. 2.4) [1]. The temperature at which the ferroelectric transforms to a prototype state is called the Curie temperature, T_C, and permittivities upwards of 10,000 can be obtained [1, 17, 18].

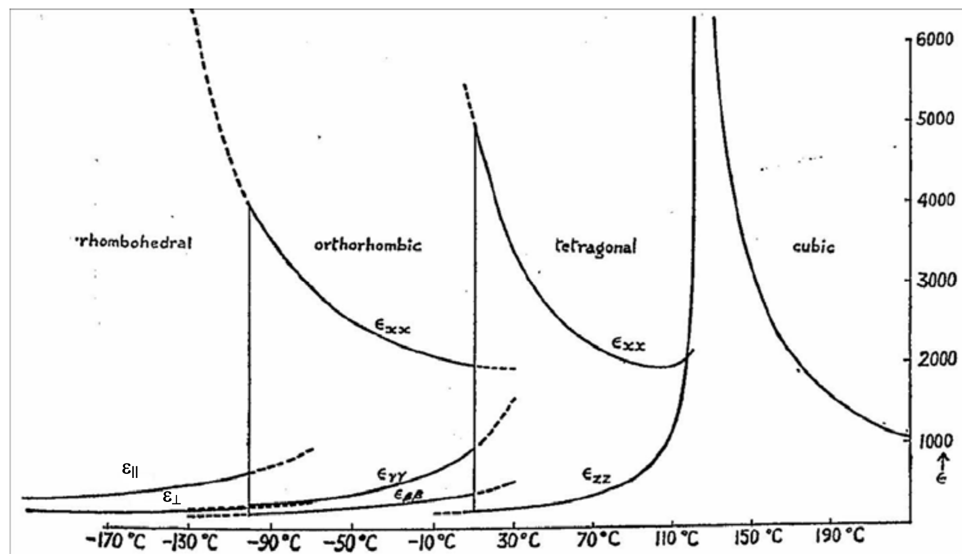

Fig. 2.4. Permittivity vs. temperature for $BaTiO_3$. After Smolenskii [18].

At temperatures below the Curie temperature, a domain structure will form due to availability of multiple possible polarization directions [1, 17, 18]. A domain is a region of material which possesses a uniform (or at least nearly so) polarization. A domain wall is a boundary between regions with different polarization directions. The number and orientation of the allowed polarization directions can be determined based on the symmetry elements lost on the transition from the prototype phase to the ferroelectric

one. The two types of domain walls are a) 180° domain walls where the polarization directions of the domains are antiparallel and b) non-180° domain walls, where the two polarizations differ by another angle. Motion of both 180° and non-180° domain walls contributes to the observed dielectric properties of ferroelectrics [1].

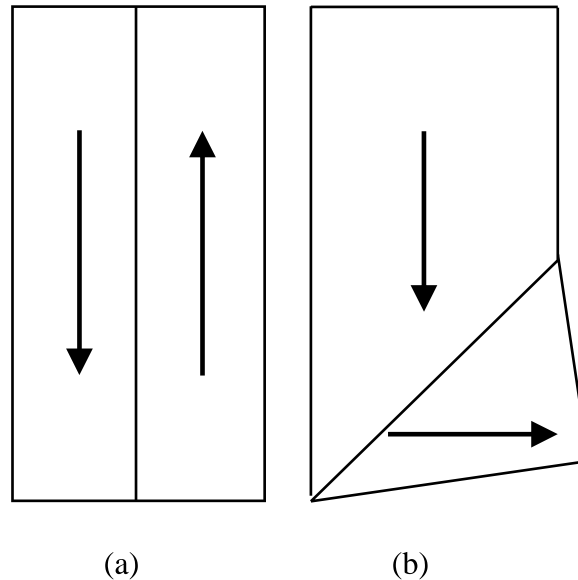

Fig. 2.5. Schematic of (a) 180° and (b) non-180° domain walls, where the arrows denote the direction of the spontaneous polarization.

Relaxor ferroelectrics differ from normal ferroelectrics in several ways, one of which is the strong frequency dependence in the permittivity values at temperatures below the maximum permittivity (see Fig. 2.7) [19-21]. Additionally, from measurements of the refractive index or the electrostrictive strain, a root-mean-square polarization is found to exist well beyond the observed T_{Max} up to a temperature $T_{D,}$ the

Burn's temperature, as shown in Fig. 2.6 [20, 22]. Relaxor ferroelectrics, near T_{Max} are characterized by nano-regions of polar material. The distribution in time constants associated with the polarization reorientation of these nano-regions (or their boundary motion), leads to the dispersion in the frequency spectrum. While numerous studies have attributed frequency dispersion to these nano-polar regions [19-21, 23, 24], the polarization mechanism in relaxors has been the subject of debate [23-26]. Physical models of the polarization mechanism vary from polar-vector reorientation in the superparaelectric model [27], to an expansion and contraction of the polar regions [26]. These models give an initial description of how the nano-polar regions can produce the large polarization response to the electric field [26, 27].

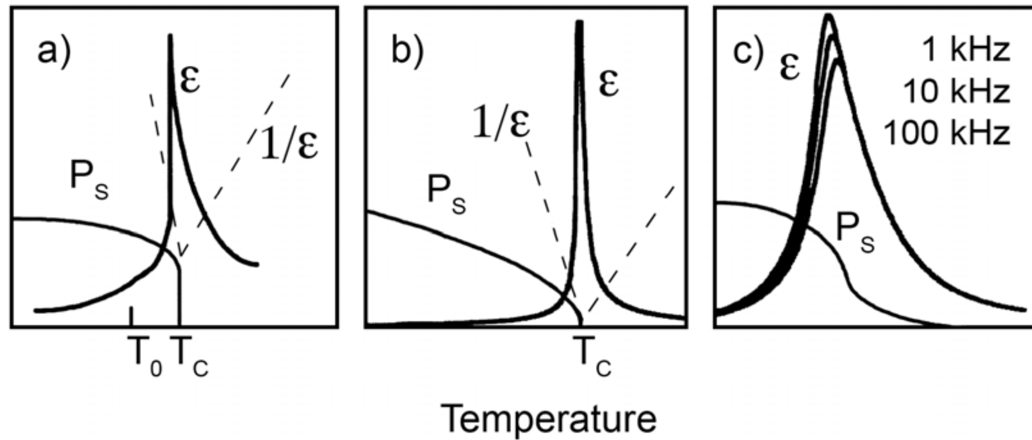

Fig. 2.6. RMS Polarization and permittivity vs. temperature for (a) normal ferroelectric undergoing a first order phase transition, (b) normal ferroelectric undergoing a second order phase transition, and (b) relaxor ferroelectric [28].

As mentioned previously, a characteristic feature of relaxor ferroelectrics is large frequency dispersion of the dielectric permittivity compared with that of normal ferroelectrics. It has been found in many cases that the degree of cation ordering on one or more crystallographic sites influences relaxor character. $Pb(Sc_{1/2},Ta_{1/2})O_3$, for example, exhibits both normal and relaxor ferroelectricity. As can be seen from Fig. 2.7, the frequency dispersion of the material decreases with increasing Sc:Ta order (given by the S parameter in the graph; higher S corresponds to more ordering) [29]. This results in processing parameters influencing the measured response of relaxor ferroelectrics.

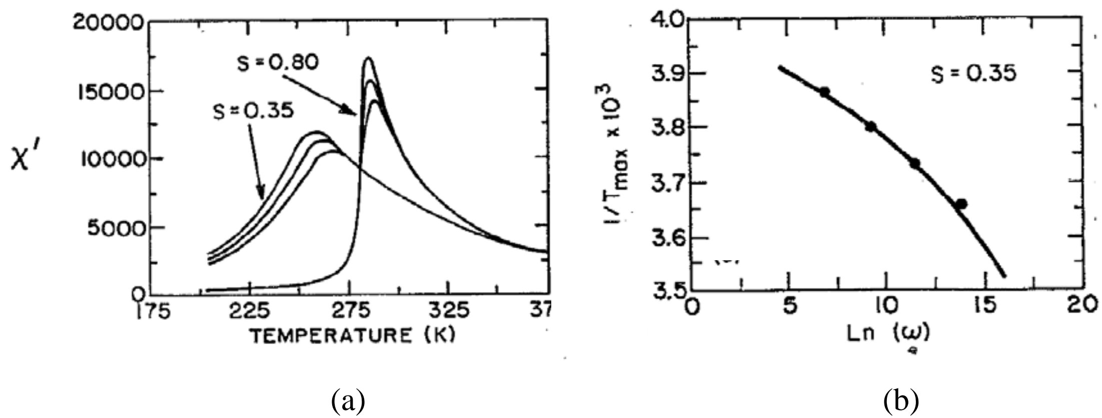

(a) (b)

Fig. 2.7. (a) Permittivity vs. temperature and (b) Vogel-Fulcher analysis for $Pb(Sc_{1/2},Ta_{1/2})O_3$ [29].

A quantitative analysis of the frequency dependence of the maximum permittivities and associated loss values with respect to temperature can be described by the Vogel-Fulcher equation:

$$\omega = \omega_o \exp\left(\frac{-E_a}{k_B (T_{Max} - T_f)}\right) \quad (2.6),$$

where ω is the frequency, ω_o is the attempt frequency, E_a is the activation energy, k_B is Boltzmann's constant, and T_{Max} and T_f the maximum temperature and the freezing temperature, respectively [20]. From here it is possible to determine a temperature, T_f, at which the polarization freezes out. This produces the temperature dependence shown in Fig. 2.6 [20]. Below T_f, the polarization hysteresis behaves like a normal ferroelectric. With increasing temperature, the hysteresis loop becomes slimmer until it appears to be a nearly non-hysteretic, non-linear dielectric at T_{Max}. While the polarization hysteresis shows little net polarization at T_{Max}, (though conduction losses may mimic one), a finite local polarization is observed up to Burn's temperature as mentioned previously [22, 30].

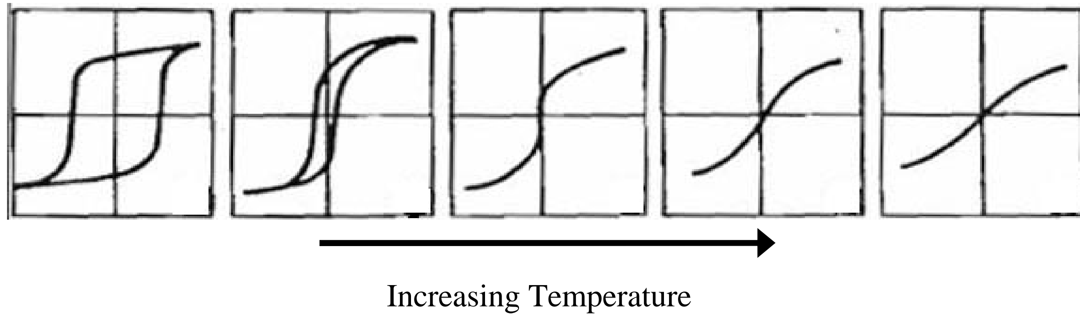

Fig. 2.8. Polarization hysteresis loops for $Pb(Mg_{1/3}Nb_{2/3})O_3$ with increasing temperature [30].

2.1.2 Permittivity of Ferroelectric Thin Films Compared to Bulk Materials

Differences found between the properties of thin films and bulk ceramics or single crystals of the same compositions are ascribed to residual stresses, high point and line defect concentrations, mechanical clamping to the substrate, as well as size effects in thin films. The large difference between permittivity values of bulk and thin films can be seen for $(Ba_{0.7}Sr_{0.3})TiO_3$ in Fig 2.9 [12]. It is clear in the figure that the permittivity for a 100 nm thick $(Ba_{0.7}Sr_{0.3})TiO_3$ film is lower at all temperatures than data for the bulk ceramic, with the most marked suppression at the peak permittivity [12].

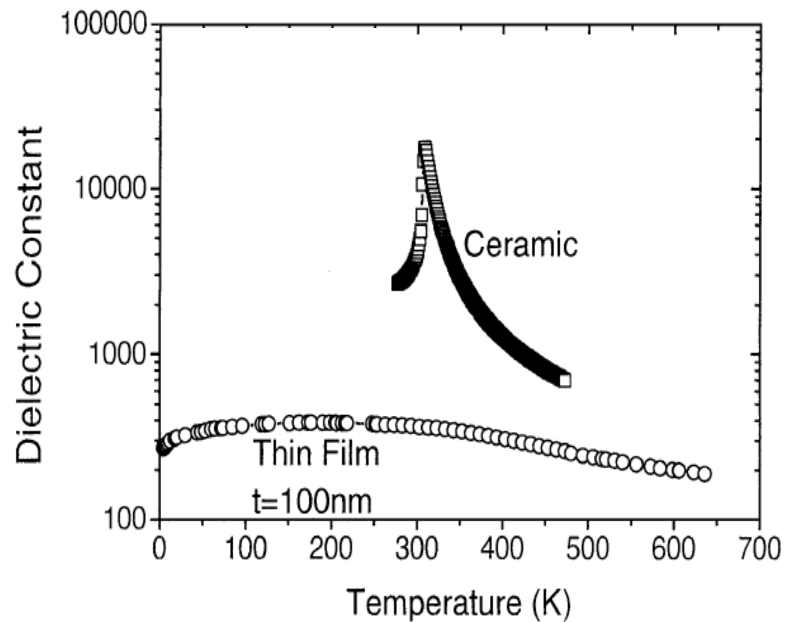

Fig. 2.9. Permittivity vs. temperature for $(Ba_{0.7},Sr_{0.3})TiO_3$ in bulk and thin film form [12].

In bulk ceramics there are several external factors that influence permittivity values. Ferroelectric materials such as $BaTiO_3$ are also ferroelastic, and therefore show substantial pressure dependence [1]. As can be seen from Fig. 2.10, with an applied hydrostatic pressure, the Curie temperature of a bulk perovskite ceramic can be shifted to lower temperatures. Similar studies in thin films show that the ferroelectric Curie temperature can be shifted more than 300°C through controlling the biaxial stress state [31, 32].

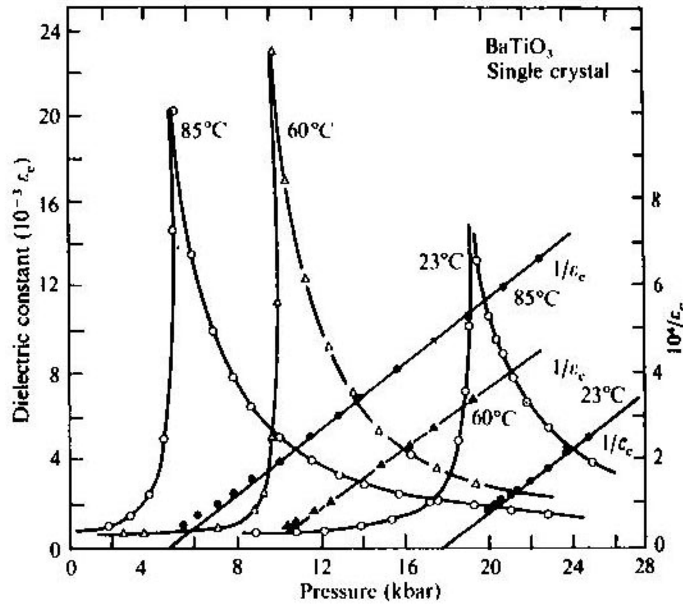

Fig. 2.10. Dielectric constant of $BaTiO_3$ as a function of hydrostatic pressure for different temperatures [1].

There are different types of stresses. Hydrostatic pressure acts as compressive stress in all three principle directions of a material. The compressive stress reduces the volume of the unit cell and favors lower volume polymorphs. In other cases, particularly

in thin film devices, the stresses can have a large anisotropy. Grown films are often under biaxial stress, constrained to the substrate in 2-dimensions while the direction out of the plane of the film is considered to be stress free. Often in thin film devices, these stresses can be advantageous in modulating the band structure of materials (e.g. in Si/SiGe heterostructures) as well as affecting phase stability [31, 33].

Fig. 2.11 shows the stability of the ferroelectric phase as a function of in-plane strain for $SrTiO_3$. From this graph, it is clear that under applied strain, $SrTiO_3$ can be induced into a ferroelectric phase, which was proven experimentally [31].

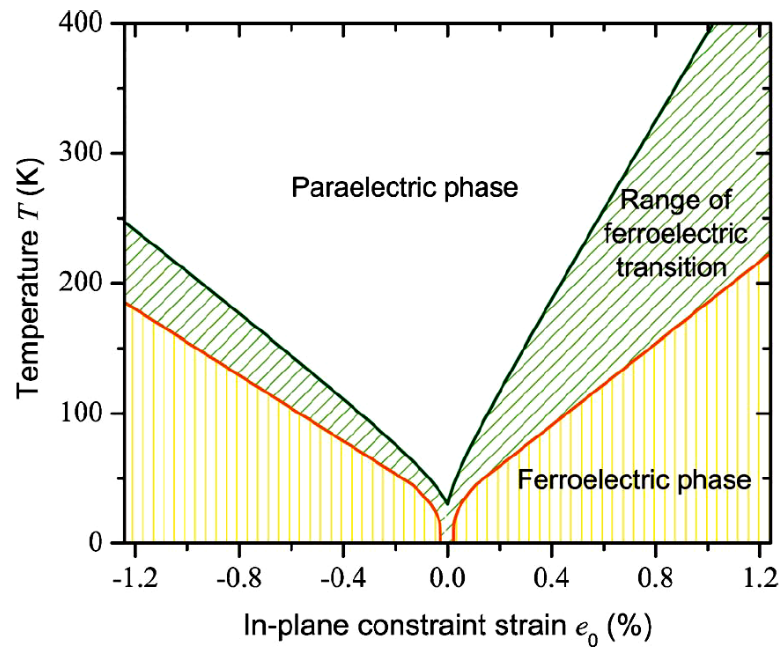

Fig. 2.11. Phase diagram for $SrTiO_3$ showing how in-plane strain can induce a ferroelectric phase in incipient ferroelectric material [34].

Because ferroelectricity is a cooperative phenomenon, it is not surprising that both the properties and the stability of the ferroelectric phase are a function of size. In bulk ceramics, the permittivity changes as a function of grain size, as shown in Fig. 2.12 [12]. In $BaTiO_3$ it was observed that at large grain sizes, the permittivity remains relatively constant. Increasing stresses within the ceramic as grain size falls increase the room temperature permittivity, leading to a peak at a grain size of ~0.8 μm. The permittivity is then shown to decrease with decreasing grain size.

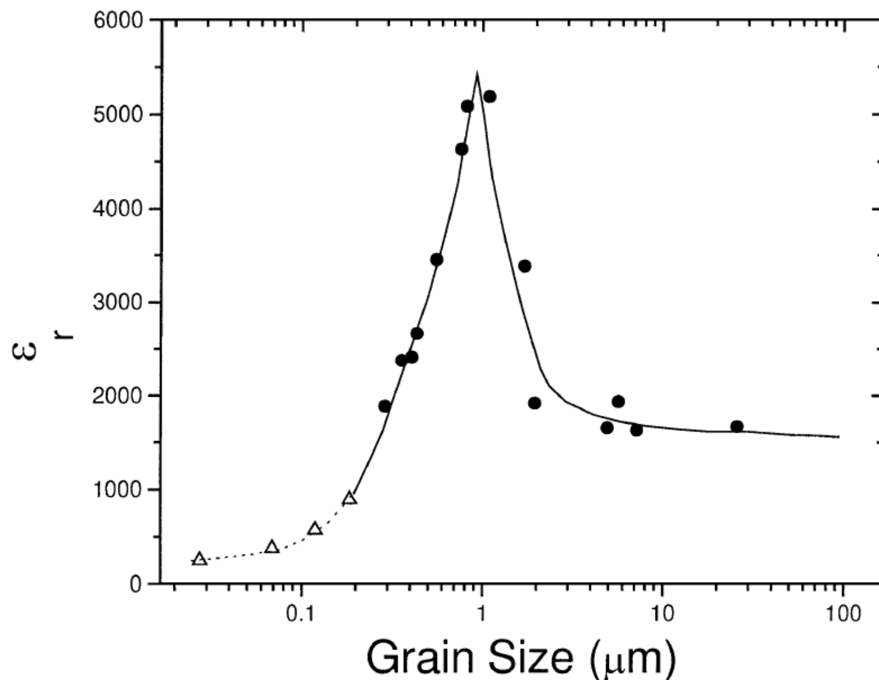

Fig. 2.12. Permittivity vs. grain size for bulk $BaTiO_3$. Circles represent bulk grain size and triangles represent thin film data. After Shaw et al. [12].

One reason that size effects become pronounced in thin films is because grain sizes in films are often smaller than achievable in bulk. As films become thinner, a drop in permittivity and broadening in the permittivity peak is observed. As seen in Fig. 2.13, Parker et al. showed that for $Ba_{0.7}Sr_{0.3}TiO_3$, the permittivity dropped significantly with decreasing thickness [35]. This indicates that for smaller thickness films, one would expect a smaller permittivity value.

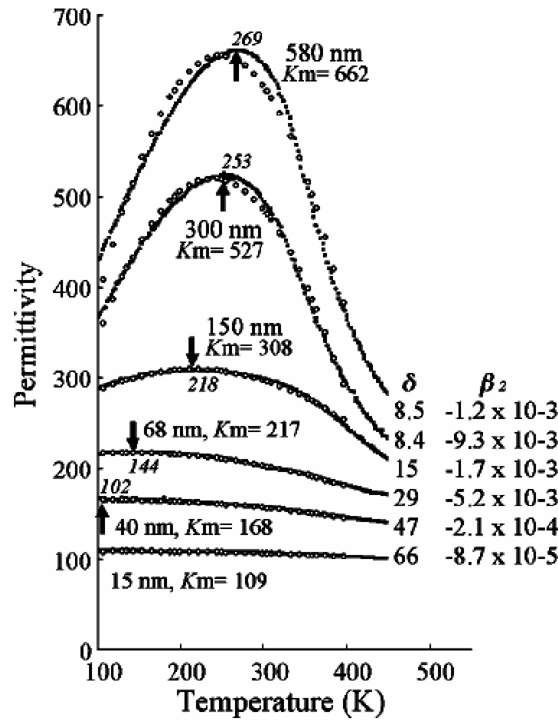

Fig. 2.13. Permittivity vs. temperature of $Ba_{0.7}Sr_{0.3}TiO_3$ thin films on Pt-coated Si plotted for different thicknesses [35].

Additional mechanisms that can cause the permittivity to drop with decreasing thickness are intrinsic size effects and interfacial layers. The material could experience an intrinsic change in permittivity due to the cooperative nature of ferroelectricity. That

is, at small enough thicknesses, the ferroelectric phase can be destabilized in favor of the paraelectric prototype. This is a likely to be important for thicknesses << 100 nm [35-37]. In addition, parasitic interfacial layers could also cause a large drop in permittivity [12, 38]. By plotting the inverse of the capacitance density, it is possible to determine if the film behaves as though it has an interfacial layer. The capacitance density value for the interface layer can be extrapolated by using equation 2.7 [12]:

$$\frac{A}{C} = \frac{2t_i}{\varepsilon_i \varepsilon_0} + \frac{(t - t_i)}{\varepsilon_b \varepsilon_0} \quad (2.7),$$

where A and C are the area of the electrode and capacitance respectively, t and t_i are thickness of the film and thickness of the interfacial layer, and ε_i and ε_b are the permittivity of the interface and of the bulk film respectively. A schematic of the model as well as an example for $(Ba_{0.7}Sr_{0.3})TiO_3$ is given in Fig. 2.14 [12]. It should be noted that while this approach fits a wide variety of experimental data well, in many cases, no discrete interfacial or grain boundary layer can be identified.

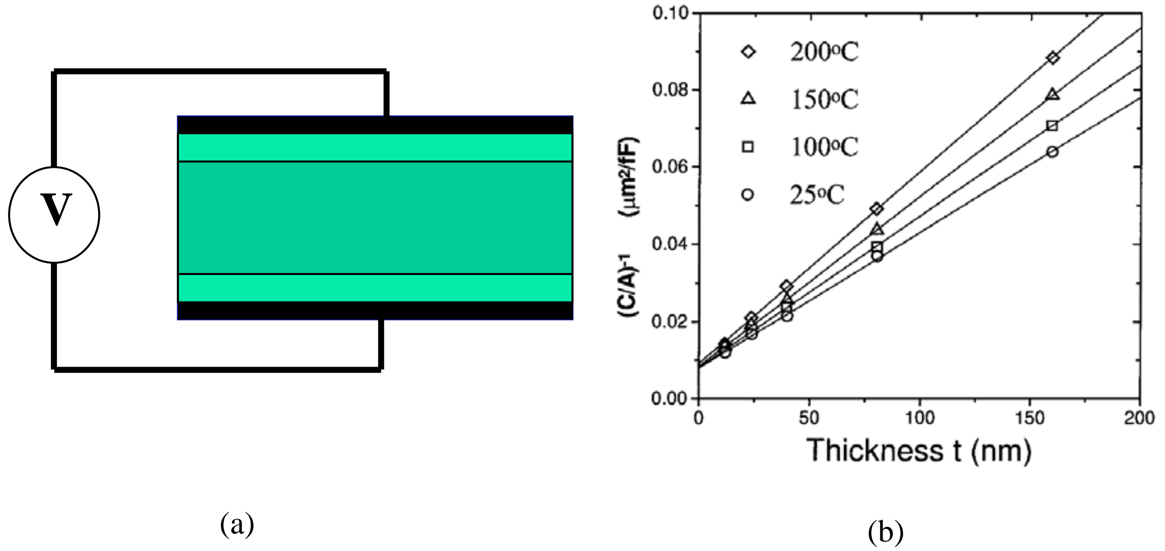

Fig. 2.14. (a) Schematic of the interface model and (b) inverse capacitance density vs. thickness plotted for different temperatures for $Ba_{0.7}Sr_{0.3}TiO_3$ films [12].

Often the suppression of permittivity peaks can be advantageous. Applications such as microwave antennas where constant permittivity over a wide temperature range is important prompted the development of low temperature coefficient of capacitance materials. The temperature coefficient of capacitance (TCC) is defined in equation 2.8:

$$TCC = \frac{1}{C}\frac{dC}{dT} = \frac{1}{\varepsilon}\frac{d\varepsilon}{dT} + \alpha_L \quad (2.8),$$

where ε is permittivity, T is temperature, C is capacitance, and α_L is the coefficient of linear expansion for an isotropic material [14]. Bismuth-based pyrochlores have been developed as linear microwave dielectrics with low temperature coefficients of capacitance [39-41]. The large stability range of the pyrochlore structure allows for

materials properties to be tailored, producing a material with near zero temperature coefficient of capacitance, as shown in Fig. 2.15 [42].

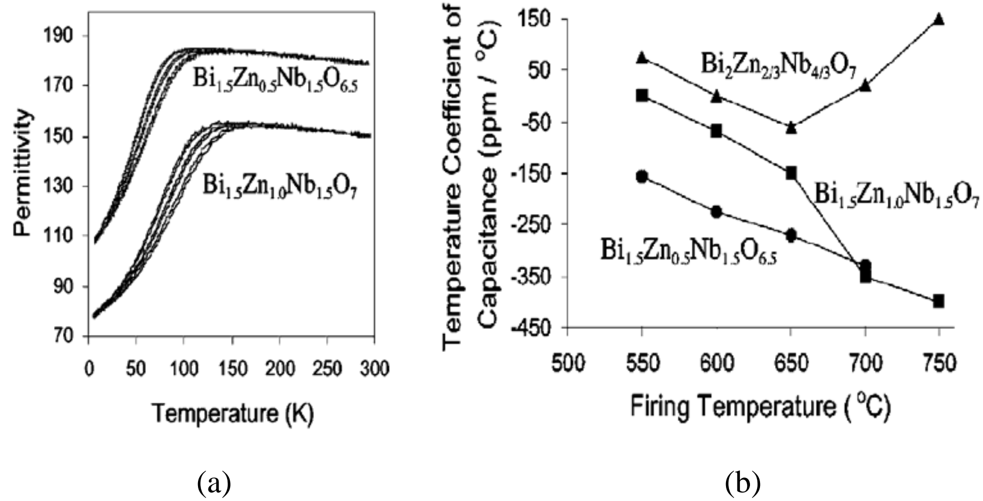

(a) (b)

Fig. 2.15. (a) Permittivity vs. temperature and (b) temperature coefficient of capacitance as a function of firing temperature for bismuth zinc niobate thin films [42].

2.2 Examples of Dielectric Materials

2.2.1 The Perovskite Structure

The $A^{XII}B^{VI}O_3$ perovskite structure, with the possible off-centering of the ions from high symmetry positions lends itself towards materials having large permittivity values. The perovskite structure is composed of a lattice of corner sharing oxygen

octahedra with a large cation in 12-fold coordination as well as a smaller 6-fold coordinated ion in the center of the octahedra as shown in Fig. 2.16a. The prototype symmetry of a perovskite is cubic, however, the tetragonal and rhombohedral distortions (shown in Fig. 2.16b) are important to perovskite-based ferroelectrics.

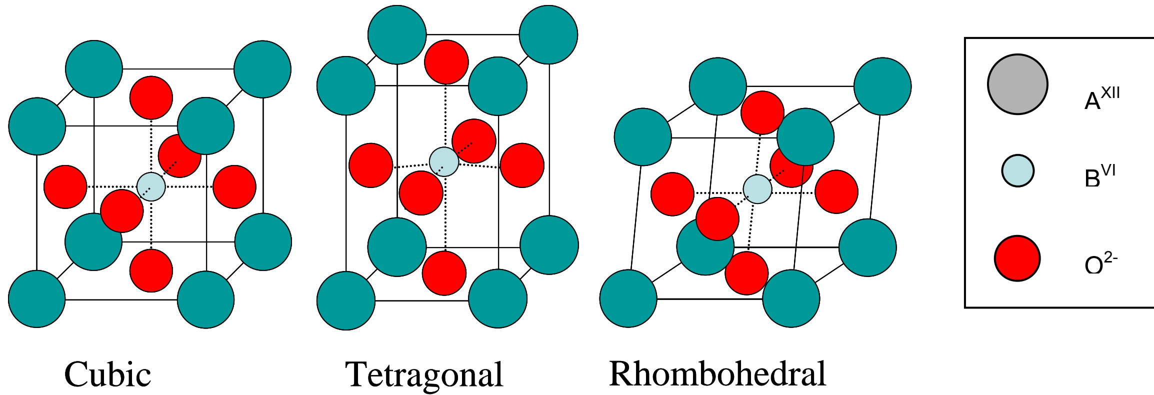

Fig. 2.16. Schematic of cubic perovskite unit cell along with tetragonal and rhombohedral ferroelectric distortions of the perovskite unit cell.

When designing new perovskite materials, the stability of the perovskite structure can often be predicted on the basis of ion size. The Goldschmidt tolerance factor, t, for perovskites has been used extensively to predict the stability of perovskite systems:

$$t = \frac{r_A + r_O}{\sqrt{2}(r_B + r_O)}, \quad (2.9)$$

where r_A is the radius of the ion on the A site, r_B is the radius of the ion on the B site and r_O is the radius of oxygen [9]. It was noted that the perovskite family is stable from t = 0.88 to t =1.09. Within the perovskite family, the symmetry of a given composition was

noted to be correlated to tolerance factor. Materials with tolerance factors above 1 were typically tetragonal, while those with smaller tolerance factors typically have lower symmetries and a tilted oxygen octahedral framework. The correlation between tolerance factor and structure is shown in Table 2.1.

Table 2.1. Tolerance Factor and Crystal Structure for Selected Perovskites

Composition	Tolerance Factor	Structure	Comments	Ref.
$BaTiO_3$	1.06	Tetragonal	FE	[1, 43]
$PbTiO_3$	1.02	Tetragonal	FE	[44, 45]
$SrTiO_3$	1.00	Cubic	PE	[9]
$LaAlO_3$	1.00	Rhombohedral	PE	[9]
$SrRuO_3$	0.99	Orthorhombic	Conducting	[9]
$Pb(Mg_{1/3}Nb_{2/3})O_3$	0.989	Pseudocubic	R-FE	[9]
$PbZrO_3$	0.96	Orthorhombic	AFE	[46]
$BiScO_3$	0.907	Triclinic	PE	[47]

FE—Ferroelectric, R-FE—Relaxor Ferroelectric, AFE—Antiferroelectric, PE-Paraelectric

2.2.2 Morphotropic Phase Boundaries

A morphotropic phase boundary (MPB) is defined as a nearly temperature independent boundary in a solid solution phase diagram between two ferroelectric phases of different composition which differ in symmetry [48]. In most materials, it has been found that morphotropic phase boundaries exist when the tolerance factor is ~1 [9]. At

the morphotropic phase boundary for a rhombohedral-tetragonal transition, both the rhombohedral and tetragonal perovskite distortions are possible (the polarization directions are shown schematically in Fig. 2.17). This leads to an increased number of polarization directions in the material. The larger polarizability of the material allows for enhanced properties over its endmembers [1, 47].

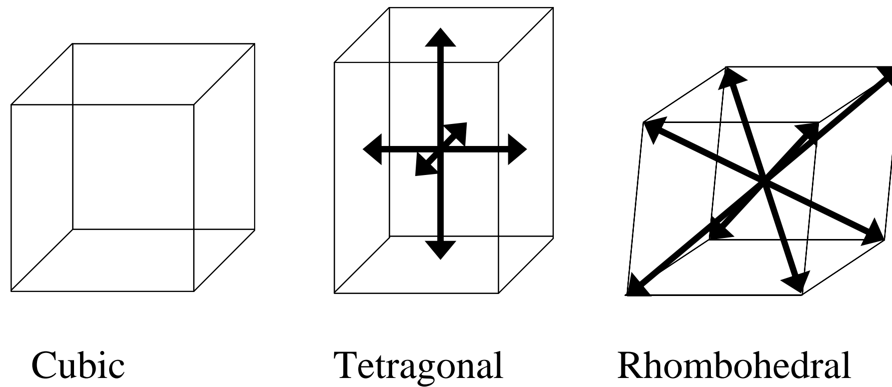

Fig. 2.17 Schematic of polarization directions for cubic (none), tetragonal (<001> directions), and rhombohedral perovskite systems (<111> directions).

2.2.2.1.1 Lead Based Perovskites with Morphotropic Phase Boundaries

Lead-based perovskite ferroelectrics have shown tremendous versatility in dielectric and piezoelectric applications. The large size, high polarizability, and lone pair electrons of the Pb^{2+} cation leads to uses as high permittivity dielectrics, ferroelectrics, and piezoelectrics. Although, many lead-based perovskite endmembers are readily prepared, the most interesting properties occur in solid solutions in which there is a

morphotropic phase boundary [44]. The most extensively studied morphotropic phase boundary has been the $Pb(Zr,Ti)O_3$ system [1, 44]. As can be seen in the phase diagram (Fig. 2.18a), the morphotropic phase boundary is between a ferroelectric rhombohedral phase and a ferroelectric tetragonal phase [44]. As can be seen in Fig. 2.18b, the permittivity at the morphotropic phase boundary increases significantly over that of the endmembers [44].

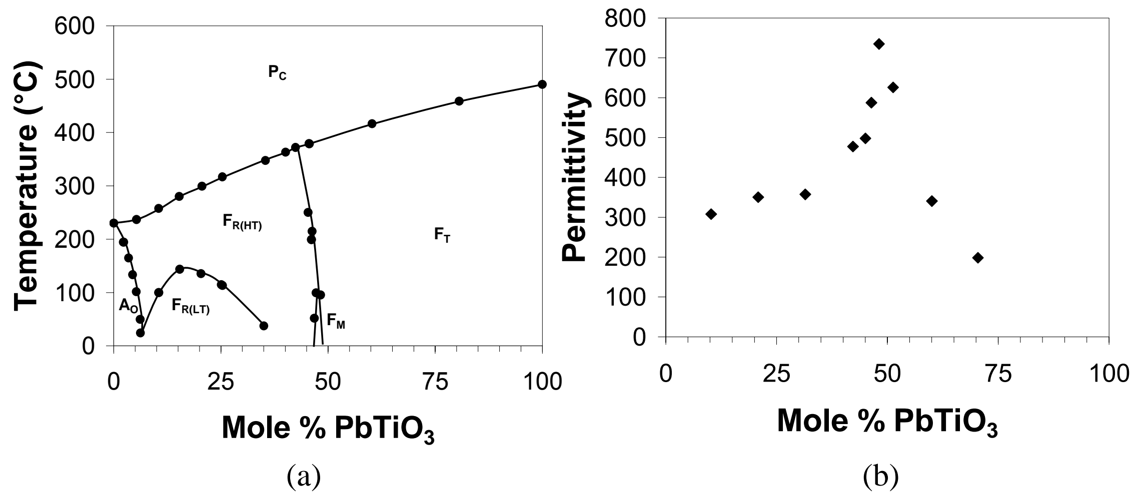

Fig. 2.18 (a) Phase diagram for PZT and (b) room temperature permittivity as a function of composition. P_C is the prototype cubic perovskite phase, F_T, F_R, F_M are the ferroelectric tetragonal, rhombohedral (high temperature HT and low temperature LT) and monoclinic, phases respectively and A_O is the antiferroelectric orthorhombic phase. After Jaffe, Cook, and Jaffe [44] and Noheda [49].

2.2.2.1.2 Lead Reduced Perovskites

Recent legislation in Japan and Europe is aimed at the reduction of the use of lead due to toxicity [50]. This has prompted the development of lead-reduced or lead-free materials. The similar nature of the Bi^{3+} cation to the Pb^{2+} cation, i.e. its polarizability due to the s-shell electrons, has led to the recent emphasis on bismuth containing dielectrics. Emerging from research in this area has been alternative morphotropic phase boundary materials such as $BiScO_3$-$PbTiO_3$.

The development of $BiScO_3$-$PbTiO_3$ and its high room temperature permittivity suggests that Bi-based systems may provide high polarizabilities. Eitel and co-workers took advantage of the morphotropic phase boundary to enhance the permittivity of ceramics to several thousand at room temperature [9]. A solid solution of two high T_C endmembers, $BiScO_3$-$PbTiO_3$ has dielectric properties comparable to PZT with a transition temperature over 100°C higher than PZT at the MPB, as shown in Fig. 2.19a [9]. Thin films also have excellent dielectric properties as evidenced in Fig. 2.19b [51].

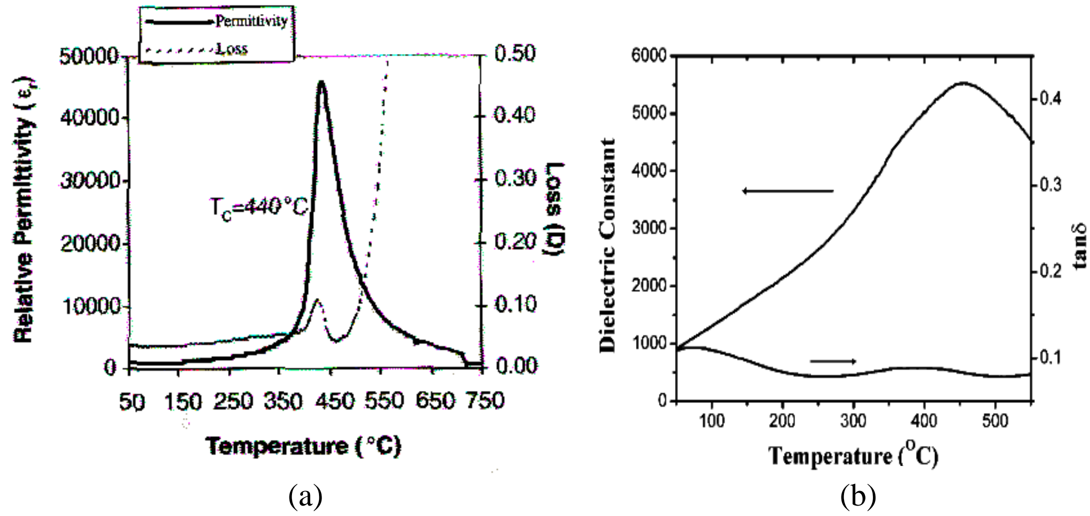

Fig. 2.19. Permittivity vs. temperature for (a) bulk and (b) thin film $BiScO_3$-$PbTiO_3$ at the MPB [9, 51].

2.2.3 Bismuth Doped Perovskites

The Bi^{3+} ion's lone pair electrons and tendency towards covalent bonding (much like the Pb^{2+} ion) in the perovskite structure make it attractive for use in dielectrics [52]. In many cases, when Bi is doped into a host perovskite as an aliovalent dopant, it increases the relaxor character of the perovskite [53-55]. In the case of $BaTiO_3$, it has been shown that relaxor ferroelectricity can be stabilized with bismuth doping.. Bahri et al. showed that for $Ba_{1-x}Bi_{2x/3}TiO_3$, a relaxor ferroelectric state exists between x=0.-09-0.15 while the T_m of the system decreases with increasing Bi concentration (Fig. 2.20) [55]. However, Zhou et al. showed that in $Ba_{1-x}Sr_xTiO_3$, the T_m increased with increasing Bi^{3+} concentration, as compared with undoped ceramics [56]. This leads towards the stabilization of the relaxor ferroelectric phase transition observed in Bi-doped

$SrTiO_3$ at low temperatures [53]. The relaxation of the Bi-doped materials can be fit using the Vogel-Fulcher relation [53-55, 57].

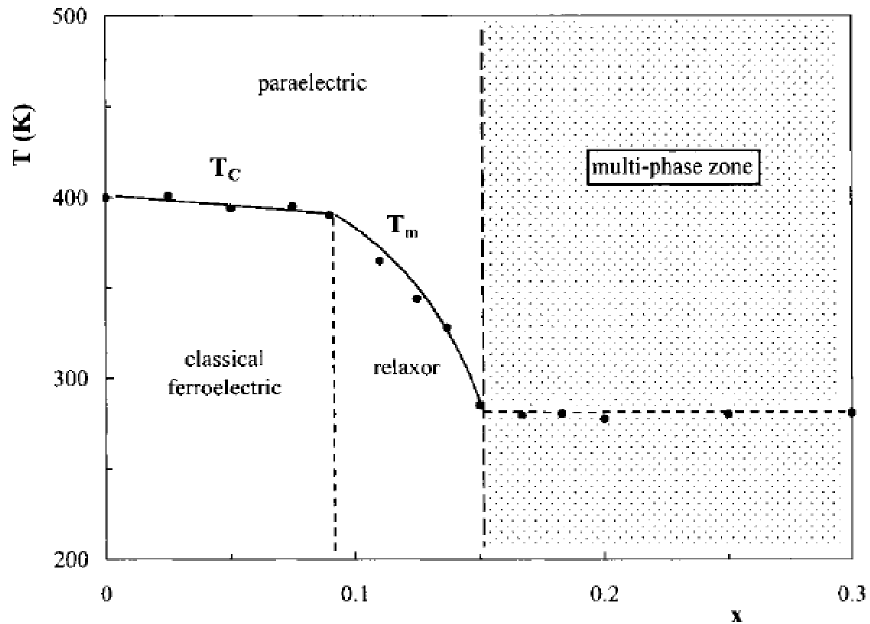

Fig. 2.20. Variation of the transition temperature as a function of composition for $Ba_{1-x}Bi_{2x/3}TiO_3$ ceramics [55].

2.2.4 Bismuth Based Perovskites

Due to the small relative size of Bi^{3+} in 12 coordination, the tolerance factors for bismuth-based perovskites tend to be small [9]. Work done in the Soviet Union in the late 1960s and early 1970s demonstrate that several bismuth perovskites could be synthesized at high pressures [58-61]. However, the dielectric constants reported were small [60]. Recent first principle calculations indicate that several bismuth-based perovskites show large polarizations and piezoelectric properties, including the

endmembers $BiAlO_3$ and $BiGaO_3$ [62]. An MPB has been projected for the $Bi(Al,Ga)O_3$ solid solution, though initial attempts at synthesis have been compromised by poor perovskite phase stability [62-64]. Recently, there have been several reports of high temperature synthesis of Bi-perovskites [64-67]. Selected properties of several known bismuth perovskites are given in Table 2.2.

Table 2.2. Selected Properties of Bismuth-Containing Perovskites Thin Films

Composition	ε_r	P_r ($\mu C/cm^2$)	Notes	Ref.
$BiMnO_3$	1400	-	FE/AFM	[52, 68]
$BiFeO_3$	60	60	FE/FM	[69, 70]
$BiAlO_3$	-	76	Theoretical	[62, 71]
$BiScO_3$	35	-	Non-hysteretic	[67]
$BiGaO_3$	-	152	Theoretical	[62]
$BiCrO_3$	1300	-	Centrosymmetric	[72, 73]

2.3 Physical Vapor Deposition

Physical vapor deposition is a set of vacuum based techniques that use physical processes to deposit thin films. Vacuum techniques such as evaporation, molecular beam epitaxy, sputtering, and pulsed laser deposition are all methods for physical vapor deposition [74]. Through physical vapor deposition, high quality semiconductor, magnetic, capacitor, and optical films, etc. can be made [75, 76].

One aspect of physical vapor deposition that allows for high quality films is ion bombardment. Ion bombardment occurs when ions, or accelerated neutrals, strike the surface of the growing film with enough energy to modify the structure of the film. This is important because it allows for growth of denser films at lower temperatures, decreasing the negative aspects of high temperature growth (thermal stress, interdiffusion, etc).

The energy with which the ions strike the surface of the growing film can be controlled through the gas pressure during deposition. This is because with each collision with an ambient gas particle, the ion will lose a finite amount of energy. The net amount of energy the particles loses is correlated with the average distance between collisions, or in other terms, the mean free path of a particle in the gas phase. The relationship between the mean free path of a molecule, l, in a gas and the pressure is given by equation 2.10;

$$l = \frac{RT}{\sqrt{2}\pi a^2 P N_A}, \quad (2.10)$$

where a is the radius of the species, P is the pressure in the system, N_A is Avogadro's number, R is the gas constant and T is the temperature of the system [74]. From this equation, it is clear that the lower energy deposition processes, such as evaporation, require deposition in high vacuum, while higher energy processes have a tolerance for an ambient background gas.

2.3.1 Evaporation

Evaporation deposition is a technique where the species deposited comes from a molten target via thermal or e-beam evaporation. During evaporation, energy is imparted

to atoms in the melt, which then vaporize. The vapor travels through the vacuum and lands on the surface of the substrate, creating the growing film. The kinetic energy of the atoms hitting the substrate is on par with the thermal energy imparted to them during the vaporization process ($\sim\frac{3}{2}k_BT$) [75]. The development of effusion cells allows control of the vapor source for high precision techniques such as molecular beam epitaxy, where extremely high quality films can be made [31, 76]. E-beam evaporation may provide better stoichiometry control of the growing films due to the elimination of contamination from the crucibles, though source stability is generally inferior [74, 75]. E-beam sources also allow a wider variety of elements to be vaporized

2.3.2 Sputtering

Sputter deposition is a technique which uses the plasma that develops between two electrically charged plates. The process is shown schematically in Fig. 2.20 [74, 75]. The gas used to create the plasma may be inert to avoid reaction with the sputter target and sputtered ions prior to deposition. Alternatively, reactive gasses such as O_2 are also widely used in deposition of oxide films. When the plasma is created, the positive ions are accelerated towards the sputter target. When the accelerated ions strike the target surface, the kinetic energy of the ions is transferred into the breaking of chemical bonds in the target and providing kinetic energy to the liberated atoms. The atoms travel through the plasma and deposit on the substrate. The use of magnetic fields to trap the electrons near the target surface allows for lower deposition pressures to be used. Additionally, for deposition of insulating targets and films, a radio frequency voltage

supply is used to avoid having charges build up on the surface of the target which would slow or even stop deposition. Through sputtering, an impingement energy on the order of 5 eV can be achieved for the depositing species [74, 75, 77].

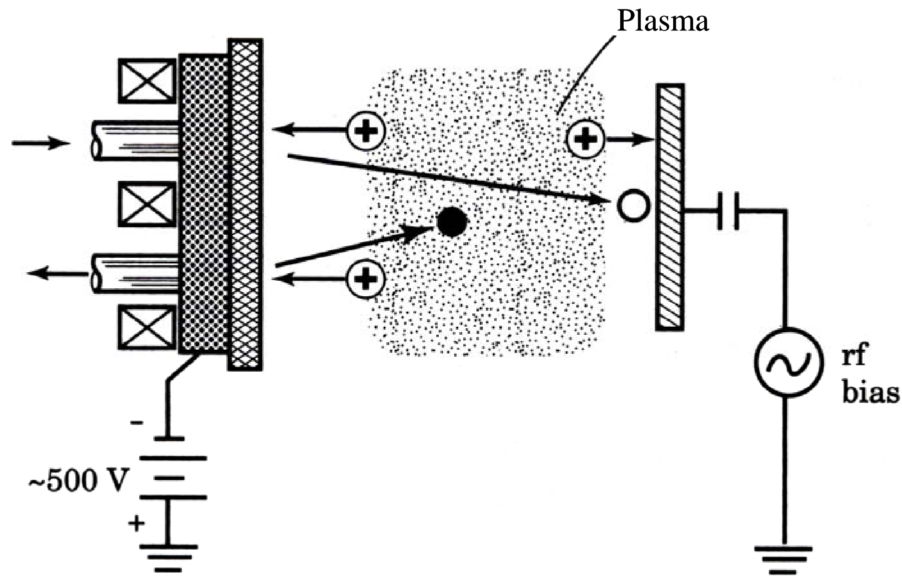

Fig. 2.21. Schematic of sputter deposition. After Smith [74].

2.3.3 Pulsed Laser Deposition

Pulsed laser deposition is a vacuum deposition technique where laser radiation is used to ablate material from a target. A schematic of a typical pulsed laser deposition system is given in Fig. 2.21. Optical lenses focus the laser beam, creating a large instantaneous power density ~10^8 W/cm^2 which allows for congruent ablation of the target [78]. Typically the focused laser beam ablates a rotating target within the vacuum chamber and a plume of material is ejected approximately normal to the target surface.

The vaporized material can deposit on any free surface. A reactive gas at pressures as high as 500 mTorr can be used during laser ablation because the kinetic energy imparted to the ions in the plume is much higher than in other physical vapor deposition techniques [74, 75, 78]. Because this was the primary growth tool employed in this thesis, additional details will be given on this technique.

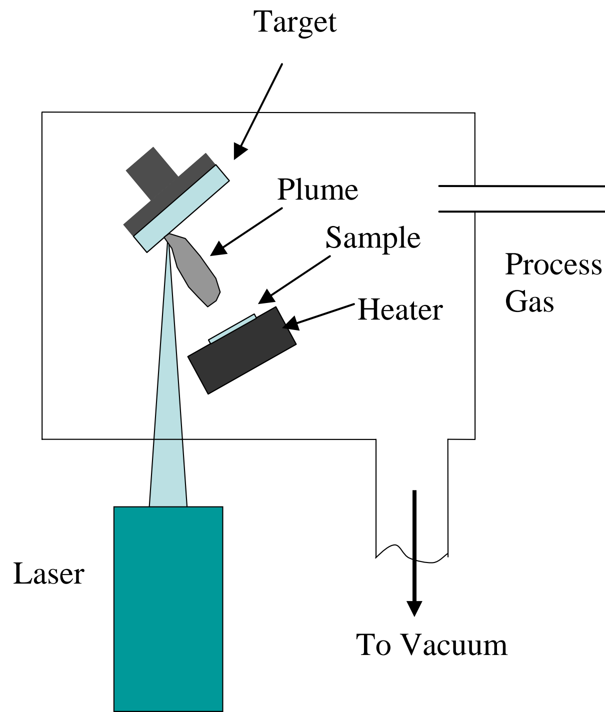

Fig. 2.22. Schematic of a pulsed laser deposition system.

2.3.3.1 Laser-Target Interaction

The ablation process occurs in a few steps. As the laser strikes the target, there is photon absorption at the surface which may generate a molten layer [43, 78]. Atoms, ions, and clusters are ejected from the target in a plume. The rapid heating of the surface

causes a phonon shockwave to be transmitted through the target. The shockwave is reflected back to the surface and may cause either ejection of molten droplets or particulate ejection as shown schematically in Fig. 2.22 [78].

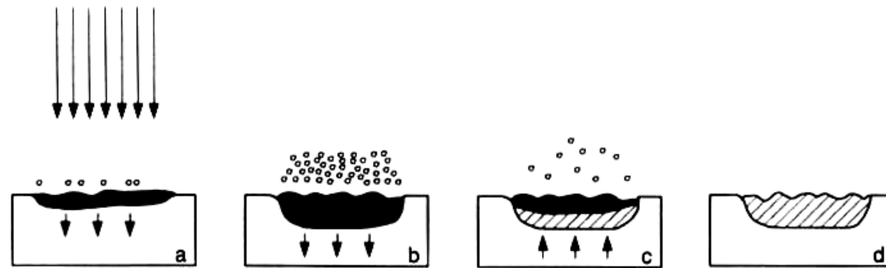

Fig. 2.23. Schematic of thermal cycle during a laser strike on the target [78]. (a) absorption of the laser radiation, (b) propagation of melt front and evaporation of material, (c) recoil of thermal shockwave and (d) solidification of the surface.

2.3.3.2 Plume Characteristics

The rapid expansion of the plume from the explosive vaporization, as well as the absorption of the laser light imparts a very high plasma temperature during the initial plume expansion. The high kinetic energy of the ions in the plume allows for the use of high deposition pressures as compared with other physical vapor deposition techniques [78]. Fig. 2.23 shows the time-evolved expansion of a plume in vacuum in a 100 mTorr O_2 ambient [79]. From this, it is evident that the expansion of the plume is perpendicular to the target. Increasing the background pressure will decrease the velocity of ions in the

plume due to thermalization; comparatively little is known about interparticle collisions within the plume. Under conditions where ablation, rather than evaporation dominates formation of the vapor phase, the stoichiometry of the plume corresponds fairly closely to the target stoichiometry [78]. This is one for the most useful aspects of pulsed laser deposition as a method for depositing multi-component films. It should be noted however, that the deposited films may not have the same stoichiometry as the target for a number of reasons, including preferential ablation, preferential scattering of one component out of the plume, segregation on the surface, and different sticking coefficients on the surface of the deposited film [80].

Additionally, particulates are ejected perpendicularly from the surface. Particles have sufficient energy to deposit on the surface of the growing film and often can affect microstructure and subsequently the properties of the film. To this end, a variety of elaborate techniques to reduce the particulate density have been explored to improve film quality [78, 81].

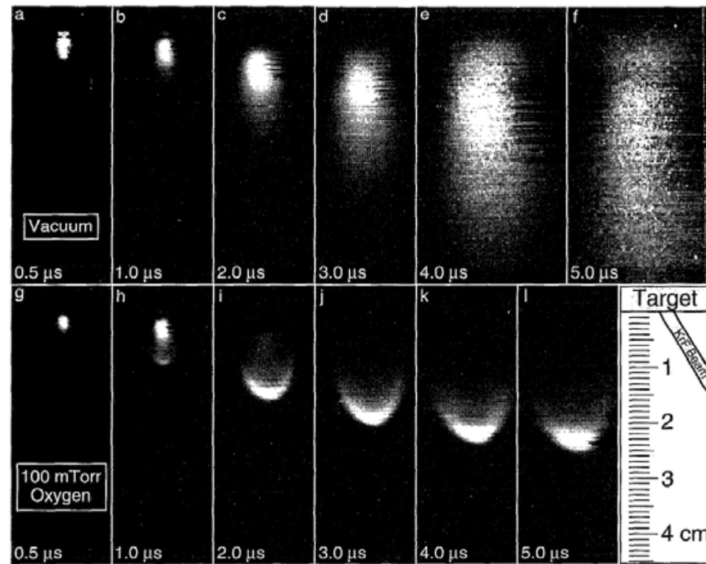

Fig. 2.24. Time lapsed CCD images of laser plume expanding into vacuum (a-f) and 100 mTorr O_2 (g-j) [79].

2.3.3.3 Particulate Generation

Particulate generation can occur in three different ways: subsurface boiling, expulsion of droplets, and recoil from thermal shock [78]. In subsurface boiling, a lower boiling point species will vaporize from the melt and cause droplets from the molten surface to be splashed onto the substrate. For high melting temperature and insulating materials, this process is generally considered to be negligible. During expulsion of droplets, a molten surface layer forms and the shockwave from the thermal recoil expels droplets from the melt. Fig. 2.24 shows schematically the most common form of particulate ejection for dielectric materials, which is solid needle-shape particles, rather than droplets, that break off due to the recoil from thermal shock. The needle-shaped particles form during deposition due to local variations in composition which create a

locally vaporization-resistant surface [82]. During ablation, these ablation-resistant areas shadow the material immediately below to create cones on the surface. Once the cones reach a critical size, the thermal recoil from the laser strike snaps the cone and ejects the particle from the surface. Methods such as off-axis deposition, velocity filters and crossed fluxes have been developed to reduce particulates [43, 81].

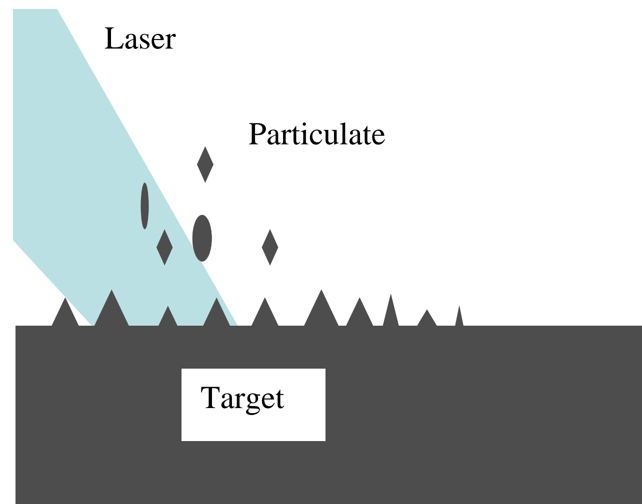

Fig.2.25. Schematic of particulate generation in pulsed laser deposition.

2.4 Thin Film Growth

There are three different modes for growth that occur widely in physical vapor deposited films. On one extreme, Frank-Van der Merwe growth occurs layer by layer. This is often seen during homoepitaxial growth (growth of a material onto itself with lattice registry), or with heteroepitaxial growth of materials (growth of one material on another, again where the crystal lattices of the film and substrate are registered) [74]. As the atoms absorb onto the surface they lose energy [77]. If there is enough energy in the

adatoms, and thermal energy on the surface, a finite number of absorbed atoms will evolve from the surface. The absorbed adatoms that do not have enough energy to vaporize from the surface may have enough energy to diffuse on the surface. The adatoms that are moving around on the surface will seek out a lowered energy state, whether it is as part of an island, absorbing onto a ledge, or filling in a surface vacancy as shown schematically in Fig. 2.25a [77]. Film growth which occurs as adatoms land on the surface and move to the edge of a step, extending the step edge forward, is called step flow growth and is shown schematically in Fig. 2.25b.

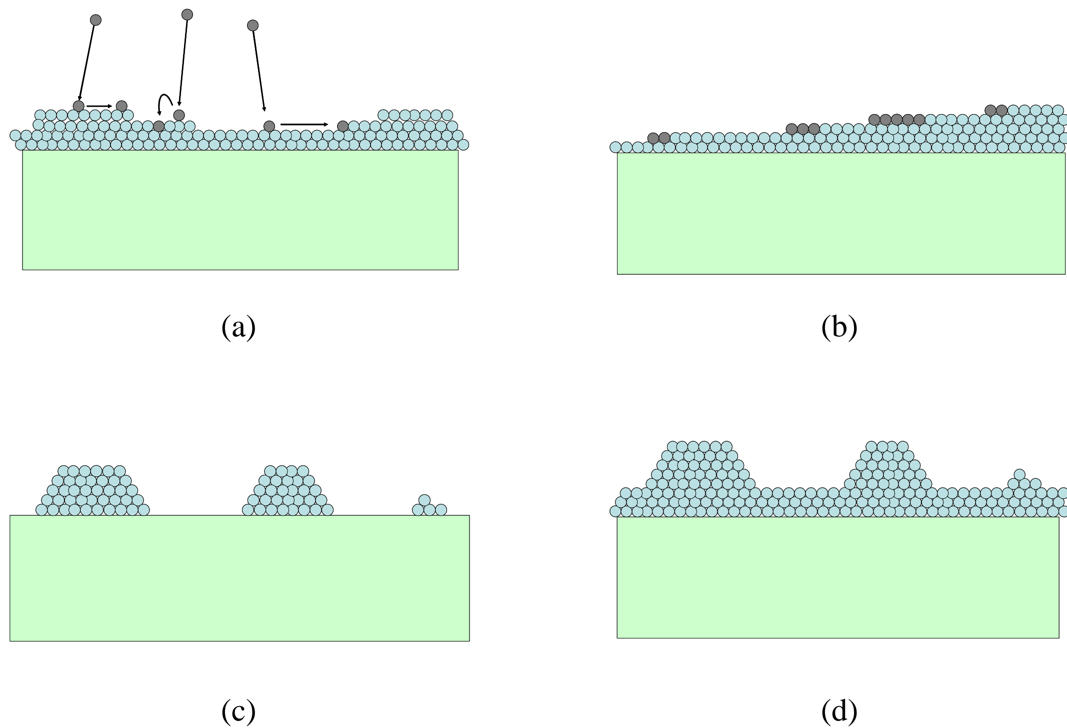

Fig. 2.26. Schematic of (a) Frank-Van der Merwe growth, (b) ideal step flow growth, (c) Volmer-Weber growth and (d) Stranski-Krastanov growth. The dark circles in (a) and (b) represent vapor deposited atoms. After Smith [74]

During deposition, if the substrate and the film are sufficiently different so that the film atoms would rather bond to themselves than the substrate, islands form (see Fig. 2.25c). The nucleation of islands on a surface follows the same form of thermodynamics as nucleation within a melt or glass-ceramic, i.e., once a critical radius is passed, a stable island is formed [75, 77]. As atoms are deposited and land in a region with no islands, provided that they have enough energy, they will move around and either form an island nucleus or will diffuse around the surface until they adhere onto the edge of an island.

An intermediate growth mode that includes a layer-by-layer deposition and island growth, called Stranski-Krastanov growth, occurs when several monolayers of material grow before island formation [77]. This is shown schematically in Fig. 2.25d. Island formation occurs as a result of a combination of strain and surface energy associated with lattice mismatch between the substrate and the film [74, 75, 83, 84].

2.4.1 Epitaxial Growth

Epitaxial growth can occur via Stranski-Krostanov or a layer by layer route for film/substrate combinations which have small lattice mismatches (<5%) [74, 75]. For high quality epitaxial films, the difference between the lattice parameters of the substrate and film must be small at growth temperatures, and the surface energies of the film and the substrate should be comparable. The lattice mismatch, *f*, between the substrate can be calculated using equation 2.11,

$$f = \frac{(a_f - a_s)}{(a_f + a_s)/2} \approx (a_f - a_s)/a_s \text{ , (2.11)}$$

where a_f and a_s are the film and substrate lattice parameters, respectively [74, 75]. At small thicknesses, epitaxial films are coherently strained to the substrate due to the energy required to create misfit dislocations. From strain energy calculations, a relationship between the critical thickness for a coherent film, d_c, and the lattice mismatch is expressed in equation 2.12:

$$d_c = \frac{b(1-\nu\cos^2\theta)}{4\pi f(1+\nu)\cos\lambda}\ln\left(\frac{d_c}{b}+1\right), \quad (2.12)$$

where b is the Burger's vector, θ is the angle between the dislocation line and the Burger's vector, ν is the Poisson's ratio, and λ is the angle between two Burger's vectors [74]. Above this critical thickness, misfit dislocations form to relieve the stress of the films. A schematic of 2 types of misfit dislocations, one generating from the substrate and another generating from the surface, is given in Fig. 2.26.

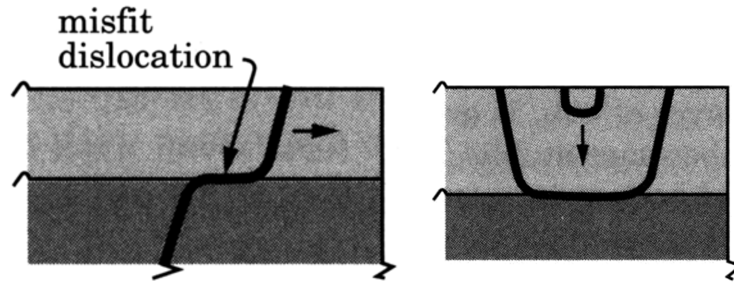

Fig. 2.27. Schematic of misfit dislocations in epitaxial films [74].

2.4.2 Polycrystalline Growth

When either the kinetics of film deposition does not favor epitaxial growth or there is no appropriate lattice mismatch, polycrystalline films result. During physical vapor deposition, the amount of energy provided to the adatoms plays a significant role in controlling the structure of the film. Analyzing the microstructure of grown films, four zones can be identified. In zone 1 films (Z1), the substrate temperature is low and the depositing atoms undergo a "hit and stick" mechanism where there is insufficient thermal energy for motion of the adatoms [77]. The morphology of these films is highly porous and is governed by a self-shadowing process, leading towards the conical shaped grains shown in Fig. 2.27. In the zone T regime (ZT), there is just enough thermal energy for some surface diffusion, which allows a denser film to be made; however, there is insufficient energy for large scale surface ordering to occur [75, 77]. This allows the grains to become more columnar in shape, diminishing the surface roughness.

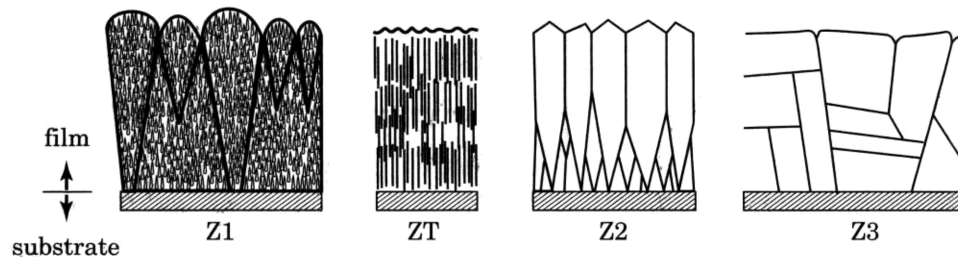

Fig. 2.28. Schematic of the four zones of thin film growth [74].

In zone 2 films (Z2), there is sufficient thermal energy for surface diffusion of the atoms as well as short range bulk diffusion. During growth of zone 2 films, the films

show re-crystallization and grain growth characteristics [75]. The surface of the film develops facets due to the surface energies associated with specific crystallographic orientations. As the temperature of the substrate increases to about two-thirds of the melting temperature of the film (zone 3, Z3), bulk diffusion dominates film growth and larger equiaxed grains appear in the film. The surface of the film smoothens as well. A schematic of a composite structure zone-diagram is given in Fig. 2.28.

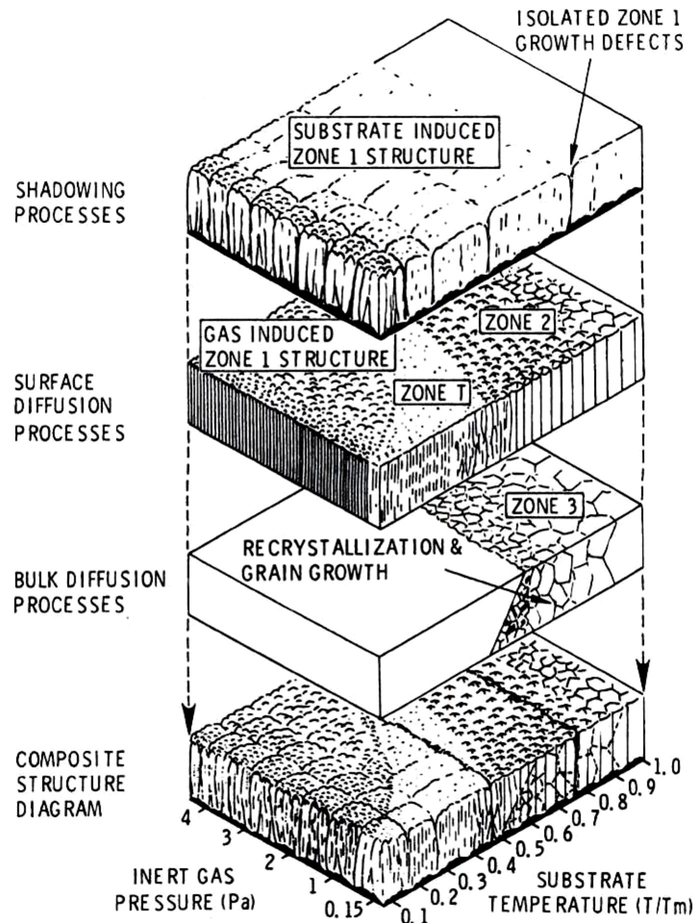

Fig. 2.29. Composite structure zone model for polycrystalline films [75].

In addition to temperature, the energy of bombarding species can also change the adatom energy. In Fig. 2.28, one axis of the structure zone model is gas pressure. The gas pressure controls the bombardment energy of the films through collisions with the depositing atoms or ions. In a growing film, if the energy of the bombarding species is greater than the bond energy between atoms in the film, the bombarding atom modifies the film structure. There are three main types of modifications to the film that a bombarding atom can perform; forward sputtering, re-sputtering, and implantation. Under forward sputter conditions, an incoming atom hits the surface and knocks an atom forward, densifying the film. In re-sputtering, the incoming atom sputters an atom off the surface of the film. In implantation, an incoming atom has sufficient energy to burrow into the film and fills either a vacancy or an interstitial location. When an atom fills an interstitial location, the ion-induced bombardment expands the lattice of the film [46, 85]. A schematic illustrating these bombardment conditions is given in Fig. 2.29. As the background gas pressure increases, additional thermalization occurs, and the amount of bombardment decreases. This is what leads to the pressure dependence seen in the structure zone model.

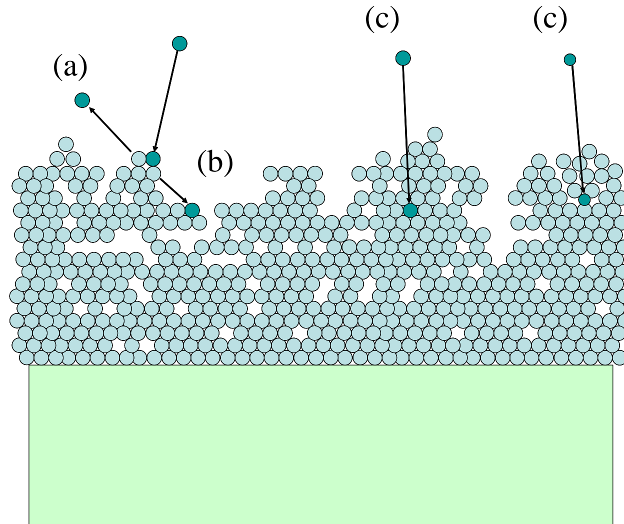

Fig. 2.30. Schematic of ion bombardment on growing films showing (a) resputtering, (b) forward sputtering, and (c) implantation. After Smith [74].

2.4.3 Stress Development in Thin Films

Stresses that develop during thin film growth can have a significant impact on the properties of the film [33, 86-88]. During the initial stages of epitaxial deposition, the lattice of the epitaxial layer will constrain itself to the lattice of the substrate as shown schematically in Fig. 2.30a and Fig. 2.30b. Being constrained to the substrate, the film is under stress in the plane of the film, i.e. the *x* and *y* directions. For a high symmetry material through Poisson's ratio, this creates a strain out of the plane of the film which can be calculated using equation 2.13;

$$\varepsilon_z = \frac{-2\nu\varepsilon_{x,y}}{1-\nu}, \quad (2.13)$$

where ε_z is the out of plane strain, ν is Poisson's ratio and $\varepsilon_{x,y}$ is the biaxial strain present in the film [74]. As mentioned before, epitaxial films remain strained to the substrate until a critical thickness is reached. Upon passing that thickness, films begin to form misfit dislocations as shown schematically in Fig. 2.30c.

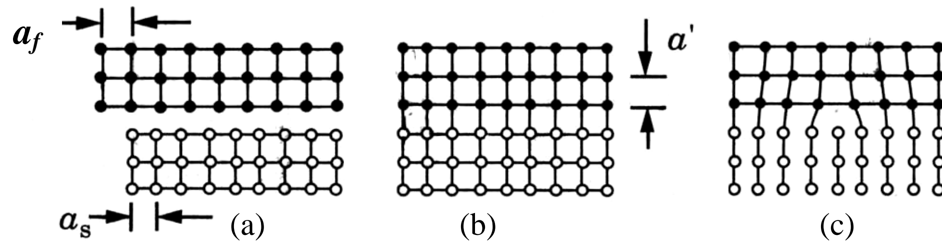

Fig. 2.31. Schematic of lattice mismatch between film and substrate (a) film and substrate lattices prior to deposition, (b) film lattice constrained to substrate, and (c) misfit dislocation relieving stress in the film. After Smith [74].

Upon complete relaxation, in both epitaxial and polycrystalline thin films, residual stresses stem largely from thermal mismatch between the film and the substrate. The thermal stresses that develop during thin film deposition can be quite large, often ranging from hundreds of MPa to the GPa regime [12, 89]. Thermal stresses originate from differences in the thermal expansion between the film and the substrate [90, 91]. The stress, $\sigma_{thermal}$, and strain, $\varepsilon_{thermal}$, associated with the thermal mismatch between the substrate and film is shown in equations 2.14 and 2.15;

$$\sigma_{thermal} = \int_{T_1}^{T_2} \frac{(\alpha_{film} - \alpha_{substrate})}{1 - \nu_{film}} dT \quad , (2.14)$$

$$\varepsilon_{thermal} = \int_{T_1}^{T_2} (\alpha_{film} - \alpha_{substrate}) dT \quad , (2.15)$$

where T is temperature, α_{film} is the coefficient of linear expansion of the film and $\alpha_{substrate}$ is the coefficient of linear expansion of the substrate [89]. The elastic energy, E_e, associated with these stresses is given in equation 2.16;

$$E_e = Yd\varepsilon^2 / (1 - \nu), (2.16)$$

where Y is the Young's modulus, d is the thickness of the film and ε is the total strain in the film.

Additionally, ion bombardment and the resulting modification of the growing films can have significant influences on the stresses that develop. Through ion bombardment, atoms are knocked out of their equilibrium position into interstitial sites, or implantation of bombarding ions occurs, increasing the volume of the unit cell. It has been shown previously that the stresses associated with this can have an adverse affect on film properties [46, 92]. Through controlling the kinetic energy of the bombarding species, it is possible to have near zero bombardment-induced stresses [93].

2.4.4 Thin Film Characterization

There are several methods to characterize the structure and microstructure of the films, including atomic force microscopy, electron microscopy, and diffraction

techniques [75]. Through atomic force microscopy, one can obtain an image of the surface of the films as well as a characterization of the roughness. Thus, the grain size of the film can be obtained. In electron microscopy, two different techniques can be used for film characterization; scanning electron microscopy, and transmission electron microscopy. Scanning electron microscopy is a lower resolution technique that can be useful for determining grain size, growth mode, and thickness of the films. Transmission electron microscopy offers those same features, however at much higher resolution. Through transmission electron microscopy, one can explore the interface between the film and substrate, and through electron diffraction determine the space group of the films. Due to sample preparation requirements, transmission electron microscopy is a destructive testing method.

X-ray diffraction, is a non-destructive technique that can be used to determine a number of parameters, especially for phase and texture analysis [94]. In thin films, x-ray diffraction can be used for stress analysis, thickness and grain size calculations, and characterization of periodic nanostructures [94, 95]. X-ray diffraction uses an x-ray source, typically a Cu filament, to produce radiation with a wavelength in the Angstrom range. When the radiation hits a periodic structure, it reflects according to Bragg's law [94]. A schematic of a common x-ray diffraction apparatus is shown in Fig. 2.31. From performing scans in the θ-2θ mode, one can obtain peaks from multiple planes in the material, enabling structure calculation of polycrystalline samples [94].

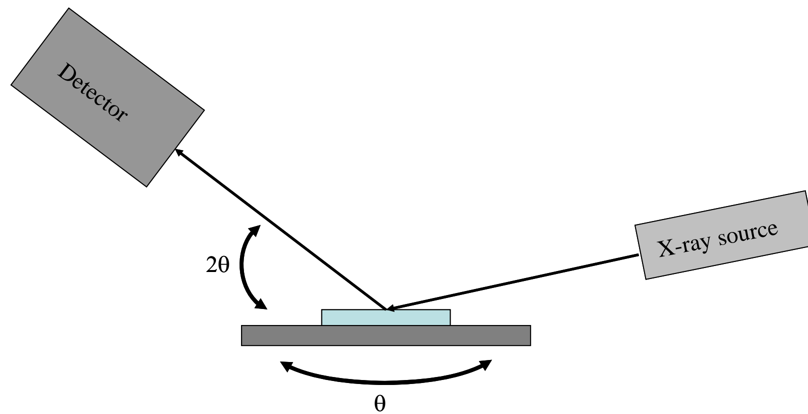

Fig. 2.32. Schematic of a common x-ray diffraction setup.

Using instruments such as the 4-circle diffractometer, it is possible to obtain measurements of lattice planes with normals that are not parallel to the sample surface. Using 4-circle diffractometers it is then possible to measure both the in-plane and out-of-plane lattice parameters of textured samples [43, 45, 95]. In epitaxial films, as the individual grains grow past the critical thickness, they develop a slight misalignment to the substrate called mosaic tilt [95]. A schematic is shown in Fig. 2.32. If the normal to the surface for each segment of the mosaic tilt is plotted, it is seen that there is a finite spread from the ideal. By performing scans along the ω axis, one can obtain a measure of the degree of mosaic structure to the film. Additionally, in ferroelectric materials, it is possible to detect ferroelastic twinning through these type of scans [43, 45].

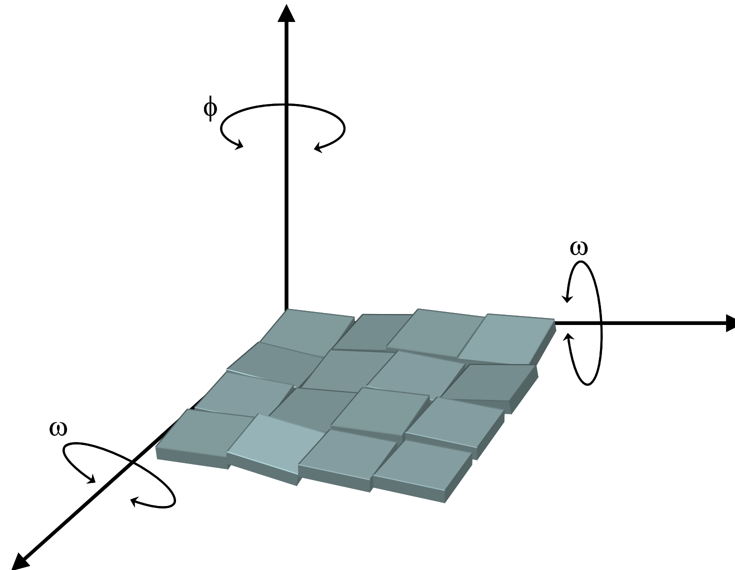

Fig. 2.33. Schematic of mosaic tilt in a thin film.

3.0 Experimental Procedure

This chapter discusses the procedures used to grow and characterize $BiScO_3$-$BaTiO_3$ thin films. An overview of the compositions used, and target preparation is discussed. Tolerance factor calculations were used to narrow the range of compositions to be explored. Targets for pulsed laser deposition were prepared using bulk processing techniques and liquid phase sintering. The pulsed laser deposition system used in this thesis is described, along with the deposition parameters utilized. The resulting films were characterized structurally by 2-circle and 4-circle x-ray diffraction, while film morphology was probed by scanning electron microscopy. Lastly, the procedure for electrical measurements, including top electrode definition and the system used for electrical measurements is described.

3.1 Compositions of Interest

This thesis was directed towards identifying a morphotropic phase boundary in the $BiScO_3$-$BaTiO_3$ system. The Goldschmidt tolerance factor (equation 2.9) was used as a guideline for identifying interesting compositions. Table 3.1 shows the ionic radii used for calculation of the perovskite tolerance factor.

Table 3.1. Ionic radii used for tolerance factor calculations.

Ion	**Radius (Å)**
Ba_{XII}^{2+}	1.60 [96]
Bi_{XII}^{3+}	1.34 [9]
Sc_{VI}^{3+}	0.745 [96]
Ti_{VI}^{4+}	0.60 [96]

Fig. 3.1 is a graph of the tolerance factor calculation for a solid solution of xBiScO$_3$-(1-x)BaTiO$_3$. As put forth by Eitel et al., a tolerance factor of ~1 in a solid solution is characteristic of many morphotropic phase boundaries [9]. The composition at which the tolerance factor equals one is $x = 0.37$. Thus the targets were chosen to have compositions in the range of x=0.2 to x = 0.6 in order to straddle the predicted morphotropic phase boundary.

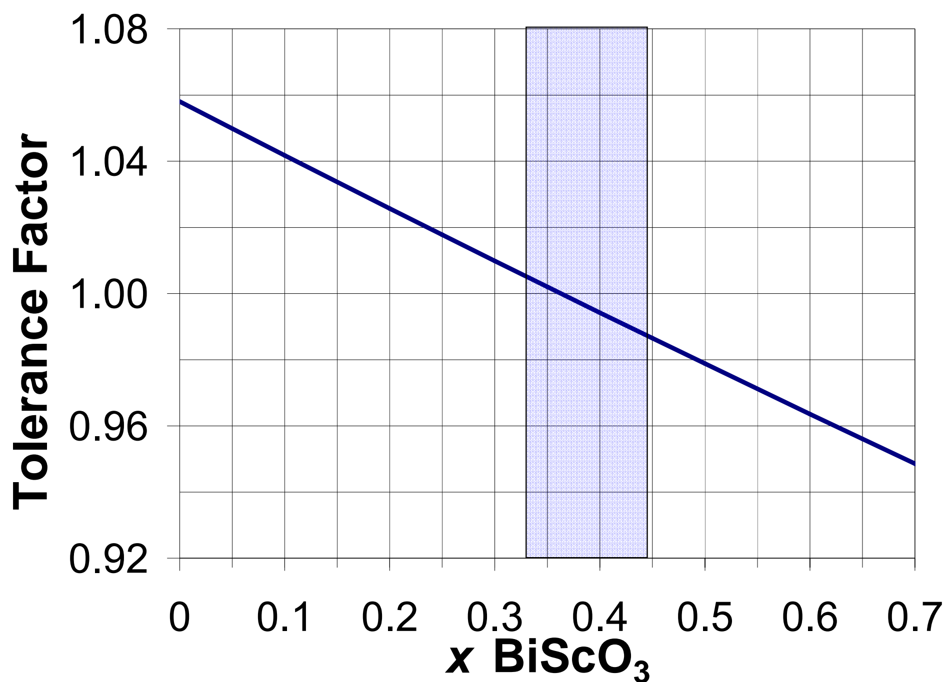

Fig. 3.1. Calculated tolerance factor for the xBiScO$_3$-(1-x) BaTiO$_3$ system.

3.2 Target Preparation

Ceramic targets for pulsed laser deposition (PLD) were batched from Bi_2O_3 (MCP Industries, Lubek, Germany), Sc_2O_3 (PIDC, Ann Arbor, MI) and stoichiometric $BaTiO_3$ (Transelco, Penn Yan, NY) powders. 5 mol% excess Bi_2O_3 was used to compensate for Bi volatility during the deposition process [51]. Powders were combined in a polyethylene jar and ball milled in ethanol for 1-2 days using ZrO_2 milling media. After being dried in an 80°C oven for 24 hours, the powders were ground in a mortar and pestle and passed through an 80 mesh sieve. An acrylic binder system (Acryloid Resin, Rohm and Haas) was added in a 5 wt% ratio of binder/powder. The binder was diluted with acetone, added to the powder, and mixed until a thick paste formed. The powder-binder composite was dried in air and ground in a mortar and pestle until a fine powder was obtained. The powder plus binder was then isostatically pressed at 125 MPa in a cylindrical die in order to provide sufficient compact strength to facilitate sintering. The pressed compact was set on MgO sand on a refractory ceramic and placed in the sintering furnace. During the sintering run, the target was given a three hour soak at 300°C to initiate binder burnout. The binder burnout was completed during a 90 minute soak at 550°C. Liquid phase sintering of the targets occurred at 850°C (Bi_2O_3 melts at 840°C [97]). This allowed for sufficient densification to occur so that the targets were mechanically stable (i.e. not easily polished) and had little observable surface porosity in an optical microscope. The resulting targets were a multi-phase ensemble as shown in Fig. 3.2.

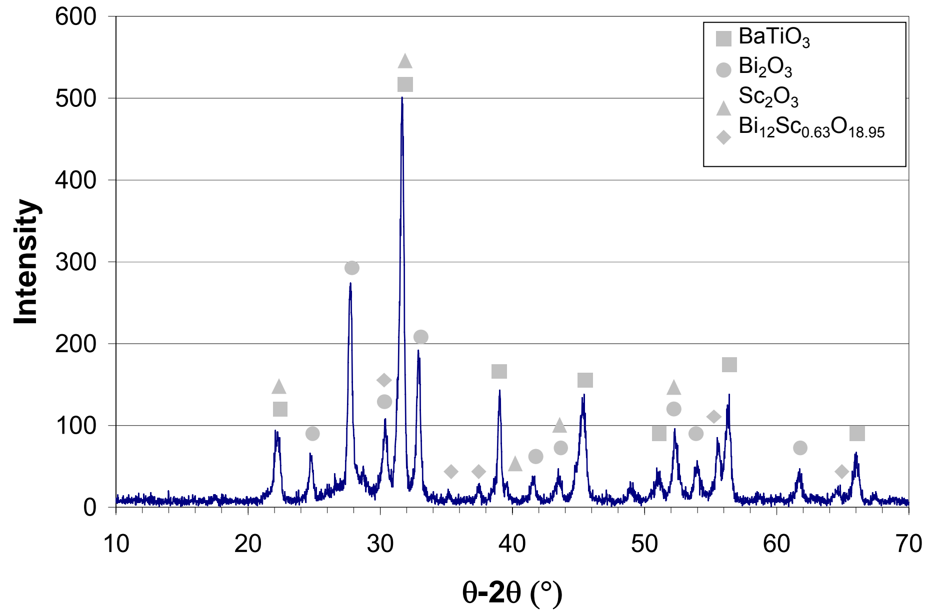

Fig. 3.2. X-ray diffraction pattern from a $0.4BiScO_3$-$0.6BaTiO_3$ target showing multiple phases present.

3.3 Vacuum System

The vacuum system used in this study was designed by Maffei [98] for pulsed laser deposition and upgraded by Maria [43]. A schematic of the pulsed laser deposition system is given in Fig. 3.3 [80]. A Varian model M6 diffusion pump with fluorinated oil (Solvey Solexis, Thorofare, NJ) was used to maintain a base pressure of 1 x 10^{-6} Torr. An Alcatel rotary pump was used as a backing and roughing pump. A Bayard-Alpert ion gauge (Duniway Stockroom Corp, Mountain View, CA) was used to determine the base pressure. During deposition, a convectron style gauge was used to monitor pressure.

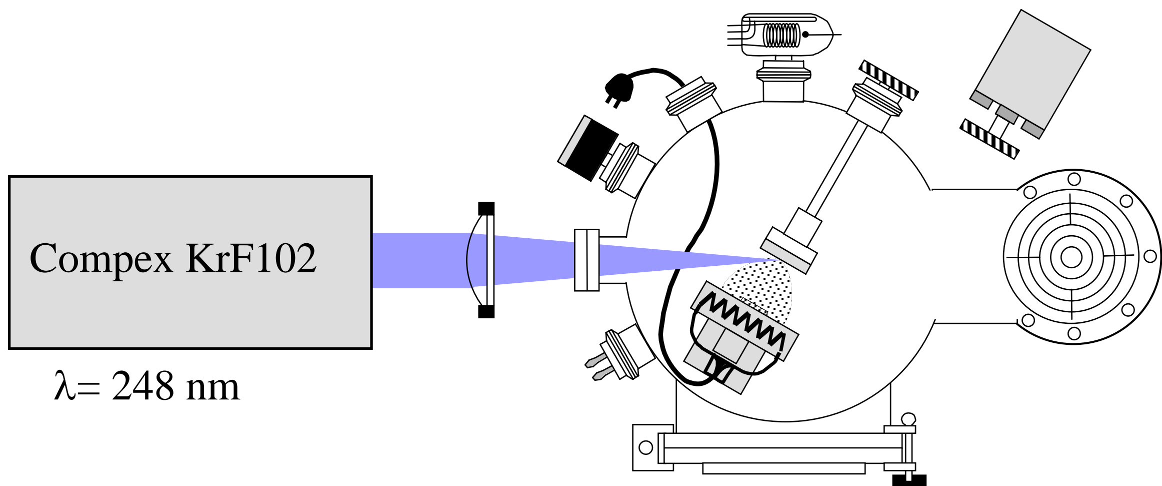

Fig. 3.3. Schematic of pulsed laser deposition setup used for these experiments [80].

The process gas used for the system is a 10%/90% mixture of O_3/O_2 output from a PCI-G1 ozone generator. Ultra-high purity (UHP) oxygen was used as the source gas for the ozone generator. A MKS model 179A (MKS Instruments, Wilmington MA) flowmeter set at a flowrate of 50 sccm was used to introduce the ambient gas to the growth chamber. With the gate valve open, a minimum deposition pressure of 5 mTorr was achieved. Deposition pressures above 5 mTorr were obtained through constriction of the gate valve between the deposition chamber and the diffusion pump.

The block heater used to control the substrate temperature was constructed using 304 stainless steel and was resistively heated. Using a winding of Inconel sheathed nickel-chromium wire produced by Thermocoax, temperatures in excess of 700°C were achieved. The temperature of the heater block was monitored via an Omega K-type thermocouple embedded into the center of the heater block. A Hewlett Packard model

6268B direct current supply was used as a power supply for the heater. The amount of power required to reach 700°C was on the order of 250 W. The heater block was mounted on an independent stand, which allowed different target-to-substrate distances up to 8 cm to be used.

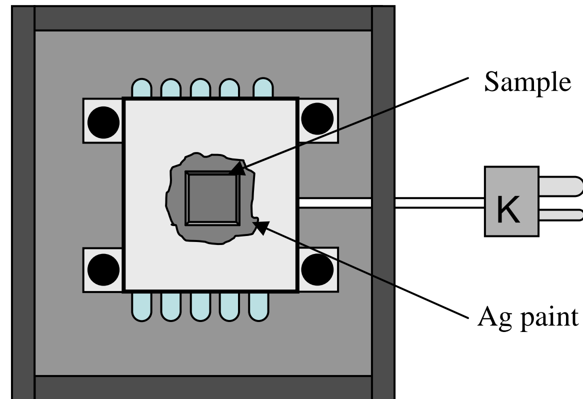

Fig. 3.4. Schematic of heater block used in this project.

Substrates were bonded to the heater block using silver paint to ensure good thermal contact. (100) $LaAlO_3$ substrates were purchased from MTI Crystal Inc. (Richmond, CA), while Pt-coated Si samples were purchased from Nova Electronic Materials Ltd. (Carrollton, TX). The Pt-coated Si substrates had a 10,000 Å SiO_2 layer with a 1000 Å Pt layer on top of a 250 A Ti adhesion layer. Substrates were cleaned by sonicating for five minutes in ethanol, methanol, and isopropanol, successively, and blown dry using a dry Ar jet.

The laser used in this study is a KrF laser (Lambda Physik Compex 102, Fort Lauderdale, FL) which emits 248 nm ultraviolet radiation. A fused quartz window was used to pass the beam into the vacuum chamber. A plano-convex lens focused the laser

to a spot size of ~ 2 mm x 2 mm at the target surface. The energy density at the target surface was ~2 J/cm^2 [81]. The targets were mounted on a rotary feed-through which allowed the target to be rotated during deposition so that subsequent laser pulses impinged at different locations on the surface.

3.4 Pulsed Laser Deposition of $xBiScO_3$-(1-x)$BaTiO_3$ Thin Films

As mentioned in chapter 2, pulsed laser deposition was used to deposit the films in this study. To optimize the quality of the grown films, several deposition parameters were investigated. First, to determine the morphotropic phase boundary, films were grown from targets with various $BiScO_3$:$BaTiO_3$ ratios. Following the work of Maria on $BaTiO_3$ growth, a substrate temperature of 700°C and a growth pressure of 100 mTorr O_2/O_3 were used in initial exploration [43]. A design of experiments was performed around these conditions varying temperature, pressure, and composition with the ranges of deposition parameters given in Table 3.2. Temperature and pressure were independently varied for a composition of 40% $BiScO_3$. A laser repetition rate of 5 Hz was used except in instances where the desired thickness of the film required the deposition length to exceed 2 hours. Lastly, the target-substrate distance was altered from 6 cm to 8 cm to determine if reducing the bombardment without increasing the pressure had any effect on film properties.

Table 3.2. List of deposition parameters used in the study.

Composition (mol% $BiScO_3$)	Temperature (°C)	Pressure (mTorr O_2/O_3)	Time (min)
20-60	450-750	15-400	5-120

Films were grown on either Pt-coated Si or (001) $LaAlO_3$ substrates. Single crystal $LaAlO_3$ were first cleaned and adhered to the heater block using silver paint and heated to ~120°C for ~20 minutes to remove solvent and provide a solid bond between the heater block and sample. Deposition of the $SrRuO_3$ (Target Materials Inc., Columbus, OH) bottom electrode was done following the procedure of Maria [46]. For deposition of the $xBiScO_3$-$(1-x)BaTiO_3$ films, the heater was aligned parallel to the target surface. The default target-to-substrate distance used was 8 cm, which kept the substrate out of the plume. During evacuation of the chamber, the sample was heated to the deposition temperature. Prior to deposition, O_2/O_3 was fed into the chamber and the gate valve was throttled to give the desired process pressure. The deposition length was varied to control the thickness the film. After film deposition, the gate valve was closed and the process gas was allowed to fill the chamber until a pressure of 3 Torr was achieved. Two anneals were performed during cooling to reduce the concentration of oxygen vacancies in the films. Samples were held at ~550°C, or their deposition temperature if lower than 550°C, for 30 minutes, then cooled to 350°C for 30 minutes prior to cooling to room temperature.

3.5 Structural Characterization

3.5.1 2-Circle X-Ray Diffraction

A Scintag powder diffractometer operating in θ-2θ mode was used in this study for phase identification and to measure the crystallographic texture of the films. Typical settings on the instrument were 35 kV and 30 mA. Films on single crystal oxide substrates and Pt-coated Si were both investigated. Using Jade x-ray analysis software (Materials Data Inc., Livermore, CA), *d*-spacings were extracted from the scans and fitted using the Nelson-Riley function [99]. The Nelson-Riley function corrects for systematic errors originating from the diffractometer which may give incorrect values of d-spacings.

3.5.2 4-Circle X-Ray Diffraction

Out-of-plane lattice parameters were investigated using a Philips X'pert Pro MRD High resolution 4-circle diffractometer (PANalytical Inc., Tempe, AZ) equipped with high temperature stage capabilities. The diffractometer was equipped with a hybrid graphite monochromator which selectively collimated Cu $K_{\alpha 1}$ radiation. The detector arm of the goiniometer had two detectors, one allowing for regular diffraction conditions, and the second with a tri-crystal analyzer, giving higher resolution capabilities for techniques such as reciprocal space mapping. A schematic of typical 4-circle diffractometer geometry is shown in Fig. 3.5.

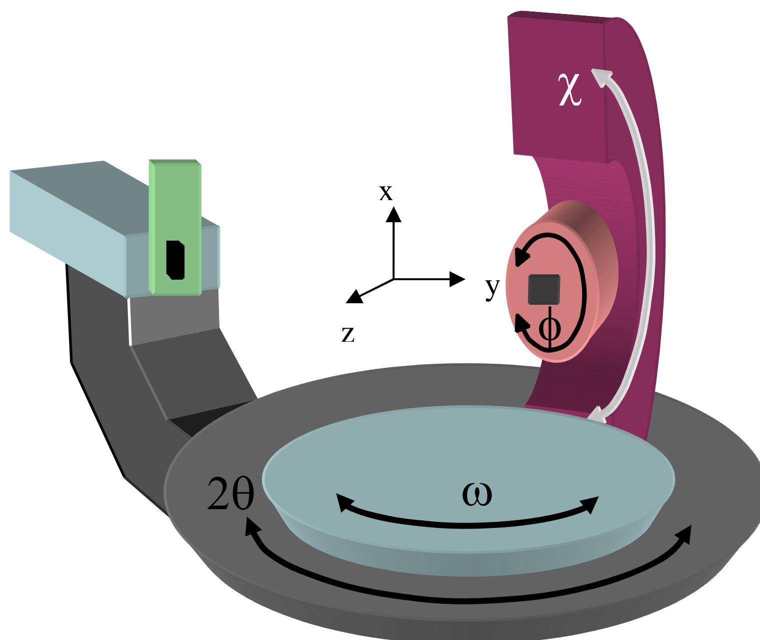

Fig. 3.5. Schematic of a typical 4-circle x-ray diffractometer setup.

Samples were mounted on a glass slide using double sided tape and were centered on the stage. The zero of the x-ray beam was found and the sample was moved in the *z*-direction until the beam intensity was cut in half. The sample was rocked in the ω-axis to align the sample surface parallel to the direction of the x-ray beam and realigned in the *z*-direction. The sample was then moved to a substrate peak to align the goiniometer to the miscut in the single crystal. After a sample was aligned to a substrate peak, θ-2θ scans were performed and ω-scans (rocking curves) were measured on the film peaks to determine mosaicity. These scans were repeated for off-axis peaks. Additional scans in the ϕ direction were performed to determine the crystallographic texture of the films as well as obtain information on the out of plane lattice parameters.

3.6 Morphological Characterization

A Hitachi S-3500N scanning electron microscope with attached energy dispersive spectroscopy (EDS) was used to investigate surface morphology and thickness. Samples were fractured to provide a clean interface for cross-sectional imaging. Prior to imaging, samples were cleaned and sputtered with gold to prevent charging. The attached software package with the SEM, with subsequent confirmation from Adobe Photoshop, allowed calculation of the thickness of the films from cross-sectional images. Additionally, secondary electron images were obtained to determine the grain size and morphology of the films.

3.7 Electrical Property Measurements

The dielectric properties of the films were characterized via capacitor structures shown schematically in Fig. 3.6. Films were deposited on a bottom electrode. Calculation of the permittivity was done using the equation:

$$C = \varepsilon_o \varepsilon_r \frac{A}{d}, \quad (3.2)$$

where C is capacitance, ε_o and ε_r are the permittivity of free space and the relative permittivity respectively, A is area of the capacitor, and d is the thickness.

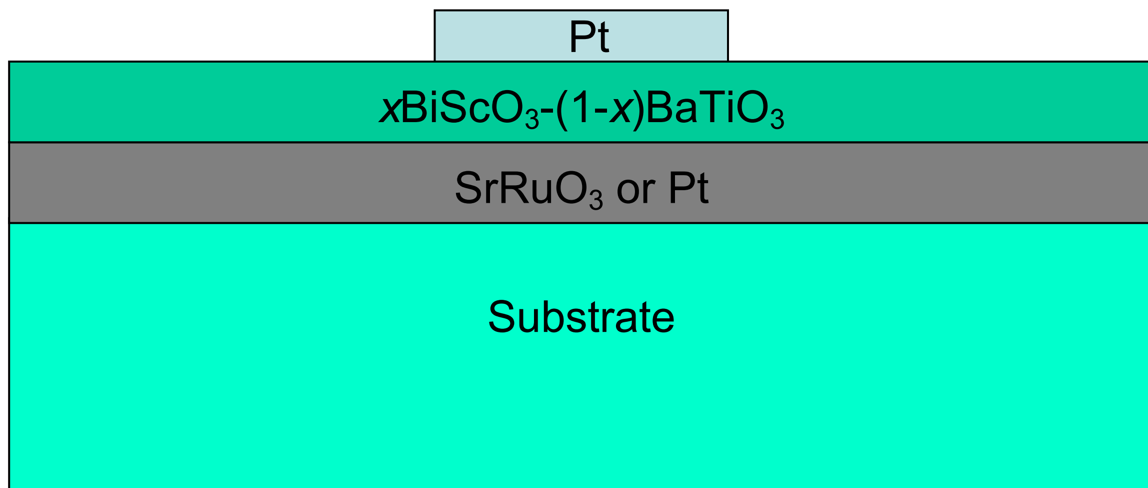

Fig. 3.6. Schematic of thin film capacitors used in this study.

Photolithography was performed to pattern the top electrodes. The top electrode area ranged from ~75 μm^2 to 0.04 mm^2. Shipley 1811 photoresist was used in conjunction with LOR 5A lift-off resist (MicroChem Corp. Newton, MA) to pattern the electrodes. Samples were cleaned using acetone and isopropanol as solvents. They were then dried using a dry nitrogen jet and a ~10 s bake at 100 °C. Lift-off resist was spun on the samples at 4000 rpm for 45 s prior to a bake at 180 °C for 2 minutes to remove excess solvents. Photoresist was spun at 4000 rpm for 45 s followed by a soft bake at 100°C for 1 minute. UV exposure was performed using an Hg vapor lamp operating at ~300 W for 30 s. The photoresist and lift-off resist were developed using CD-26 (Shipley, Marlboro MA) until clear undercutting of the photoresist was observed using an optical microscope. After developing, the samples were cleaned using de-ionized water and dried using a dry-N_2 jet.

The Pt-top electrode was sputtered using the W.M. Keck Smart Materials Integration Laboratory Lesker CMS-18 sputter system. The system involves a high vacuum chamber with a RF magnetron sputter gun. Typical operating Ar pressures were 2.5 mTorr. The typical thickness of the top electrodes was 100 nm. Excess Pt and photoresist were removed using acetone while the remaining lift-off resist was removed using a developer. Prior to electrical measurements, the samples were annealed in air at 550-650°C to provide a good interface between the metal and dielectric. This is done to minimize space charge contributions to the measurements.

Most measurements were made using a pair of point probes. Contact to the top electrode consisted of making physical contact between the point probe and the Pt electrode. Contacting the bottom electrode was done through a shorted electrode or by etching the dielectric using a buffered HF solution to reveal the bottom electrode. Polarization hysteresis loops were measured using a RT66A Ferroelectrics tester (Radiant Technologies, Albuquerque, NM). When the voltage required for hysteresis loops exceeded the RT66's 20V limit, a 10:1 voltage amplifier (AVC, Div. of PCB Piezotronics Inc., Depew, NY) was used. Capacitance and loss measurements were made using a Hewlett Packard 4192A LF impedance analyzer (Agilent Technology, Palo Alto, CA) on a probe station equipped with a high temperature stage. LabView programs were used to record the capacitance and loss data as a function of frequency (0.1-1000 kHz), applied DC bias (0-20V) and temperature between room temperature and 400°C using a 30 mV AC field excitation.

For low temperature measurements, samples were mounted to a 24 pin chip package using Ag paint. The samples were dried for 2 hours at ~100°C to provide a solid bond to the package. Wirebonding was used for contact to the electrodes. The samples were wirebonded using a Kulicke and Soffa model 4123 wedge bonder (Fort Washington, PA). 1.0 mil Au wire was used to make the electrical connections. The bonding parameters used was a temperature of 45°C, power of 1.8 W, time of 50 ms and dynamic force of 6.5 grams. Once the samples were wire bonded, the samples were mounted in a Delta Design model Delta 9023 oven (San Diego, CA). The Delta oven was equipped with a liquid nitrogen cooling apparatus, and capable of temperatures in the range of -180 °C – 200 °C. The capacitance and loss values were measured using a HP4284A LCR meter with a HP 69408 Multiprogrammer relay (Hewlett Packard, Palo Alto, CA) so that individual pins on the package could be selected. The temperature was monitored using a K-type thermocouple mounted directly beneath the sample.

4.0 Results and Discussion

The crystal structure of the films was investigated as a function of composition and deposition conditions. The location of the morphotropic phase boundary was determined based on a combination of structural and electrical measurements. Finally, the low and high field dielectric properties of epitaxial and polycrystalline films were measured.

4.1 X-ray Characterization of $xBiScO_3$-(1-x)$BaTiO_3$ Thin Films

X-ray diffraction was used to investigate the phase and crystallinity of the films. 2-circle x-ray diffraction was performed after deposition to determine the phase purity of the films prior to dielectric measurements. Lattice parameters were determined as a function of film composition and deposition parameters. 4-circle diffraction was used to measure in-plane and out-of-plane lattice constants.

4.1.1 $SrRuO_3$ Deposition and $xBiScO_3$-(1-x)$BaTiO_3$ Perovskite Phase Formation

Initial experiments were conducted by growing $x$$BiScO_3$-(1-$x$)$BaTiO_3$ (BSBT) films on single crystal oxide substrates in an attempt to utilize epitaxy to increase the stability of the perovskite phase. $LaAlO_3$ single crystal substrates were chosen for their moderate price. The small lattice parameter (a = 3.821Å) of $LaAlO_3$ also leads to relaxation of films at small thicknesses. For dielectric measurements of thin films on $LaAlO_3$, $SrRuO_3$ was deposited to be used as a bottom electrode. $SrRuO_3$ was chosen as the bottom electrode material due to its low resistivity (~300 μΩ-cm at room temperature) and reasonable lattice match to $LaAlO_3$ (a = 3.821Å) [46]. The deposition

conditions used for $SrRuO_3$ were a substrate temperature of 680°C and 160 mTorr O_2/O_3, which were shown to produce good quality films [46]. Using these conditions, well oriented $SrRuO_3$ was deposited on $LaAlO_3$ as evidenced in Fig. 4.1. 80 nm thick $SrRuO_3$ films were used as electrodes throughout this thesis.

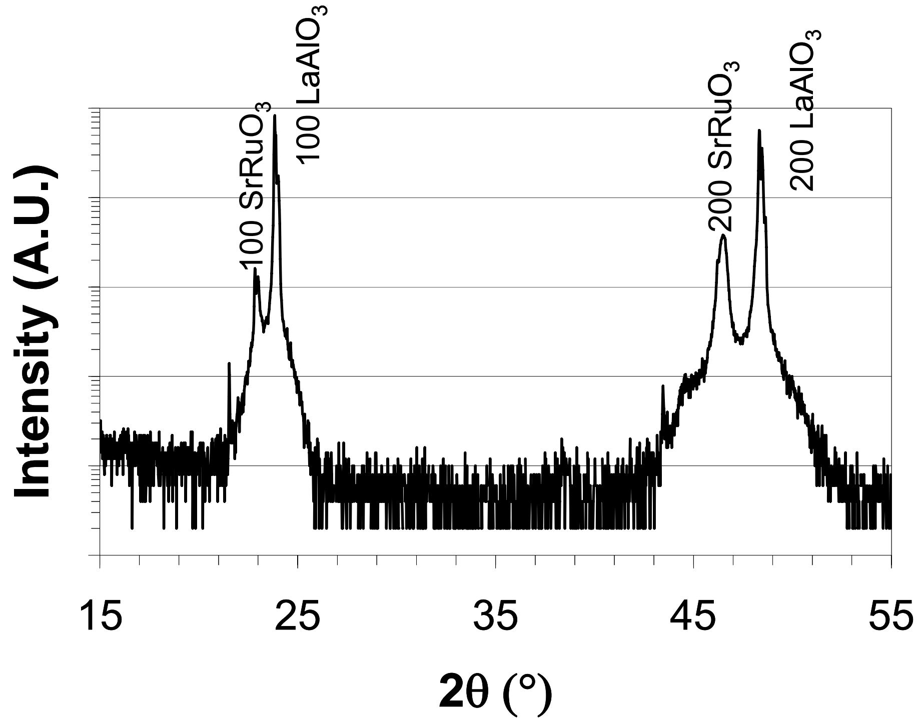

Fig. 4.1. X-ray diffraction pattern for $SrRuO_3$ deposited on $LaAlO_3$. Here and throughout the chapter, unless otherwise noted, all perovskite peaks are indexed in terms of a pseudocubic unit cell.

After successful deposition of the $SrRuO_3$ bottom electrode, $0.2BiScO_3$-$0.8BaTiO_3$ films were grown on $SrRuO_3/LaAlO_3$. This composition was chosen since the

high $BaTiO_3$ concentration should yield a stable tetragonal perovskite structure as predicted by tolerance factor calculations. Films were grown using the base conditions of a substrate temperature of 700 °C and a background gas of 100 mTorr O_2/O_3, adapted from the work of Maria on epitaxial $BaTiO_3$ deposition [43]. Using x-ray diffraction, it was shown that epitaxial growth of $0.2BiScO_3$-$0.8BaTiO_3$ occurs under these conditions, as evidenced in Fig. 4.2.

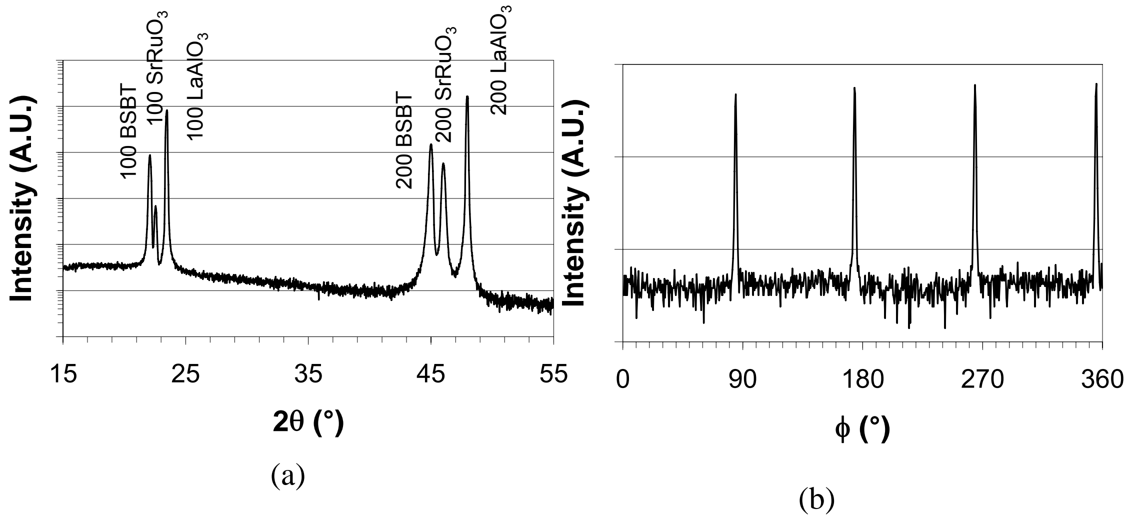

Fig. 4.2 X-ray diffraction patterns for $0.2BiScO_3$-$0.8BaTiO_3$ (BSBT) on $SrRuO_3/LaAlO_3$. (a) θ-2θ scan of the 100 peaks and (b) ϕ scan of 101 peaks showing 4 fold symmetry characteristic of in-plane alignment.

After epitaxial deposition of $0.2BiScO_3$-$0.8BaTiO_3$ on $SrRuO_3/LaAlO_3$ was shown, the issue of perovskite stability across the compositional range was investigated.

Thin films of composition $x = 0.2-0.6$ were deposited at 700°C and 100 mTorr O_2/O_3. It was found that all compositions within this range were epitaxial as deposited on (100) $SrRuO_3/LaAlO_3$. Fig. 4.3a shows a comparison of the x-ray data collected for all compositions. Fig. 4.3b shows a ϕ scan of the 101 film peak for a composition of $x = 0.6$. The absence of secondary peaks in this scan indicates that films are epitaxial up to a composition of $x = 0.6$.

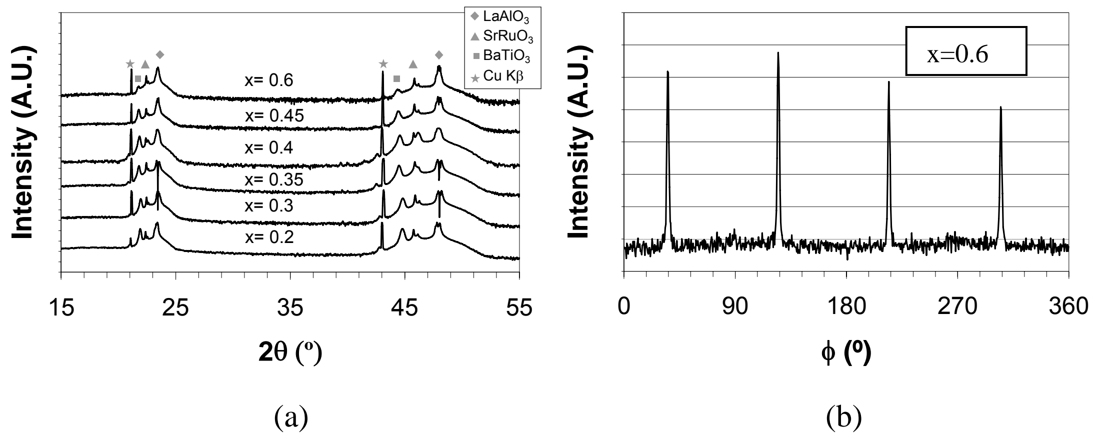

Fig. 4.3. a) Compilation of x-ray patterns for xBiScO$_3$-(1-x)BaTiO$_3$ on (100)$SrRuO_3/LaAlO_3$ and b) 101 ϕ scan for 0.6BiScO$_3$-0.4BaTiO$_3$ thin film.

Since the stability of the perovskite structure was established in epitaxial thin film form, polycrystalline films were deposited on Pt-coated silicon. As with epitaxial samples, 0.2BiScO$_3$-0.8BaTiO$_3$ was used to initially test the stability of the perovskite phase on Pt-coated silicon substrates using the previous deposition conditions. As can be seen in Fig. 4.4a, films with x=0.2 form a stable perovskite phase on Pt-coated silicon.

After perovskite phase formation was confirmed, other compositions were deposited on Pt-coated silicon substrates. It was found that films with the composition of x=0.2-0.45 formed a stable perovskite phase, while films with a composition of x=0.6 have prominent second phase peaks as shown in Fig. 4.4b. There are several important conclusions to draw from this. Firstly, epitaxy is believed to extend the perovskite stability limits for films on (100)$SrRuO_3$/$LaAlO_3$ [100]. Secondly, the appearance of the perovskite phase for $x \leq 0.45$ in the absence of substrate-induced stabilization suggests that bulk ceramics of the same composition should be possible to make.

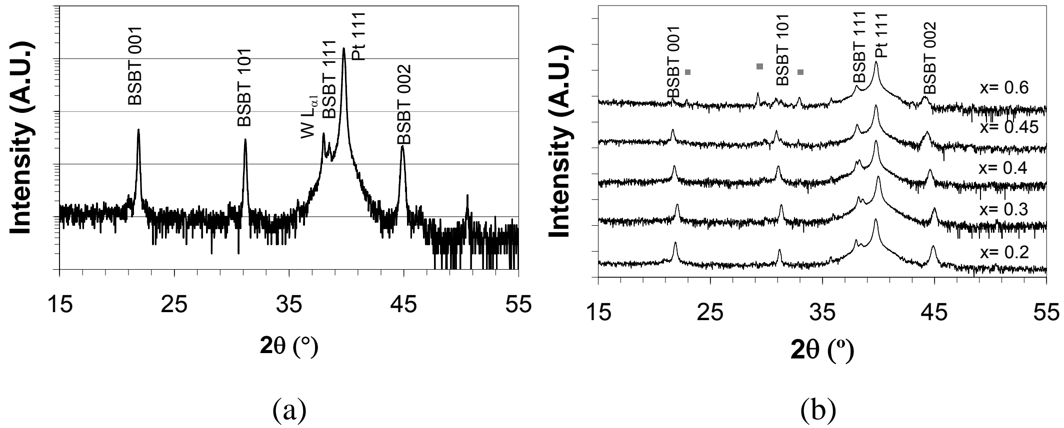

Fig. 4.4. (a) 0.2 $BiScO_3$-$BaTiO_3$ on Pt-coated Si. The $W_{L\alpha}$ line is due to contamination of the Cu x-ray source from the W filament. (b) compilation of x-ray patterns for $x$$BiScO_3$-(1-$x$)$BaTiO_3$ films with x= 0.2-0.6 on Pt-coated Si. Starred peaks correspond to a second phase.

The polycrystalline films exhibited different morphology compared with the epitaxial samples as illustrated in Fig. 4.5. For polycrystalline samples, the films exhibited a columnar grain structure similar to a zone 2 type film, as shown in Fig. 4.5c. For epitaxial films however, it was difficult to resolve individual grains via scanning electron microscopy. The textured natured of the epitaxial films was confirmed using full-width half-maximum (FWHM) scans. Additionally, the epitaxial nature of the films grown on $SrRuO_3/LaAlO_3$ made it difficult to resolve the morphology in a cross-sectional scanning electron micrograph (Fig. 4.5d).

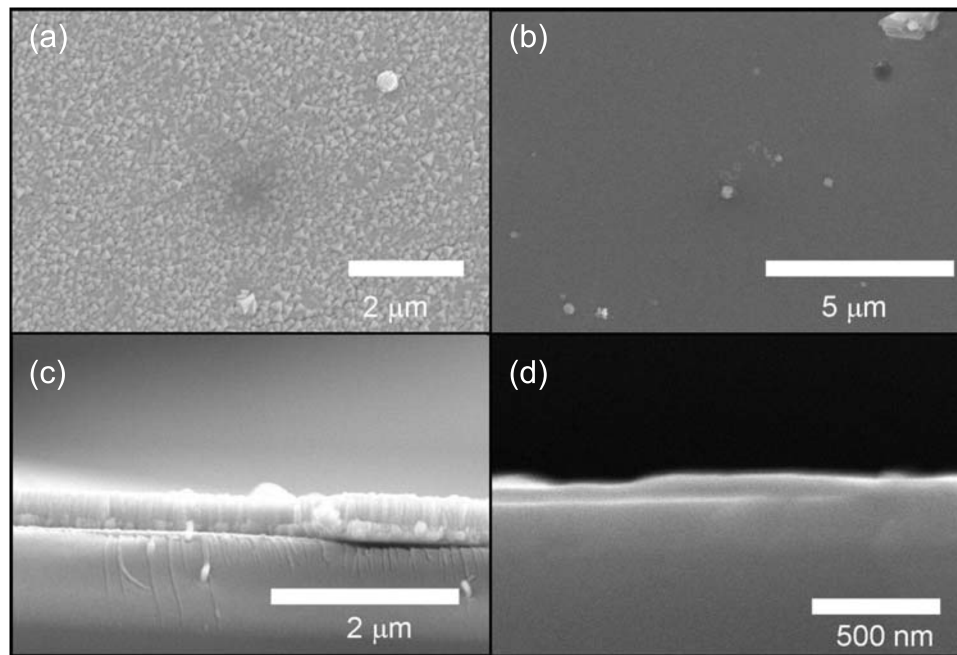

Fig. 4.5. Scanning electron micrographs illustrating the difference in morphology of the polycrystalline ((a) and (c)) vs. epitaxial films ((b) and (d)).

4.1.2 Lattice Parameter Analysis

During x-ray diffraction measurements, errors inherent to the diffractometer and setup can lead to errors in the measured d-spacing. In this thesis, the Nelson-Riley method was used to extrapolate the d-spacing for particular crystallographic planes in order to calculate corrected lattice parameters [99]. X-ray patterns from 2-circle and 4-circle measurements such as those in Fig. 4.6, were analyzed for the peak positions in 2θ using Jade X-ray analysis software.

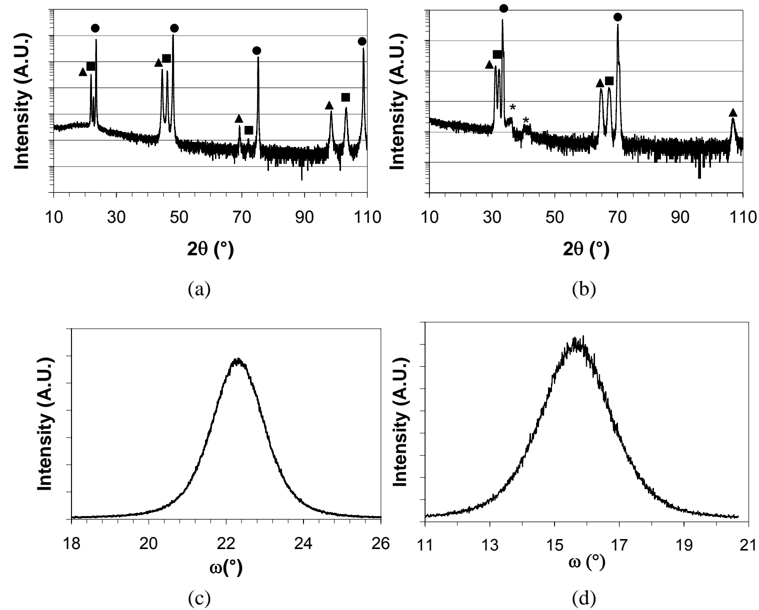

Fig. 4.6. X-ray diffraction patterns for a $0.4BiScO_3$-$0.6BaTiO_3$ film (triangles) deposited at 700°C and 100 mTorr O_2/O_3 on $SrRuO_3/LaAlO_3$ (squares/circles). (a) 100 family and (b) 101 family of planes and FWHM for the (c) 200 peak and (d) 101 peak. Starred peaks stem from the substrate holder.

The 2θ value for each peak was used to calculate a d-spacing using Bragg's law [94]:

$$\lambda = 2d\sin\theta, \quad (4.1)$$

where λ is the wavelength of the radiation used, d is the interplanar spacing of the family of planes, and θ is defined as half the measured 2θ value. Using the Nelson-Riley method [99], the experimental d-spacings were plotted against a function $F(\theta)$:

$$F(\theta) = \frac{1}{2}\left(\frac{\cos^2\theta}{\sin\theta} + \frac{\cos^2\theta}{\theta}\right), \quad (4.2)$$

where θ is given in radians. The corrected d spacing is the y intercept of the graph. These corrected values were used to calculate accurate lattice parameters of the film.

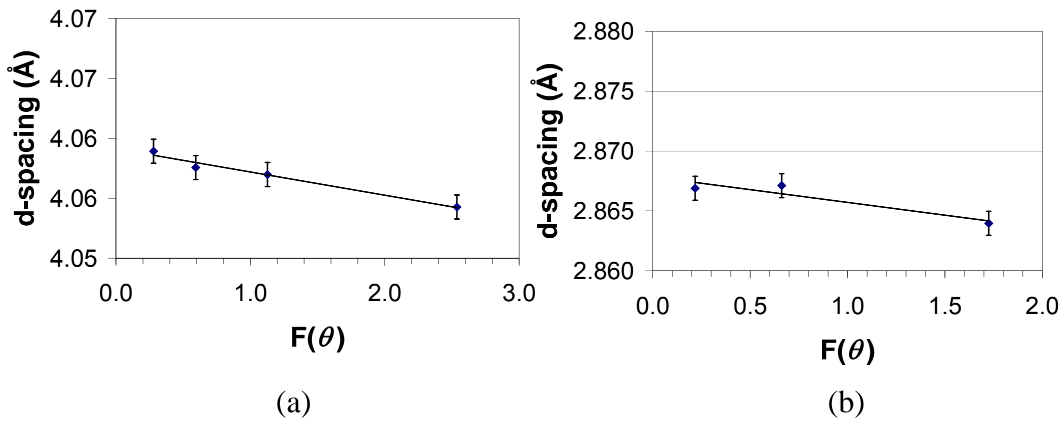

(a) (b)

Fig. 4.7. Nelson-Riley plots for epitaxial 0.4$BiScO_3$-0.6$BaTiO_3$ films deposited at 700°C and 100 mTorr O_2/O_3 (a) 100 family and (b) 101 family of planes.

4.1.3 Deposition Parameter Study

The limits of perovskite stability were next determined as a function of deposition parameters. A film composition of x=0.4 was chosen due to its location near the predicted morphotropic phase boundary as shown in Fig. 3.2. During the deposition temperature study, the substrate temperature, T_S, was varied while all other parameters were kept constant (100 mTorr O_2/O_3, 5 Hz repetition rate and target-to-substrate distance of 8 cm). It was found that $0.4BiScO_3$-$0.6BaTiO_3$ on $SrRuO_3$ formed the perovskite phase at substrate temperatures as low as 450°C, as shown in Fig. 4.8a. In contrast, as shown in Fig. 4.8b, films of the same composition deposited on Pt-coated silicon crystallize at substrate temperatures $\geq$500°C. From this it can be concluded that the textured growth of films deposited on $SrRuO_3/LaAlO_3$ aids in nucleation of the films during deposition, which allows growth of crystalline films at lower temperatures.

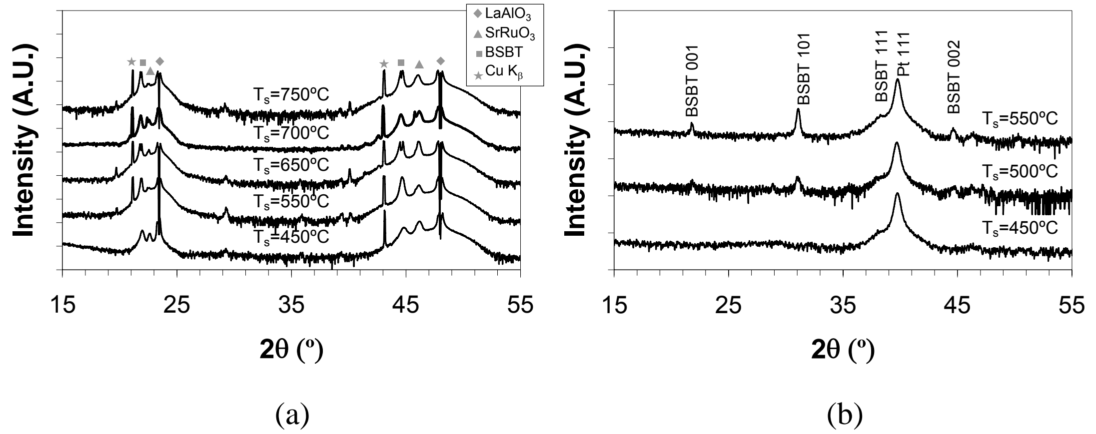

Fig. 4.8. X-ray diffraction patterns for $0.4BiScO_3$-$0.6BaTiO_3$ as a function of substrate temperature on (a) $SrRuO_3/LaAlO_3$ and (b) Pt-coated Si.

The effect of the substrate temperature during deposition on the room temperature out-of-plane lattice parameter is shown in Fig. 4.9. The out-of-plane lattice parameter increases with increasing deposition temperature up until ~700°C, where it appears to saturate. Several factors were considered as possible origins for this behavior. First, bombardment-induced swelling of the lattice was ruled out. All films were deposited at the same pressure and target-to-substrate distances. Thus, the bombardment of the growing film should be comparable for all growth temperatures. Indeed, since higher substrate temperatures provide larger adatom mobilities, any bombardment-induced swelling of the lattice parameter would be expected to be relaxed, rather than exacerbated, at higher temperatures. Thus, this could not account for the observed behavior. Secondly, in order to estimate whether thermal expansion mismatches were

responsible for the observed increase in lattice parameter with deposition temperature, the in-plane thermal strain was calculated using equation 2.14. Because the depositions occur at temperatures where both the film and the substrate are cubic perovskites, thermal expansion coefficients for the cubic prototype phases of the two materials were employed (12 ppm/°C for $LaAlO_3$ and 14.5 ppm/°C for the film [43]). Unfortunately, no thermal expansion values are available in the literature for $0.4BiScO_3$-$0.6BaTiO_3$, thus the thermal expansion coefficient for $BaTiO_3$ was used as a first approximation. The calculated in-plane thermal strain was tensile, with a magnitude of 0.1% to 0.2% for growth temperatures of 450°C-750°C. This change is too small to account for the observed expansion of the lattice parameters. Moreover, it should have *reduced*, rather than *increased* the out-of-plane lattice parameter. Therefore, some other mechanism must be responsible for the observed changes in lattice parameter as a function of temperature. Third, bismuth has the possibility of ionizing to form Bi^{5+} which could be accommodated on the B-site of the perovskite. Bi^{5+}, being larger than both Sc^{3+} and Ti^{4+}, would then result in an expansion of the lattice. However, the amount of Bi^{5+} on the B-site required to expand the lattice as observed is on the order of 10% which is unrealistically large. This is unrealistically large because this would require all the excess bismuth in the system to be ionized into Bi^{5+} and would preclude bismuth from volatilizing during growth. Additional work to establish the mechanism for this is essential. In all remaining experiments, the substrate temperature was chosen to be 700°C.

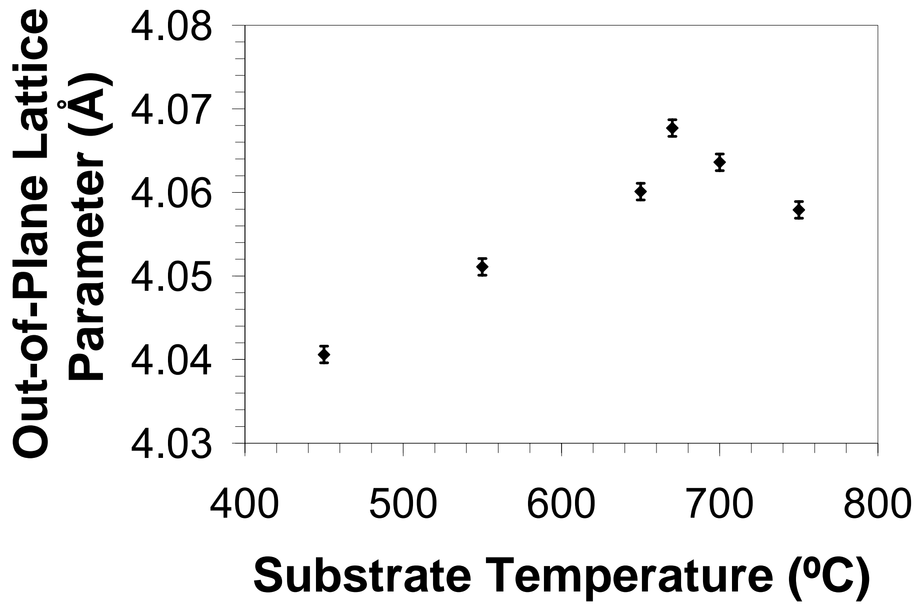

Fig. 4.9. Out-of-plane lattice parameter as a function of substrate temperature for epitaxial $0.4BiScO_3$-$0.6BaTiO_3$ thin films deposited at an ambient pressure of 100 mTorr O_2/O_3 and a target-substrate distance of 8 cm.

Images of the surface of the films were taken using a scanning electron microscope and are shown in Fig. 4.10. Micrographs were taken from samples deposited between 550°C and 750°C. Modest changes in microstructure are apparent as a function of deposition temperature.

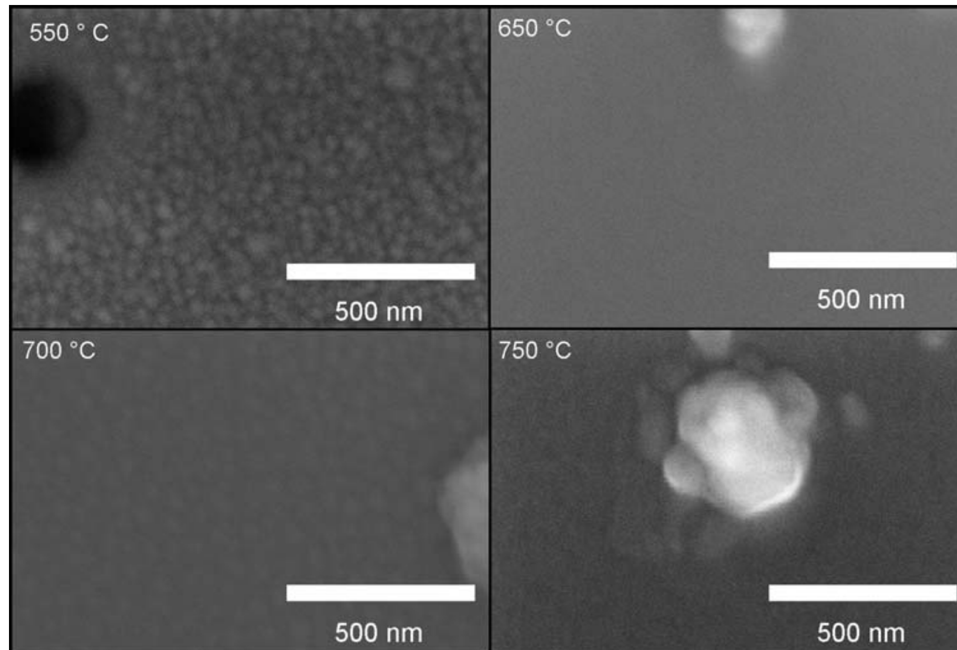

Fig. 4.10. Scanning electron micrograph of the surface of $0.4BiScO_3$-$0.6BaTiO_3$/SRO/LAO thin films as a function of deposition temperature. Particles on the surface were used to facilitate focusing.

During pulsed laser deposition, the pressure in the chamber can have a significant effect on film quality as discussed previously. The deposition pressure for this system was varied between 15 mTorr O_2/O_3 and 400 mTorr O_2/O_3. The out-of-plane lattice parameter is shown to increase as the chamber pressure is reduced, with a dramatic increase at pressures below 50 mTorr as shown in Fig. 4.11a. Comparable effects have been seen previously in vapor-phase deposition of other perovskites, and is most likely due to bombardment induced expansion of the lattice [46, 85, 93]. That is, at low

pressures, there is less collision-induced thermalization of the plume, so that bombardment of the growing films increases.

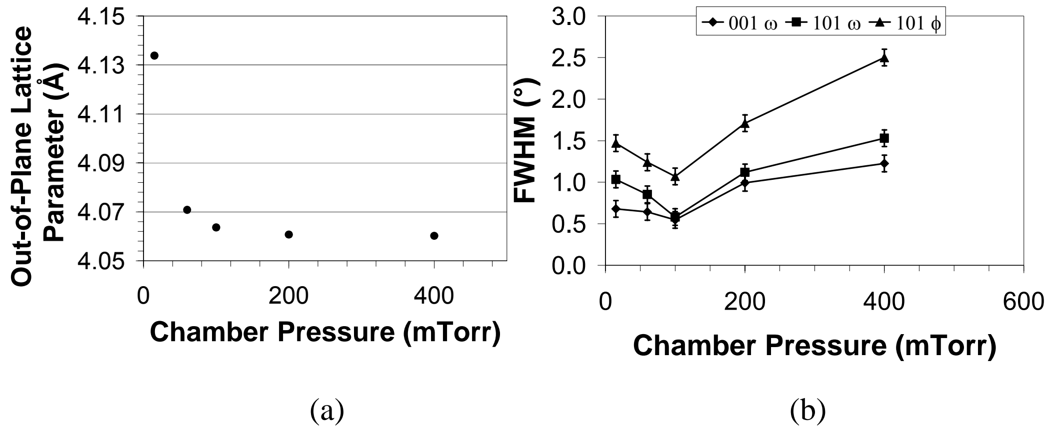

(a) (b)

Fig. 4.11. (a) Out of plane lattice parameter as a function of chamber pressure for a $0.4BiScO_3$-$0.6BaTiO_3$ thin film deposited at 700°C and (b) Full-Width at Half Maximum (FWHM) for $0.4BiScO_3$-$0.6BaTiO_3$ films deposited at 700°C at various chamber pressures.

A good measure of crystalline quality is the full-width half maximum (FWHM) of the rocking curve. The rocking curve is generally collected by fixing the detector position in 2θ, and measuring the intensity as ω is changed. (See the schematic of a 4-circle x-ray diffractometer in Fig. 3.4). Epitaxial films can be considered as an ensemble of slightly misaligned grains as shown schematically in Fig 2.31. By "rocking" the ω axis of the diffractometer, grains with different orientations will be brought into the

Bragg condition and the intensity recorded by the detector will change. Thus, a smaller FWHM for the rocking curve indicates higher crystal quality. Fig. 4.11b shows a graph of the measured FWHM for $0.4BiScO_3$-$0.6BaTiO_3$ thin films deposited at 700°C under different chamber pressures. From this graph it is clear that the highest quality film is produced using 100 mTorr O_2/O_3. At pressures lower than 100 mTorr, the increase in FWHM most likely stems from ion bombardment. Comparable behavior has been previously reported in PLD oxide films [46].

Scanning electron micrographs showed that there was a small increase in the surface grain size as the deposition pressure increased (Fig. 4.12) [46]. As the growth pressure was increased from 60 mTorr to 400 mTorr for a $0.4BiScO_3$-$0.6BaTiO_3$ thin film on $SrRuO_3/LaAlO_3$, the surface of the films appear to roughen. This corresponds well with the structure zone model which states that increasing the bombardment of the film (i.e. decreasing chamber pressure) will increase the adatom mobility on the surface of the film resulting in a smoother film. In all remaining experiments, the ambient pressure used was 100 mTorr O_2/O_3.

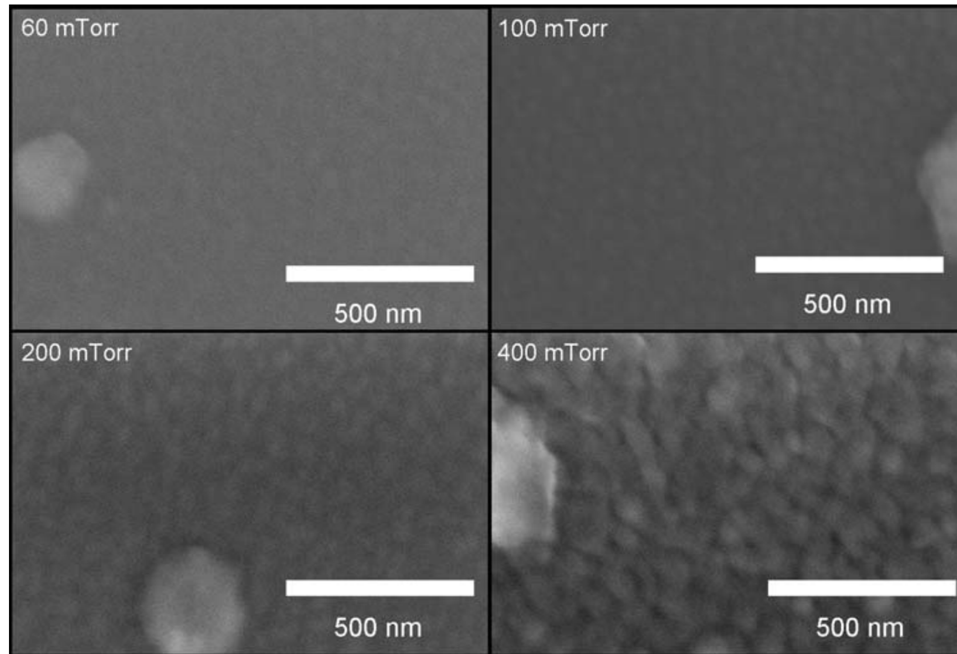

Fig. 4.12. Scanning electron microscope images of the surface of $0.4BiScO_3$-$0.6BaTiO_3$/SRO/LAO thin films as a function of deposition pressure.

Based on the substrate temperature and deposition pressure studies, the deposition conditions of 700°C, 100 mTorr O_2/O_3, and a target to substrate distance of 8 cm were chosen. Films were grown in the composition range x=0.2-0.6 on (100) $SrRuO_3/LaAlO_3$ and Pt-coated Si. The lattice parameters were measured in and out-of-the plane of the film, calculated assuming tetragonal symmetry, are plotted in Fig. 4.13. From this it is clear that the films split into a tetragonal symmetry at compositions below x= 0.4 with the long axis in the plane of the film. The tetragonality of all of the films measured was modest, typically on the order of 0.8% for x = 0.2. For higher x, the films were pseudocubic. This is indicative of a morphotropic phase boundary in the material. From

these results, we would expect enhanced dielectric properties around a composition of x=0.4.

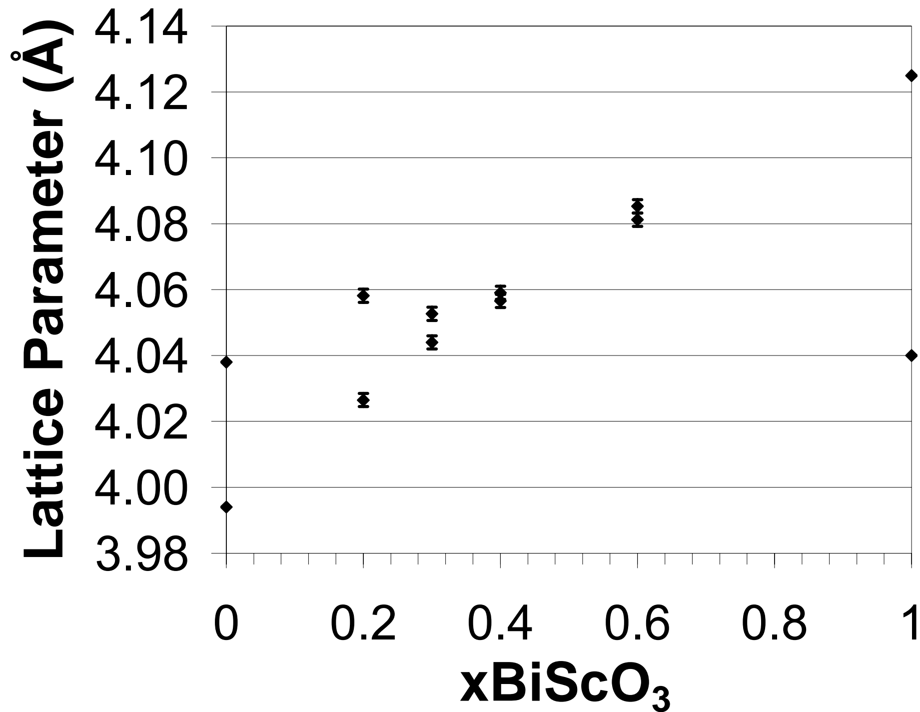

Fig. 4.13. Measured lattice parameter as a function of composition for films deposited at 700°C and 100 mTorr O_2/O_3. End member lattice parameters were taken from Maria [43] and Inaguma [47].

4-circle x-ray diffraction was performed on all compositions. The measured FWHM are plotted in Fig. 4.14. The small change in FWHM values for compositions between x=0.2-0.4 suggest that the films have similar structural quality. The larger FWHM value for x=0.6 indicates that the film is not of as high quality as other

compositions. It is possible that a combination of increasing lattice parameter (and hence larger misfit with the substrate) and inferior perovskite stability induces a larger mosaicity.

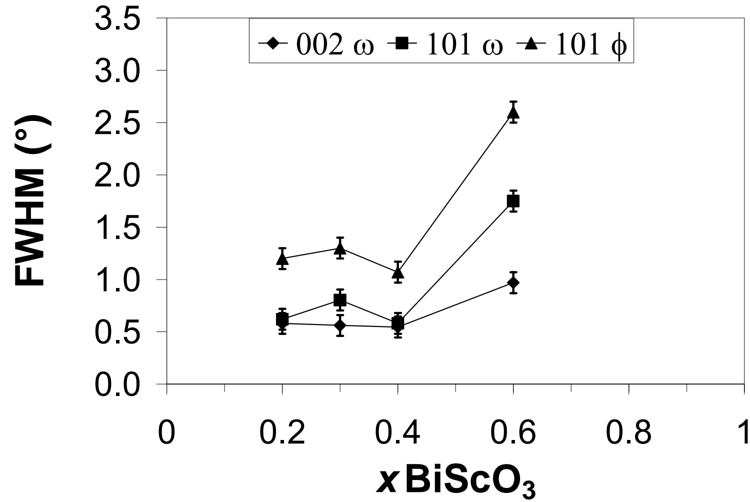

Fig. 4.14. FWHM for different composition of films deposited at 700°C and 100 mTorr O_2/O_3.

Scanning electron micrographs were used to examine surface morphology of the grown films as a function of composition. From Fig. 4.15, the surface morphology of the films does not change much in the composition range of x=0.2-0.4. At a composition of x=0.6 more pronounced surface features were evident.

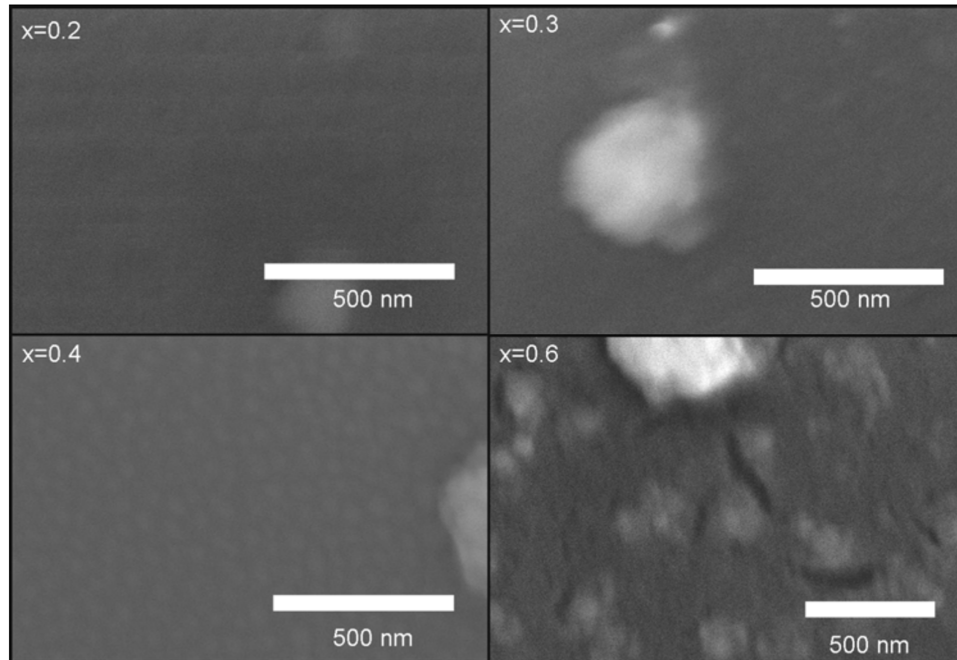

Fig. 4.15. Scanning electron micrographs of $xBiScO_3$-(1-x)$BaTiO_3$ on thin films deposited on SRO/LAO at 700°C and 100 mTorr O_2/O_3.

The unit cell volume of the *x*$BiScO_3$-(1-*x*)$BaTiO_3$ films is shown in Fig. 4.16. For ideal solid solutions, the unit cell volume scales linearly with composition, according to Vegard's law, (shown as the solid line in Fig. 4.16) [95]. As can be seen in the figure, the unit cell volume for *x*$BiScO_3$-(1-x)$BaTiO_3$ scales with composition, but does not follow ideal behavior. This type of behavior has been seen in other solid solutions with $BiScO_3$ [47]. It is also possible that part of the increase in unit cell volume is due to bombardment induced expansion, since unstrained bulk values were used for end members and film data for intermediate compositions.

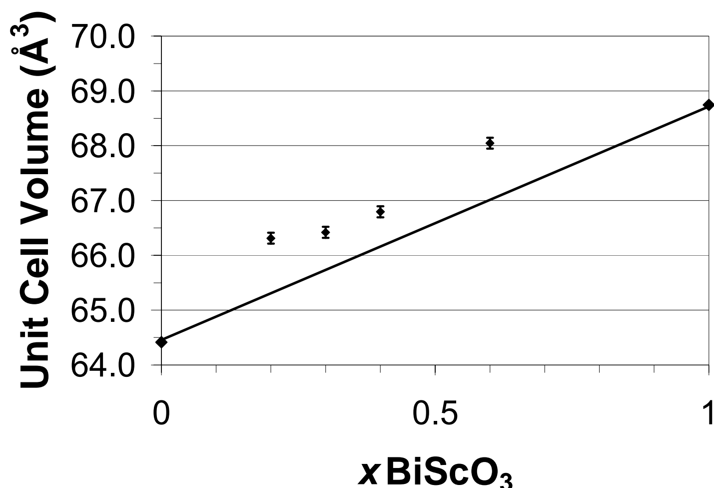

Fig. 4.16. Unit cell volume as a function of composition for xBiScO$_3$-(1-x)BaTiO$_3$ thin films. The solid line represents Vegard's Law. End member lattice parameters were taken from Maria [43] and Inaguma [47].

4.1.4 Thickness Dependence Study

As mentioned in chapter 2, the properties of the dielectric film can be a function of thickness due to size effects. In very thin epitaxial films, the film grows as a strained layer until some critical thickness [101]. Above that thickness the films begin to relax and assume lattice parameters closer to bulk values. This relaxation changes the stress levels within the films and so can have significant effects on the dielectric properties [31]. Using the Matthew-Blakeslee equation, the critical thickness for 0.4BiScO$_3$-0.6BaTiO$_3$ on relaxed SrRuO$_3$ can be calculated [74]. Using the lattice parameter from Fig. 4.13, a critical thickness of 10 nm is calculated, which is well below the thicknesses

used in this study. Consequently, any thickness dependence of the dielectric properties is presumed to arise from other sources.

In order to deposit films with different thickness under identical conditions, the length of the deposition was extended. The thickness of $0.4BiScO_3$-$0.6BaTiO_3$ films grown at 700°C and 100 mTorr O_2/O_3 as a function of deposition time is given in Fig. 4.17. The thickness of the films was measured using multiple profilometery scans and averaged to give a single value, while an electronic timer was used to measure the length of the deposition. The films show an average deposition rate of 4.7 nm/min (0.2 Å/pulse).

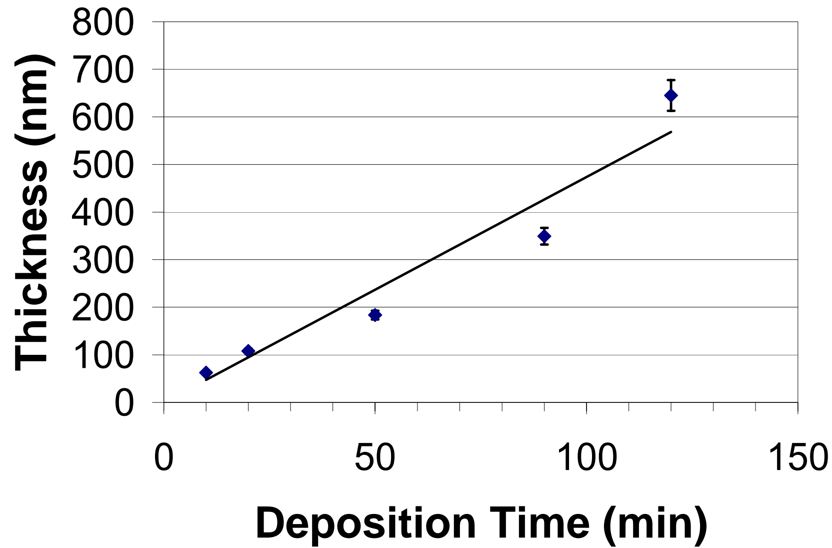

Fig. 4.17. Thickness as a function of deposition time for $0.4BiScO_3$-$0.6BaTiO_3$ thin films.

One potential concern with deposition at 700°C is bismuth volatility. A measure of the lattice parameters, or the unit cell volume can give an indication if significant bismuth losses occur at long deposition times. The lattice parameters of the $0.4BiScO_3$-$0.6BaTiO_3$ thin film as a function of thickness were measured and are plotted in Fig. 4.18. Previously for $PbTiO_3$, it was shown that as single crystals become lead deficient, the lattice parameter of the film decreases [45]. Similarly, with a volatile cation such as bismuth, one would expect the lattice parameters to drop as bismuth evolves from the films.

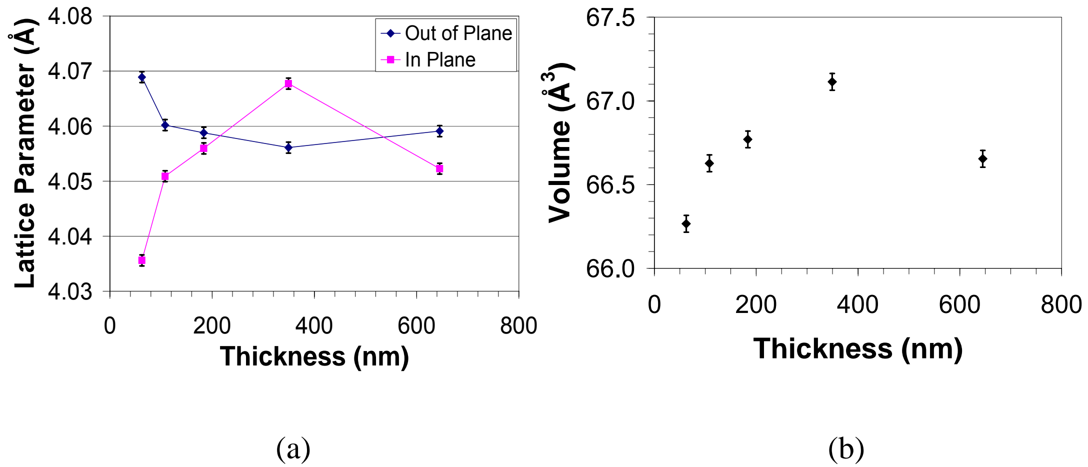

(a) (b)

Fig. 4.18. (a) Lattice parameters and (b) unit cell volume as a function of thickness for $0.4BiScO_3$-$0.6BaTiO_3$ thin films.

The lattice parameter of the films show the possibility of incomplete relaxation below 100 nm, however films with a thickness of 100 nm and above appear largely

relaxed. The amount of relaxation in the films was calculated, assuming the lattice parameters of the 650 nm film are fully relaxed, using equation 4.3:

$$r = 1 - \left(\frac{f_e}{f_s} \right) \qquad (4.3)$$

where r is the relaxation, f_e is the mismatch between the film at that thickness and the fully relaxed values and f_s is the mismatch between $SrRuO_3$ bottom electrode and the fully relaxed $BiScO_3$-$BaTiO_3$ lattice parameters. Using this equation the 60 nm thick $0.4BiScO_3$-$0.6BaTiO_3$ thin film is estimated to be ~85% relaxed. Looking at the unit cell volume as a function of thickness (Fig. 4.18b), it is clear that the unit cell volume of the films changes little with increasing thickness. The changes in the unit cell volume could stem from compositional inhomogenieties within the film. These compositional inhomegenieties must be on a small length scale because it was observed that there was only a 5% change in capacitance as a function of location on the samples. This would suggest that the composition underneath any particular electrode can be considered to be relatively constant.

Scanning electron micrograph images were taken as a function of film thickness and are shown in Fig. 4.19. It is apparent in the figure that as the film thickness increases, the number of defects observed in the film increases. When making electrical measurements it was observed that for thicker films there were less pinholes, allowing the use of larger electrodes. However, from Fig. 4.19, the thickest film (650 nm) apparently has the most pinholes. One cause of this is the longer time scales needed to deposit the thicker films yielding an increased number of particulates as deposition times increase.

These particulates would then self-shadow on the surface of the film causing the defective structure seen in Fig. 4.19.

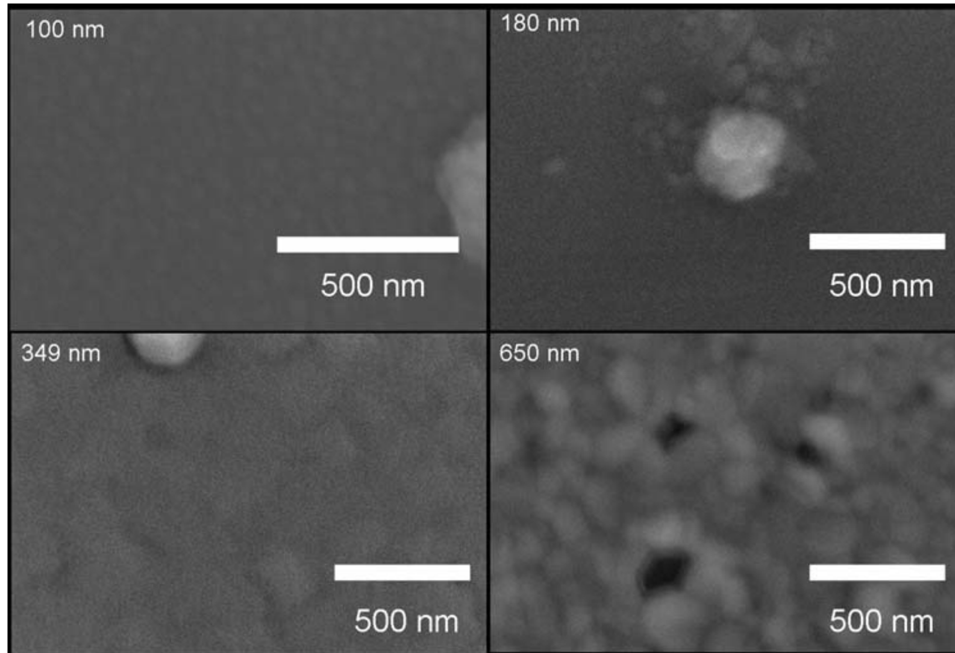

Fig. 4.19. Scanning electron micrographs as a function of thickness for $0.4BiScO_3$-$0.6BaTiO_3$/SRO/LAO thin films deposited at 700°C and 100 mTorr O_2/O_3.

4.2 Dielectric Properties of $xBiScO_3$-$(1-x)BaTiO_3$ Thin Films

Dielectric measurements were performed on films deposited at 700°C and 100 mTorr O_2/O_3. Photolithography was used to define the Pt top electrodes. An optical microscope image (Fig. 4.20) shows the range of contact sizes used in these experiments. In films below 150 nm thickness, pinholes caused shorting of larger electrodes. Films

were etched using a 10% buffered HF solution in order to expose the $SrRuO_3$ bottom electrode.

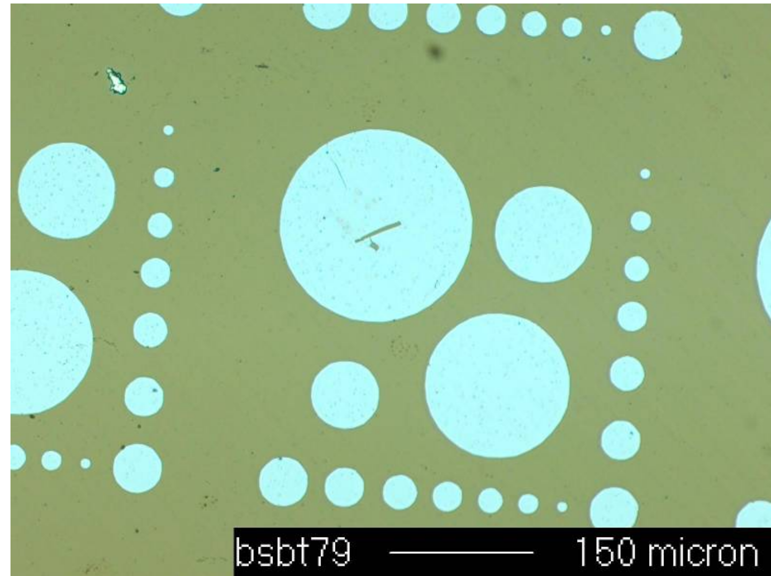

Fig. 4.20. Optical microscope image of top electrodes used in this thesis.

4.2.1 Dielectric Properties vs. Film Composition

The frequency response of permittivity was measured at room temperature. The permittivity of the films decreased approximately linearly with logarithm of frequency as shown in Fig. 4.21a. All films showed some measure of frequency dependence, with increasing dispersion seen at increasing $BiScO_3$ concentrations (Fig. 4.21b). It has been shown previously that the addition of Bi to other perovskites can increase frequency dispersion [55, 102, 103]. A $BiScO_3$-$BaTiO_3$ film that shows a small frequency dependence of the permittivity may be more like a normal ferroelectric, while substantial dispersion is characteristic of a relaxor ferroelectric. As mentioned in the literature

review, the addition of bismuth to many perovskite structures leads to a dielectric relaxation [53, 55]. Thus, the frequency and temperature dependence of these films was investigated.

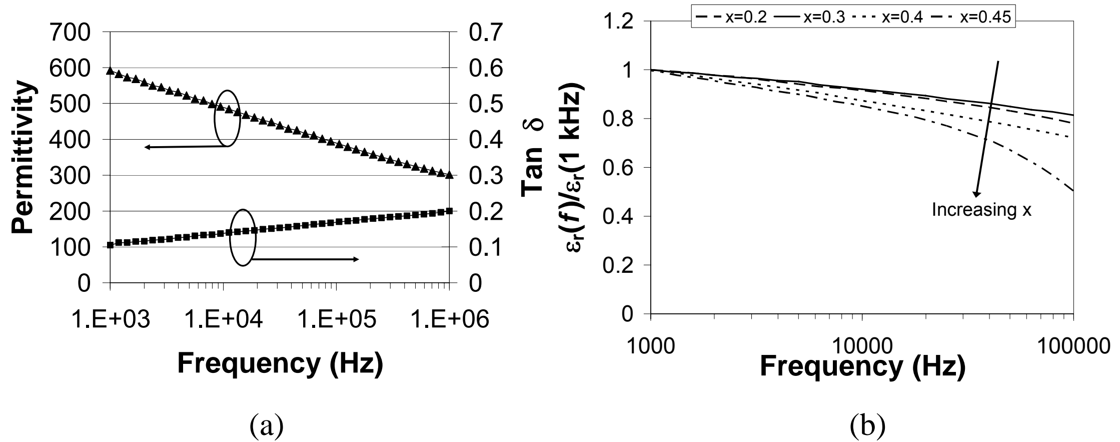

Fig. 4.21. (a) Permittivity vs. frequency for a $0.4BiScO_3$-$0.6BaTiO_3$ /SRO/LAO thin film and (b) $\varepsilon_r(f)/\varepsilon_r(1\ \text{kHz})$ vs. frequency showing increasing frequency dependence with increasing $BiScO_3$ concentration.

Permittivity was measured as a function of temperature and frequency for a series of compositions in epitaxial films. Some data above room temperature were taken on a heated probe station. For other measurements, samples were wirebonded to a chip package and cooled in a nitrogen cooled Delta Design oven with a temperature range of -180°C to 200°C. The permittivities were measured with frequencies between 20 Hz and 1 MHz. For a composition of x=0.4, the permittivity of the films increases from ~450 at

room temperature until a peak of 800 at ~200°C (see Fig. 4.22a). The broad permittivity maximum of ~800 occurs over a 100°C temperature range. There is a strong frequency dependence of the permittivity *below* T_{Max} which collapses above T_{Max}. This suggests that the dispersion is due primarily to relaxor ferroelectricity rather than space charge contribution since conductivity (and dispersion) would be expected to rise monotonically as temperature is increased. Data for other compositions are shown in Figures 4.23 and 4.24.

The temperature of the permittivity maximum was shown to increase with increasing $BiScO_3$ content (Fig. 4.22b). This not uncommon for the case where a low Curie point material is in solid solution with a high Curie point material. This suggests that $BiScO_3$ acts to stabilize the ferroelectric phase [104].

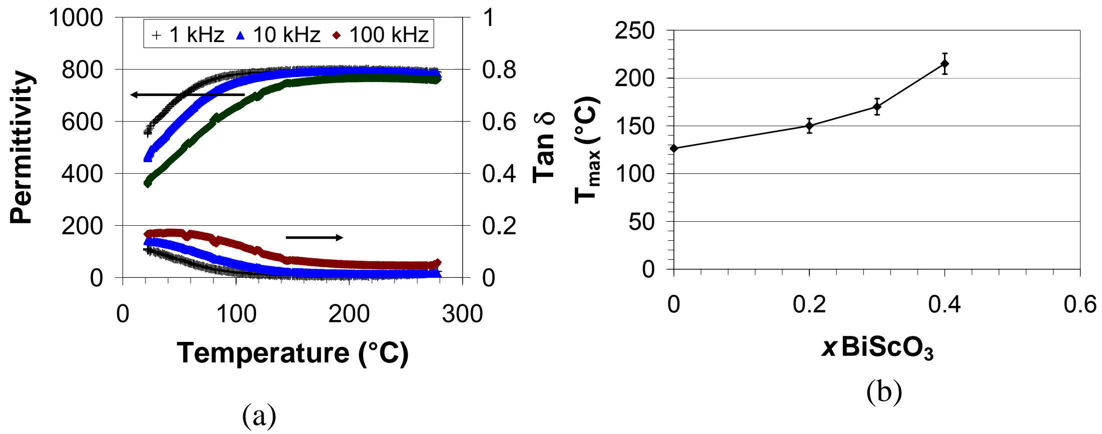

Fig. 4.22. (a) Permittivity vs. temperature for a $0.4BiScO_3$-$0.6BaTiO_3$/SRO/LAO thin film at various frequencies and (b) T_{Max} $xBiScO_3$-$(1-x)BaTiO_3$/SRO/LAO thin films at 10 kHz.

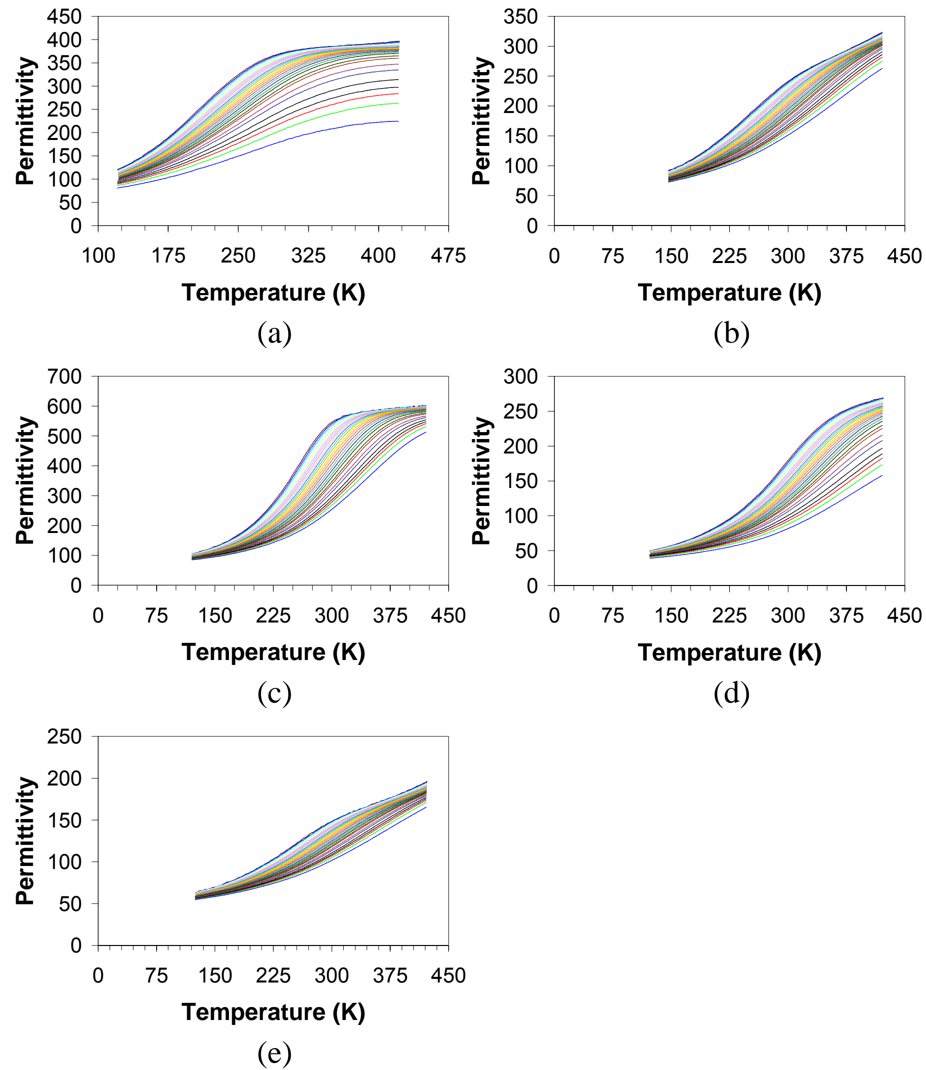

Fig. 4.23. Permittivity as a function of temperature and at different frequencies for xBiScO$_3$-(1-x)BaTiO$_3$/SRO/LAO thin films. (a) x=0.2, (b) x=0.35, (c) x=0.4, (d) x=0.45, and (e) x=0.6 for frequencies ranging from 100 Hz to 1 MHz.

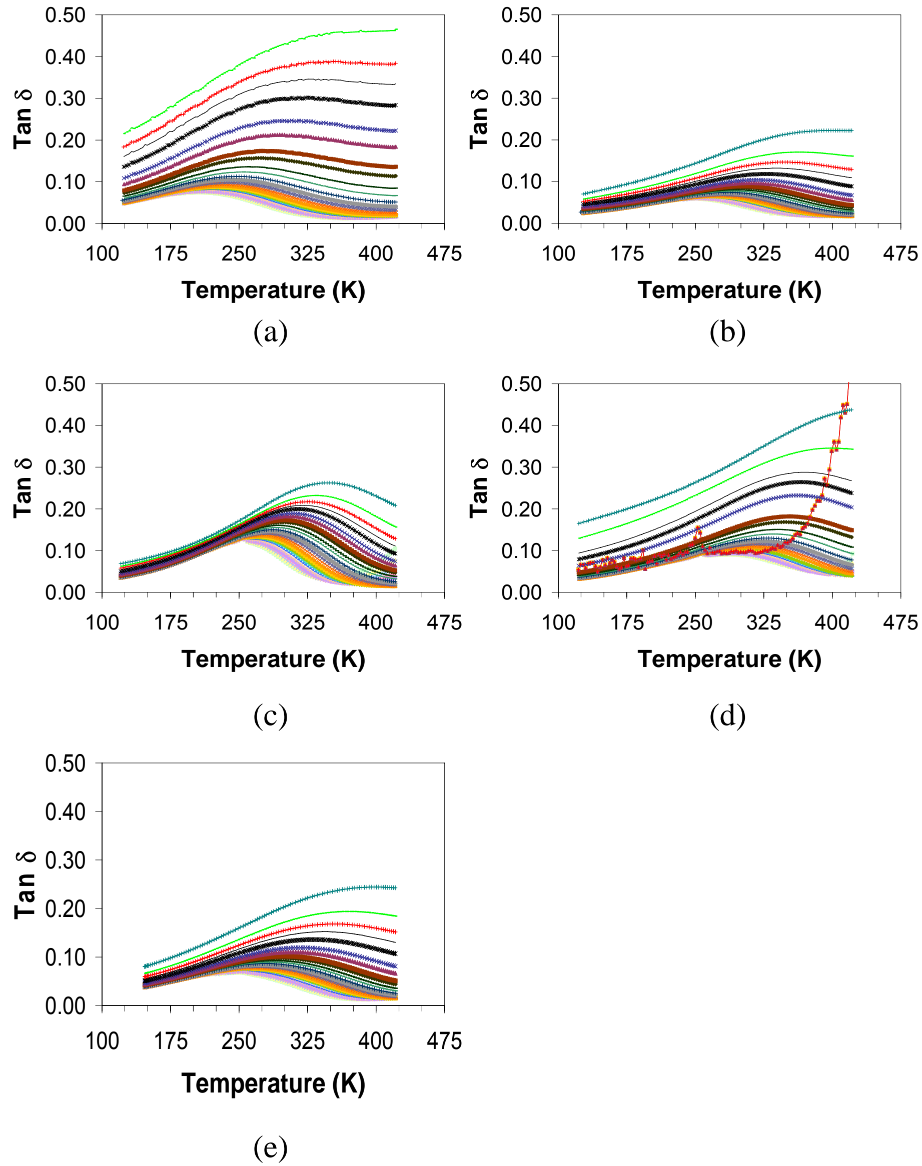

Fig. 4.24. Loss tangent as a function of temperature measured at different frequencies for xBiScO$_3$-(1-x)BaTiO$_3$/SRO/LAO thin films. (a) x=0.2, (b) x=0.35, (c) x=0.4, (d) x=0.45, and (e) x=0.6 for frequencies ranging from 100 Hz to 1 MHz.

Because the dielectric loss of some of the compositions was quite high, over at least part of the temperature range, the resistivity of the films were measured using through the thickness of the films. A HP 4140B pA meter/DC voltage source was used to measure the current across the capacitors as a function of applied voltage. A DC bias was applied to the sample and held for ~10 s and the leakage current was measured at electric fields and temperatures. Through plotting the current density as a function of electric field, the resistivity of the capacitor is calculated using the slope of the linear region. Fig. 4.25 shows a plot of the resistivity of a $0.4BiScO_3$-$0.6BaTiO_3$/SRO/LAO thin film as a function of temperature. As is seen in the graph, the resistivity for the films ranges between 10^{13}-10^{15} Ω-cm. This suggests that the films are highly insulating and the high losses associated with the films stems from a dielectric relaxation rather than a conduction process. Using an Arrhenius relationship, the activation energy for conduction is 0.46 ± 0.08 eV which is low compared to other ferroelectric systems [105, 106] and comparable to other Bi_2O_3 systems [107, 108].

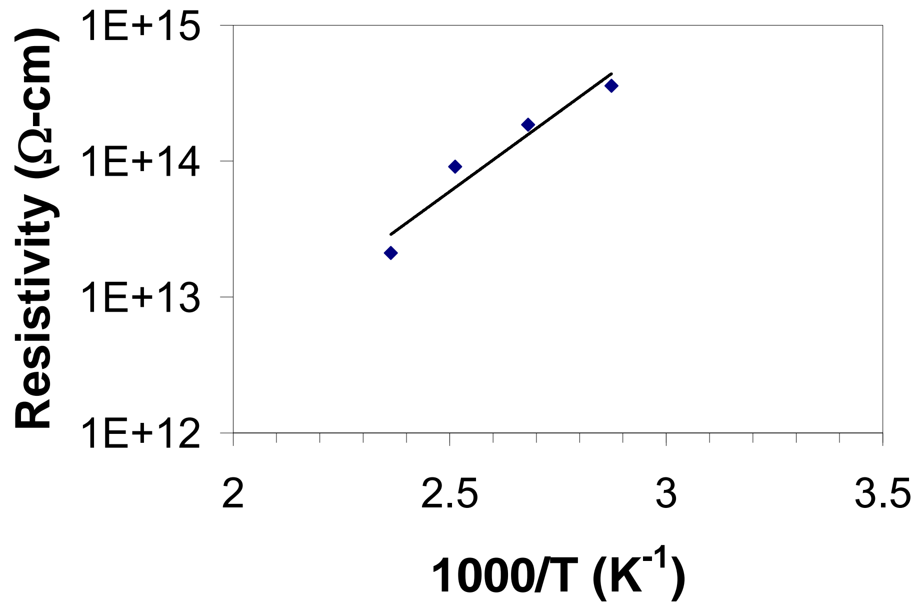

Fig. 4.25 Resistivity of a $0.4BiScO_3$-$0.6BaTiO_3$/SRO/LAO thin film as a function of 1/T.

The morphotropic phase boundary in materials can be seen through an analysis of electrical data as a function of composition. As mentioned in chapter 2, at the morphotropic phase boundary an increase in permittivity, electromechanical coupling factor, and piezoelectric coefficients is observed. Through measuring permittivity as a function of composition, the location of a morphotropic phase boundary can be determined.

The permittivity of the $BiScO_3$-$BaTiO_3$ films as a function of composition was measured at varying temperatures and is plotted in Fig. 4.26. The permittivity initially drops with $BiScO_3$ additions, possibly due to the low Curie point of the $BaTiO_3$ end

member and the *a*-domain character of the tetragonal films at room temperature. In most perovskites, the permittivity is anisotropic, and substantially larger transverse to the polar axis. The permittivity then increases with increasing $BiScO_3$ content until the morphotropic phase boundary is reached at ~x=0.4. Above a composition of x=0.4, the permittivity decreases. The agreement between the phase boundary composition estimated from the tolerance factor and the experimentally determined boundary is quite good. Unfortunately, the very broad permittivity vs. temperature curve makes it difficult to ascertain whether the MPB is curved in the $BiScO_3$-$BaTiO_3$ solid solution.

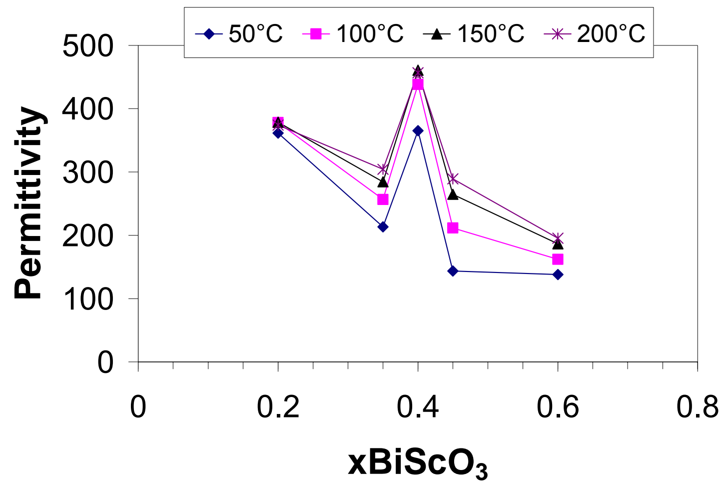

Fig. 4.26. Permittivity and loss tangent at 10 kHz as a function of composition for $x$$BiScO_3$-(1-$x$)$BaTiO_3$ thin films with thicknesses around 100 nm at varying temperatures.

Due to high losses at room temperature, the permittivity was investigated as a function of temperature across the MPB. In Fig. 4.26, the peak in permittivity at the

MPB exists to elevated temperatures. This type of behavior is characteristic of MPB compositions, as shown in Fig. 4.27 for the $PbZr_{1-x}Ti_xO_3$ solid solution [109]. The high polarizability of the MPB materials yields high Curie constants, and large permittivity values both above and below the phase transition temperature. There is also a possibility that some of the permittivity enhancement observed for $0.4BiScO_3$-$0.6BaTiO_3$ is due to the fact that the film deposition parameters were optimized for that composition. This is believed to be a comparatively minor effect, however, since the end members have previously been shown to have good properties at very similar deposition parameters.

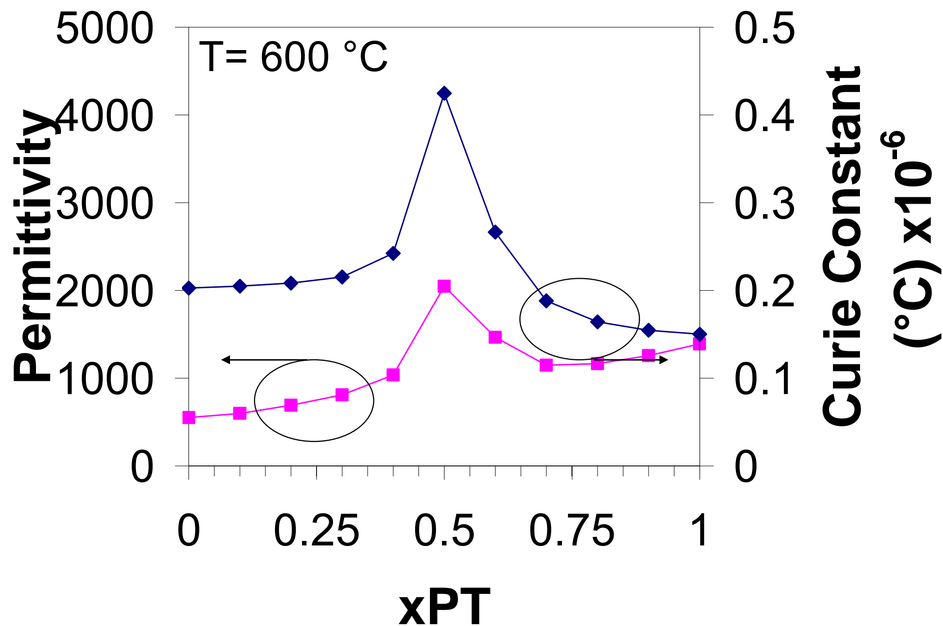

Fig. 4.27. Phenomenologically derived values for permittivity and the Curie constant of $Pb(Zr_{1-x}Ti_x)O_3$ as a function of composition at a temperature of 600°C. Equations taken from Haun [109].

In order to understand the relaxation that the films undergo, the permittivity and loss tangents measured at low temperatures were examined further. Due to the large flat region in permittivity, the peaks in the loss data were used to assess the relaxation. An asymmetric power function was fitted to data points near the peak in the tan δ data. The T_m obtained from the fit was used in the Vogel-Fulcher relationship in order to obtain the fitted parameters activation energy, E_a, characteristic freezing temperature T_f, and the pre-exponential factor, τ_o. A plot of the natural log of the relaxation time ($1/2\pi f$) as a function T_m is shown in Fig. 4.28. The relaxation of the films was found to follow a Vogel-Fulcher relationship $\left(\tau = \tau_o \exp\left(\frac{Ea}{k_b\left(T_m - T_f\right)}\right)\right)$. The Vogel-Fulcher analysis was performed on films with an approximate thickness of 100 nm and the fitted parameters E_a, T_f, and τ_o are plotted in Fig. 4.29. It was found that the activation energy increases with higher $BiScO_3$ contents. Comparable behavior has been observed previously in $PbMg_{1/3}Nb_{2/3}O_3 - PbTiO_3$ films [110].

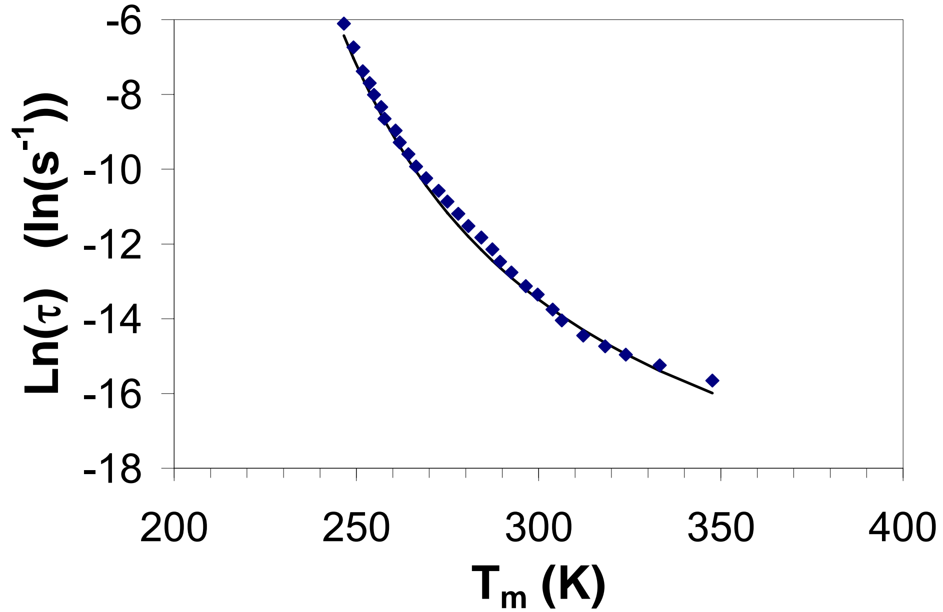

Fig. 4.28. Plot of natural log of the relaxation time as a function of T_m for a $0.4BiScO_3$-$0.6BaTiO_3$/SRO/LAO thin film. Solid line is the Vogel-Fulcher fit to the data.

Additionally, the freezing temperature T_f is shown to initially increase with increasing $BiScO_3$ composition. It was not clear why T_f decreased again for x=0.6. Lastly, in Fig. 4.29d, the measured T_{Max} in the loss data for each composition at 10 kHz is reported. These data follow the same trend seen for the T_f of the system.

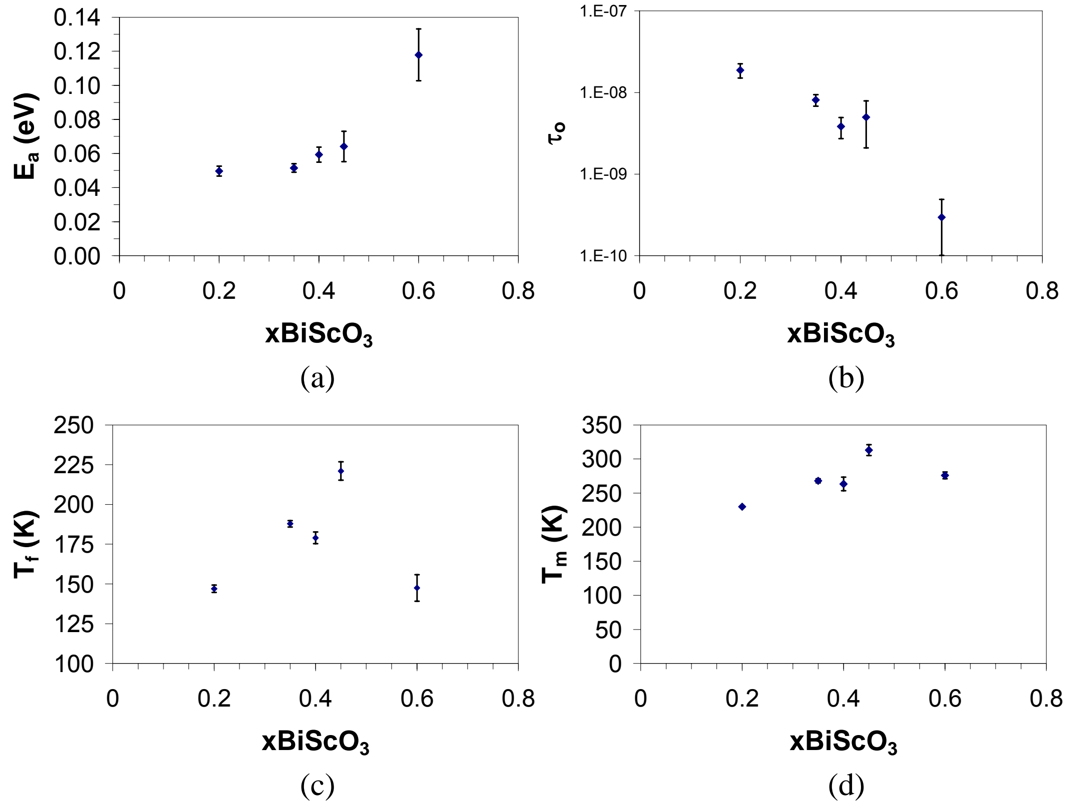

Fig. 4.29. Vogel-Fulcher fitting parameters as a function of composition (a) activation energy, E_a, (b) relaxation time τ_o, (c) characteristic temperature, T_f, and (d) the T_m in the loss data at 10 kHz.

It is also observed that τ_o decreases with increasing $BiScO_3$ composition (Fig. 4.29a). The τ_o shown for x = 0.6 is characteristic of many other relaxor ferroelectrics as seen in Table 4.1. The τ_o values for the $BaTiO_3$ – rich compositions denote a characteristic relaxation time that is substantially longer than is typical for bulk relaxor ferroelectrics, where the attempt frequency is typically on the order of 10^{-12} s. Similar

values have been previously reported for $PbMg_{1/3}Nb_{2/3}O_3$-$PbTiO_3$ films in compositions where a stable ferroelectric phase is observed at room temperature, as shown in Fig. 4.30. Likewise, in Bi:$SrTiO_3$, the reported relaxation times are on the order of 10^{-10} s, which are also substantially longer than most relaxor ferroelectrics.

Table 4.1 τ_o values for several different compositions of perovskites

Composition	τ_o	Error	Ref.
$0.2BiScO_3$-$0.8BaTiO_3$*	1.88×10^{-8}	3.69×10^{-9}	—
$0.35BiScO_3$-$0.65BaTiO_3$*	8.12×10^{-9}	1.31×10^{-9}	—
$0.4BiScO_3$-$0.6BaTiO_3$*	3.83×10^{-9}	1.11×10^{-9}	—
$0.45BiScO_3$-$0.55BaTiO_3$*	4.99×10^{-9}	2.90×10^{-9}	—
$0.6BiScO_3$-$0.4BaTiO_3$*	2.96×10^{-10}	1.95×10^{-10}	—
PMN*	1.20×10^{-11}		[110]
0.9PMN-0.1PT*	2.30×10^{-9}		[110]
0.8PMN-0.2PT*	6.80×10^{-9}		[110]
0.9PMN-0.1PT	9.71×10^{-13}		[111]
PZN	2.88×10^{-13}		[112]
$(Pb_{0.92}La_{0.08})(Zr_{0.65}Ti_{0.35})O_3$	5.81×10^{-14}		[113]
$Sr_{0.96}Bi_{0.04}TiO_3$	2.21×10^{-9}		[53]
$Sr_{0.9}Bi_{0.1}TiO_3$	3.73×10^{-10}		[53]
$Sr_{0.8}Bi_{0.2}TiO_3$	3.25×10^{-9}		[53]
$Ba(Ti_{0.7}Zr_{0.3})O_3$	6.49×10^{-11}		[114]
$Ba(Ti_{0.9}Ce_{0.1})O_3$	6.89×10^{-12}		[115]
$Ba(Ti_{0.8}Ce_{0.2})O_3$	9.43×10^{-9}		[115]

* Denotes thin film data

There are several possible mechanisms for the films that might account for these long time constants: 1) some degree of order-disorder character to the phase transition. Many of the faster time constants are associated with displacive phase transitions. $BaTiO_3$ itself has some degree of order-disorder character associated with its phase transition; this might be exacerbated by Bi^{3+} doping [116]. 2) Defects associated with the

thin film preparation methods. The PMN-PT time constants reported by Donnelly for thin films are substantially slower than those observed for bulk materials of the same composition [110]. It is possible that similar phenomena are operating here. 3) The possibility that the dipolar units undergoing the relaxation are larger (and hence slower) than would be normal for the micropolar regions in PMN-based relaxors.

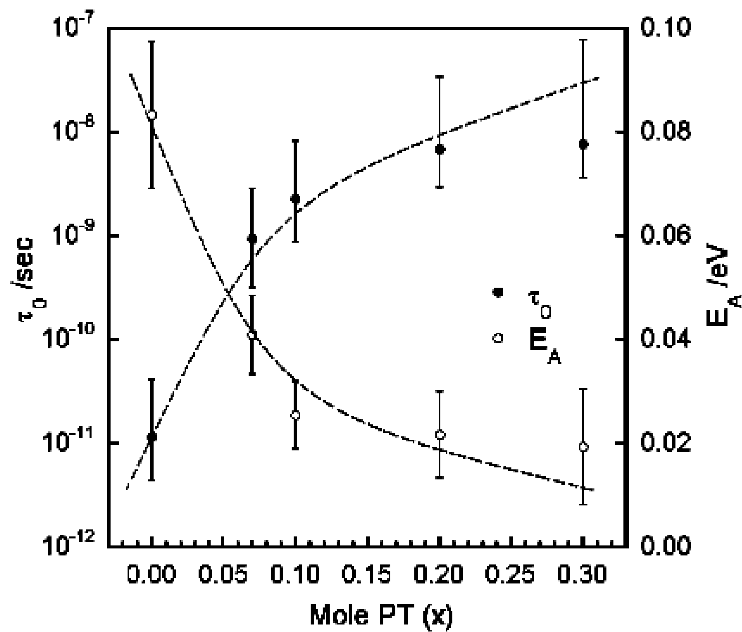

Fig. 4.30. Relaxation time for various compositions within the PMN-PT system [110].

4.2.2 Dielectric Properties vs. Film Thickness

It is also interesting to consider how the permittivity scales with thickness. In thin films, the permittivity often decreases due to interfacial layers [12], grain size effects

[117, 118], stress effects [86, 119, 120], or depolarization effects [120-122]. The fact that the Bi^{3+} cation has a lone pair of s-shell electrons [52, 123] should increase the polarizability of the films, which may stabilize permittivity to smaller thicknesses. In Fig. 4.31 we can see that as the thickness of $0.4BiScO_3$-$0.6BaTiO_3$ film decreases from ~600 nm to ~50 nm, the permittivity decreases by a factor of 2. The thickness dependence of permittivity exhibited by these films is comparable to the thickness dependence reported for other films [35, 36].

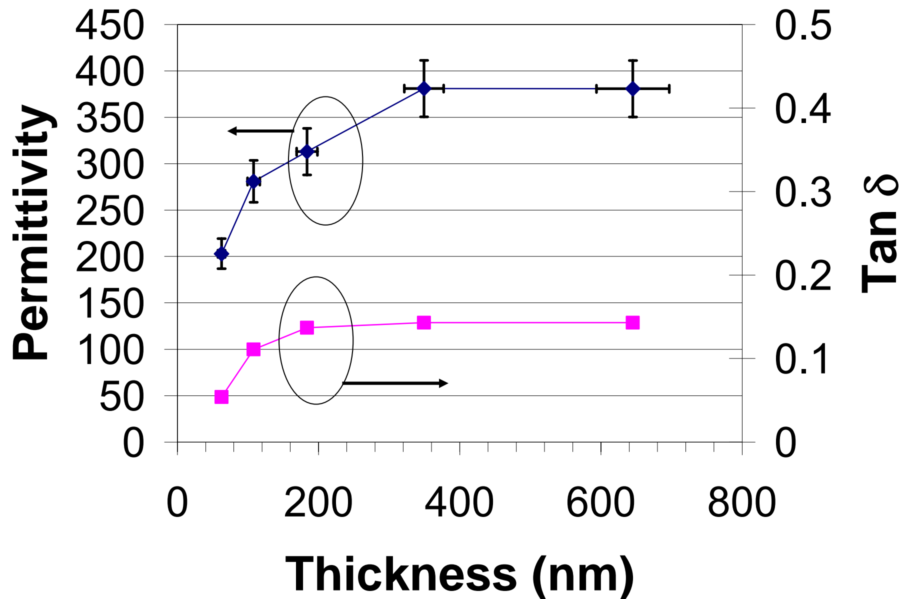

Fig. 4.31. Permittivity and loss tangent as a function of thickness for $0.4BiScO_3$-$0.6BaTiO_3$ thin films.

The broad permittivity maximum shown in Fig. 4.22a indicates the possibility of an interfacial layer acting as a Curie point flattener. In addition, grain size effects have

been known to decrease permittivity peaks as well [117, 118]. To determine if a parasitic interfacial layer is lowering the capacitance of the films, the inverse capacitance (standardized for the area of electrode) was plotted as a function of thickness for various temperatures and is shown in Fig 4.32. Using the series capacitance model given in equation 2.7, the interfacial capacitance can be estimated from the *y*-intercept in the graph. From this model an interfacial capacitance of 49.3 ± 6.0 fF/μm^2 was calculated. This is less than what is reported for other $BaTiO_3$-based solid solutions [12]. The interfacial capacitance for the films exhibits no temperature dependence within the experimental error. This suggests that the interfacial capacitance does not stem from a substantial compositional gradient within the film. That is, if the interfacial capacitance were due to initial nucleation of a $BaTiO_3$ – rich phase (perhaps due to its better lattice match to the substrate or to its improved perovskite phase stability), then the interfacial layer might be expected to show a finite temperature dependence, particularly if the layer were comparatively thick. The origin of the interfacial capacitance is unknown.

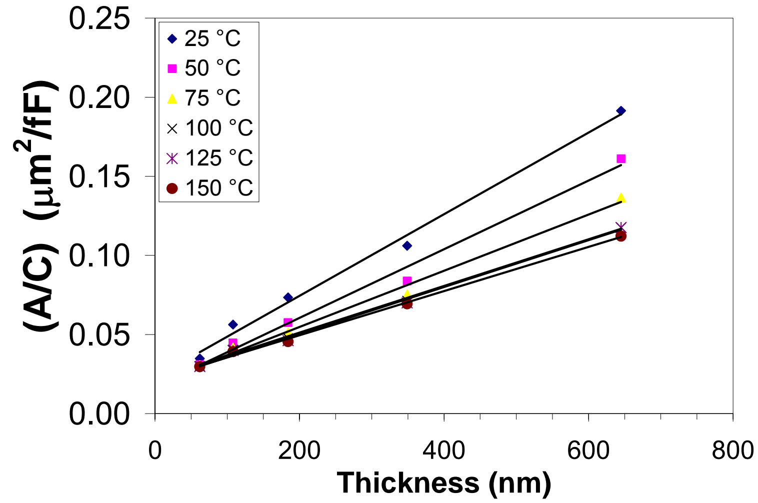

Fig. 4.32. Inverse of the capacitance density as a function of thickness for a $0.4BiScO_3$-$0.6BaTiO_3$ thin film.

The dc field dependence of the permittivity was examined to look for evidence of ferroelectricity. To measure this, a dc bias was applied to the films and the small signal permittivity at 10 kHz was recorded. The films showed considerable bias dependence as seen in Fig. 4.33 for a $0.4BiScO_3$-$0.6BaTiO_3$ thin film. The small but finite hysteresis seen during these measurements suggests that the films are ferroelectric.

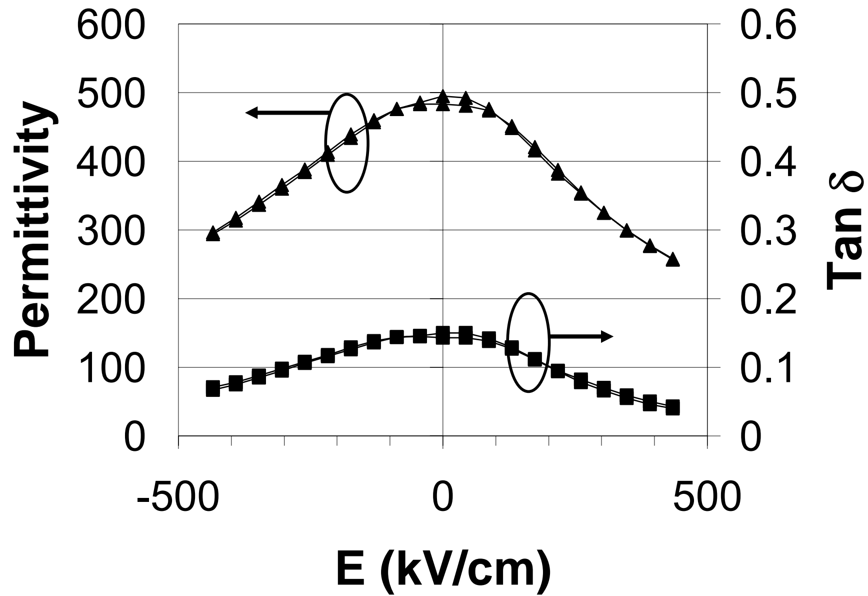

Fig. 4.33. Permittivity and loss tangent as a function of DC bias field for a $0.4BiScO_3$-$0.6BaTiO_3$/SRO/LAO thin film.

4.3 Dielectric Hysteresis of $xBiScO_3$-$(1\text{-}x)BaTiO_3$ Thin Films

Fig. 4.34 shows a polarization hysteresis loop for a $0.4BiScO_3$-$0.6BaTiO_3$ film grown on (100) $SrRuO_3/LaAlO_3$. The behavior of the film was representative of all epitaxial films. The films show a coercive field of ~200 kV/cm with a remanent polarization near 9 $\mu C/cm^2$. Polycrystalline films deposited on Pt-Si showed similar behavior, with higher loss values. The slim loop characteristics shown in Fig. 4.34 most likely stem from the relaxor character of the film and the proximity to T_{Max}. Films that did not exhibit space charge contributions had breakdown strengths that exceeded 2MV/cm.

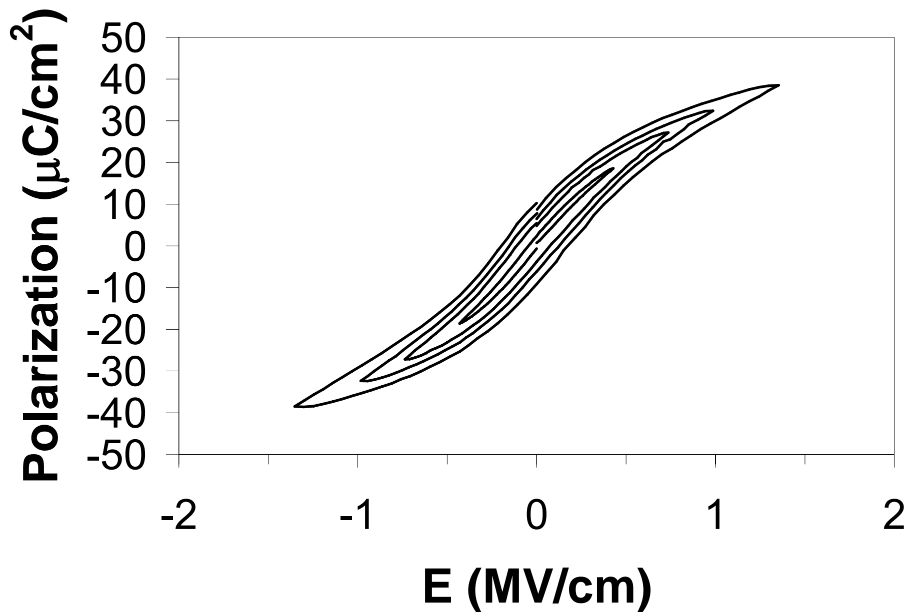

Fig. 4.34. Polarization hysteresis loop for a $0.4BiScO_3$-$0.6BaTiO_3$ thin film on (100) $SrRuO_3/LaAlO_3$.

The low remanent polarization value is disappointing, as it is likely to reduce the achievable piezoelectric coefficient in the material, thus rendering it less useful as a lead-free piezoelectric. Thus, it would be useful to develop a means of increasing the remanent polarization.

In order to determine if a remanent polarization develops in the films in a different temperature range, the polarization hysteresis curves were measured as a function of temperature up to a field level of > 1MV/cm. It is shown in Fig. 4.35a that as the temperature is lowered; a larger remanent polarization develops in the films. In addition, the coercive field required to switch the material scales with decreasing

temperature (shown in Fig. 4.35b). Both of these are indicative of a ferroelectric phase. While the remanent polarization increases with decreasing temperature, the coercive field remains relatively constant until a temperature of ~ -50°C (223 K) before it begins to increase. The freezing temperature of a material is dependent on the electric field and it is expected that one would obtain different values for low and high electric field measurements. The decrease in polarization at very low temperatures can be attributed to hysteresis loops that do not achieve full saturation for the field values used.

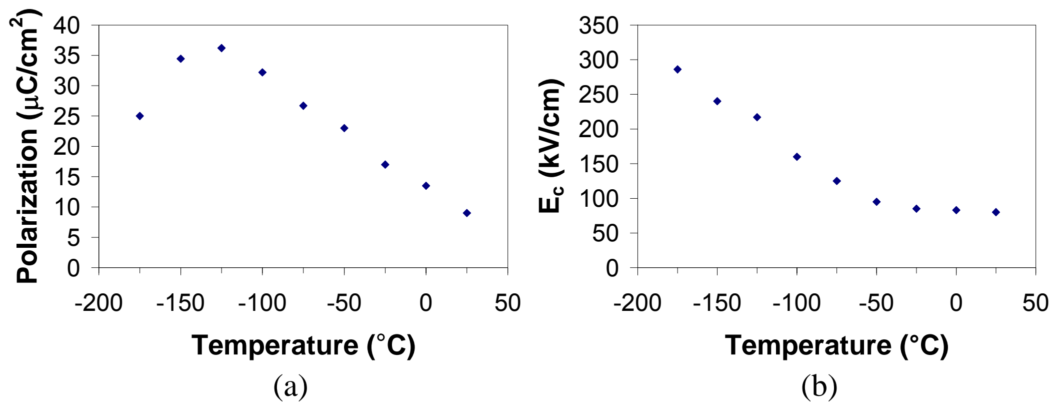

Fig. 4.35. (a) Remanent polarization and (b) coercive field as a function of temperature for a $0.4BiScO_3$-$0.6BaTiO_3$/SRO/LAO thin film.

The hysteresis loop and its minor loops are measured as in Fig. 4.36. Under a high enough electric field, all hysteresis loops show some ferroelectric character. Lastly in Fig. 4.37 the hysteresis behavior across the composition range is shown. The nature of the hysteresis loops changes as a function of composition, possibly stemming from the

changing nature of the ferroelectric phase. At -175°C the electric field required to induce the ferroelectric phase increases with increasing $BiScO_3$ composition. A bad electrical contact is probably causing the misshapen loop seen in the x=0.6 sample.

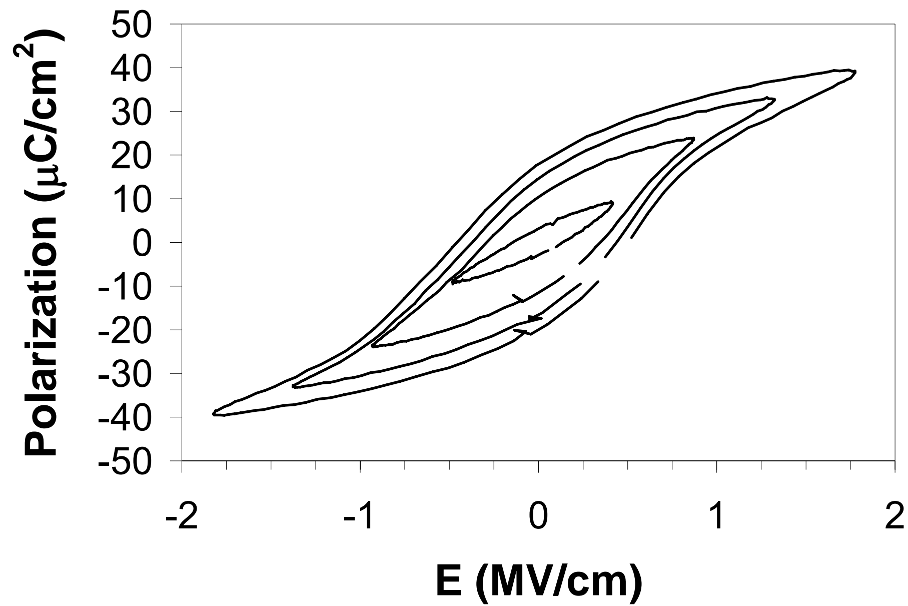

Fig. 4.36. Hysteresis loops for $0.2BiScO_3$-$0.8BaTiO_3$/SRO/LAO measured at -175°C under different electric fields.

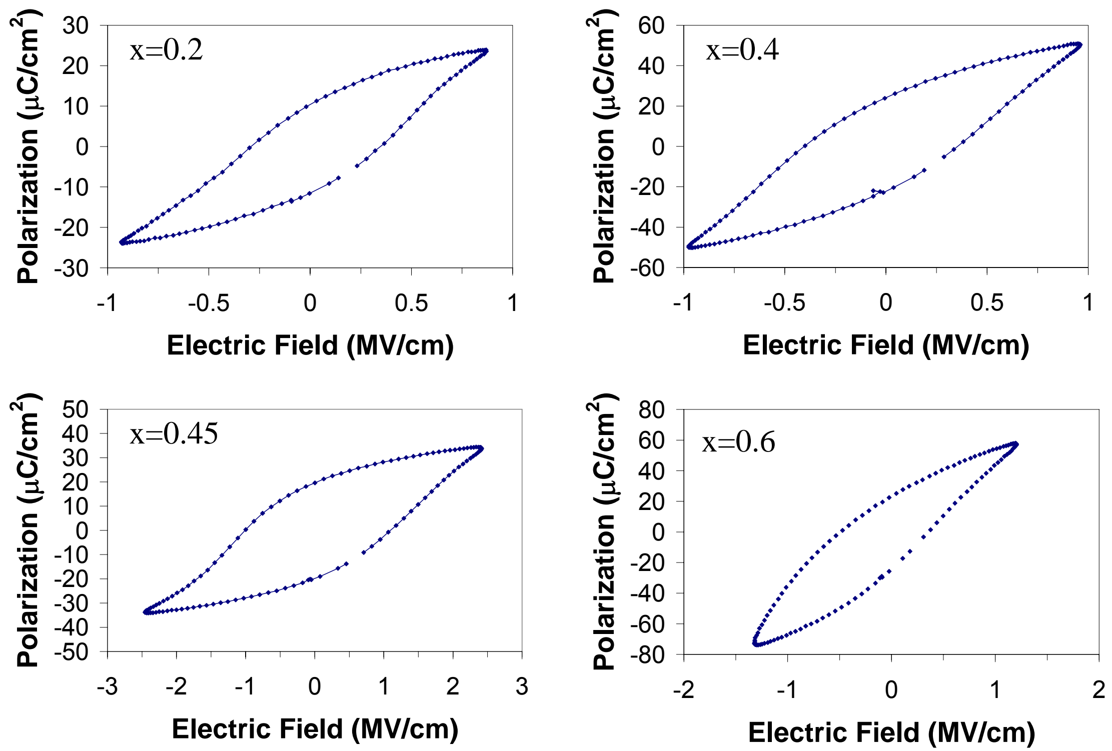

Fig. 4.37. Hysteresis loops for $xBiScO_3$-$(1\text{-}x)BaTiO_3$/SRO/LAO measured at -175 °C.

5.0 Conclusions and Recommendations for Future Work

5.1 Summary and Conclusions

Using a tolerance factor approach, it was predicted that $x BiScO_3$ – $(1-x)BaTiO_3$ will have a morphotropic phase boundary that should enhance both the polarizability and permittivity, relative to the $BiScO_3$ end-member, near a composition of $x = 0.4$. To verify this prediction, pulsed laser deposition was used to grow $x BiScO_3$-$(1-x)BaTiO_3$ thin films on (100) $SrRuO_3/LaAlO_3$ and Pt-coated Si substrates. Optimized growth conditions were 700°C and 100 mTorr O_2/O_3 and a target to substrate distance of 8 cm. The perovskite structure was found to be stable for compositions of x=0.2-0.6 in epitaxial films, with a reduced stability range in polycrystalline films.

The temperature where the maximum permittivity occurs rises as $BiScO_3$ is added to $BaTiO_3$, and increasingly relaxor-like behavior is observed with increasing $BiScO_3$ content. Room temperature permittivity values ranged from 200 to 400, with loss tangents of ~0.1 at 10 kHz. The high resistivity of the films indicates that the majority of the dielectric loss in this system stems from a dielectric relaxation rather than a conduction process. The experimental morphotropic phase boundary was found near x=0.4. This composition showed a broad permittivity maximum of ~800 between 150 and 275°C. Films with $x = 0.4$ show a coercive field of about 100 kV/cm with a modest room temperature remanent polarization less than 10 $\mu C/cm^2$. The films exhibit a dielectric tunability of greater than 25% at fields of ~500 kV/cm. The relaxation in the

films was characterized using the Vogel-Fulcher analysis with the E_a, τ_o and T_f changing as a function of composition.

The high, temperature-stable permittivity makes these films attractive for use in capacitor and piezoelectric applications. However, if the degree of relaxor character could be reduced (with commensurate reductions in the dielectric loss and increased squareness in the P-E loop) the range of applications could be greatly expanded. In particular, this system could be a potential replacement for lead based thin films in piezoelectric applications. However, the high permittivity at and low loss at elevated temperatures makes this an interesting material for high temperature lead free capacitor applications.

5.2 Future Work

5.2.1 Increasing the Remanent Polarization

Since films are clamped to the substrate, using strain engineering and producing a compressive in-plane strains should also push the polarization out of the plane of the film, as described in Tuttle's transformation stress model [124]. The result should be an increase in the remanent polarization. A high thermal expansion coefficient substrate such MgO (α = 13 ppm/°C [125]), should thus increase the out-of-plane polarization. For example, Brennecka et al. showed that the remanent polarization increased for $PbZr_{0.4}Ti_{0.6}O_3$ when deposited on higher thermal expansion coefficient substrates (Fig. 5.1) [125]. The increase in polarization is associated with an increase in the *c*-domain orientation of the film.

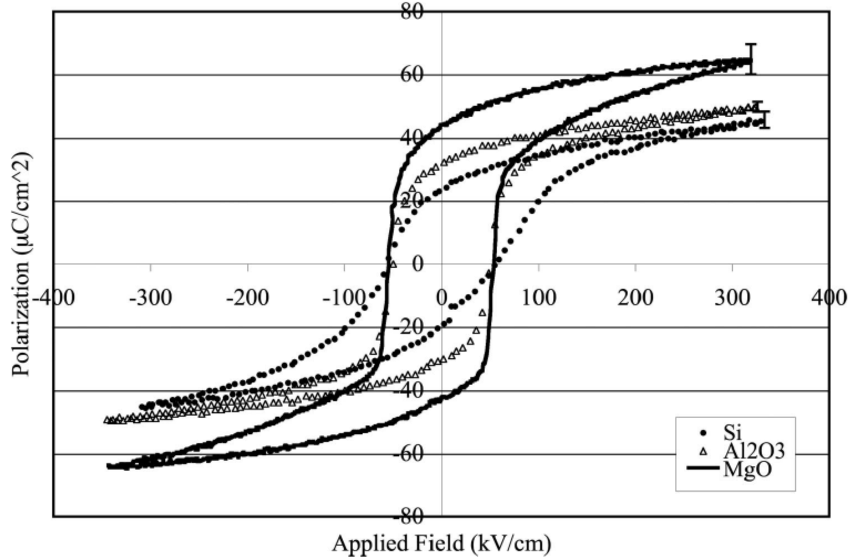

Fig. 5.1 Polarization hysteresis loops for $PbZr_{0.4}Ti_{0.6}O_3$ on MgO (α_T= 13 ppm/°C), Al_2O_3 (α_T =7.4 ppm/°C) and Si (α_T= 4 ppm/°C)three different substrates showing the effect of stress on remanent polarization [125].

Since this is the first synthesis of $BiScO_3$-$BaTiO_3$ to date, it would be useful to develop bulk powders over the same composition range in order to precisely determine lattice parameters, Curie point, permittivity, and remanent polarization. Doing so would allow composition effects to be separated unambiguously from the clamping effects imposed by the substrate on the film. Additionally, studying the crystallography of the bulk sample will allow a precise measurement of the $BiScO_3$-$BaTiO_3$ phase diagram, including the shape of the morphotropic phase boundary.

Impedance measurements in bulk samples would also yield information on the nature of the high losses at room temperature, i.e. whether or not is intrinsic to the

dielectric relaxation or some conduction process. Additionally, the nature of the relaxation process and the large losses in this system is still unknown and warrants investigation. The high permittivity and low loss at high temperatures would be attractive for certain applications. Through doping of $BiScO_3$-$BaTiO_3$ with an ion known to lower T_m, such as La^{3+}, would open up applications that require a lead free temperature stable capacitor at room temperature.

Lastly, measurements of film compositions as a function of temperature should be made in order to determine with the temperature at which significant bismuth loss occurs during growth of the films. This could be particularly useful in optimizing the target and film compositions.

5.2.2 Alternative Bismuth Perovskites

Alternatively, producing thin films of other bismuth-based perovskites might be preferable to doping $BiScO_3$-$BaTiO_3$. $BiAlO_3$ is predicted to be ferroelectric from first principle calculations. However, $BiAlO_3$ has poor perovskite stability, [63] and has only been synthesized under high pressure [64, 126]. Moreover, experimental measurements of the lattice parameter showed a doubling of the unit cell which was not predicted in the theoretical calculations[62].

Attempts at using epitaxy thin films to stabilize the $BiAlO_3$ perovskite structure have proven difficult [71]. Initial attempts by the author to stabilize $BiAlO_3$ using 10 mol% $PbTiO_3$ were not successful (Fig. 5.2). Using a stable Al^{3+} perovskite may stabilize the $BiAlO_3$ phase. Thus, an investigation of the $LaAlO_3$-$BiAlO_3$ phase diagram is suggested. La^{3+} being slightly larger and more electropositive than Bi^{3+} would act as a

stabilizing agent for $BiAlO_3$. While La^{3+} is known to lower the Curie point and slim the hysteresis loop of a many ferroelectrics, if $BiAlO_3$ has a high Curie point and large polarization as predicted, small additions of La^{3+} may not prevent a $Bi_xLa_{1-x}AlO_3$ solid solution from being technically useful.

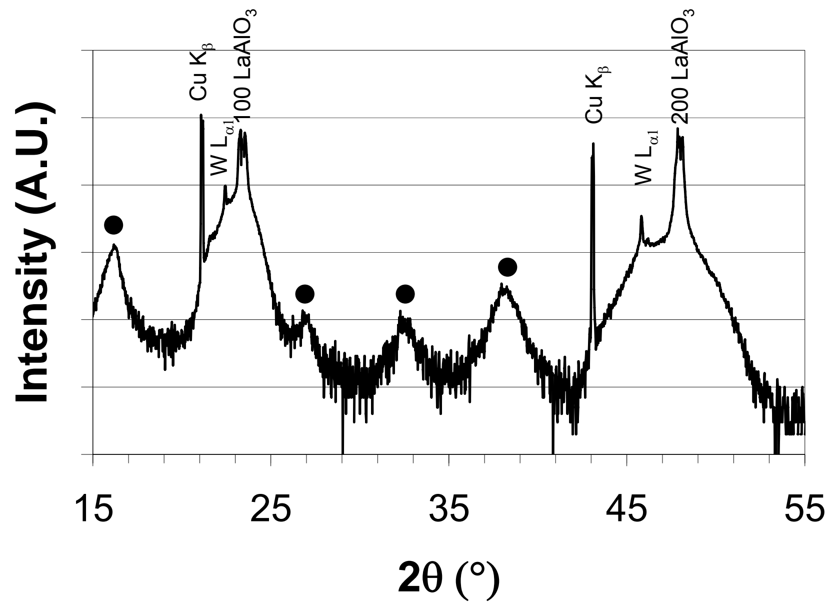

Fig. 5.2. X-ray diffraction pattern for a $0.9BiAlO_3$-$0.1PbTiO_3$ thin film on (100) $LaAlO_3$. Circles represent film peaks.

6.0 References

1. Lines, M.E. and A.M. Glass, *Principles and Applications of Ferroelectrics and Related Materials*. 1977, Oxford, NY: Oxford University Press. 680.

2. Burfoot, J.C. and G.W. Taylor, *Polar Dielectrics and Their Applications*. 1979, Berkeley and Los Angeles, California: University of California Press. 465.

3. Takasu, H., *The ferroelectric memory and its applications.* Journal of Electroceramics, 2000. **4**(2-3): p. 327.

4. Dimos, D., S.J. Lockwood, R.W. Schwartz, and M.S. Rodgers, *Thin-Film Decoupling Capacitors for Multichip Modules.* IEEE Transactions on Components Packaging and Manufacturing Technology Part A, 1995. **18**(1): p. 174.

5. Waffenschmidt, E., B. Ackermann, and J.A. Ferreira, *Design method and material technologies for passives in printed circuit board embedded circuits.* IEEE Transactions on Power Electronics, 2005. **20**(3): p. 576.

6. Scott, J.F., *New developments on FRAMs: [3D] structures and all-perovskite FETs.* Materials Science and Engineering B-Solid State Materials for Advanced Technology, 2005. **120**(1-3): p. 6.

7. Maeder, M.D., D. Damjanovic, and N. Setter, *Lead free piezoelectric materials.* Journal of Electroceramics, 2004. **13**(1-3): p. 385.

8. Zhang, S.J., C. Stringer, R. Xia, S.M. Choi, C.A. Randall, and T.R. Shrout, *Investigation of bismuth-based perovskite system: (1-x)*$Bi(Ni_{2/3}Nb_{1/3})O_3$*-x*$PbTiO_3$. Journal of Applied Physics, 2005. **98**(3).

9. Eitel, R.E., C.A. Randall, T.R. Shrout, P.W. Rehrig, W. Hackenberger, and S.E. Park, *New high temperature morphotropic phase boundary piezoelectrics based on* $Bi(Me)O_3$-$PbTiO_3$ *ceramics.* Japanese Journal of Applied Physics Part 1-Regular Papers Short Notes & Review Papers, 2001. **40**(10): p. 5999.

10. Do, D.H., P.G. Evans, E.D. Isaacs, D.M. Kim, C.B. Eom, and E.M. Dufresne, *Structural visualization of polarization fatigue in epitaxial ferroelectric oxide devices.* Nature Materials, 2004. **3**(6): p. 365.

11. Cross, L.E., *Materials Science - Lead-free at last.* Nature, 2004. **432**(7013): p. 24.

12. Shaw, T.M., S. Trolier-McKinstry, and P.C. McIntyre, *The properties of ferroelectric films at small dimensions.* Annual Review of Materials Science, 2000. **30**: p. 263.

13. Newnham, R.E., *Properties of Materials: Anisotropy, Symmetry, Structure*. 2005, Oxford, NY: Oxford University Press. 392.

14. Kao, K.C., *Dielectric Phenomena in Solids*. 2004, San Diego, California: Elsevier Academic Press. 579.

15. von Hippel, A.R., *Dielectrics and Waves*. 1962, New York: John Wiley & Sons, Inc. 267.

16. Jonscher, A.K., *Dielectric Relaxation in Solids.* Journal of Physics D-Applied Physics, 1999. **32**(14): p. R57.

17. Jona, F. and G. Shirane, *Ferroelectric Crystals*. 1993, Mineola, New York: Dover Publications, Inc. 402.

18. Smolenskii, G.A., V.A. Bokov, V.A. Isupov, N.N. Krainik, R.E. Pasynkov, and A.I. Sokolov, *Ferroelectrics and Related Materials*. Ferroelectricity and Related Phenomena, ed. G.W. Taylor. Vol. 3. 1984, New York, NY: Gordon and Breach Science Publishers. 763.

19. Ye, Z.G., *Crystal chemistry and domain structure of relaxor piezoerystals.* Current Opinion in Solid State & Materials Science, 2002. **6**(1): p. 35.

20. Bokov, A.A. and Z.G. Ye, *Recent progress in relaxor ferroelectrics with perovskite structure.* Journal of Materials Science, 2006. **41**(1): p. 31.

21. Bokov, A.A. and Z.G. Ye, *Phenomenological description of dielectric permittivity peak in relaxor ferroelectrics.* Solid State Communications, 2000. **116**(2): p. 105.

22. R. Waser, U.B., S. Tiedke, ed. *Polar Oxides: Properties, Characterization and Imaging*. 2005, John Wiley & Sons: New York.

23. Hubert, C., J. Levy, T.V. Rivkin, C. Carlson, P.A. Parilla, J.D. Perkins, and D.S. Ginley, *Nanopolar reorientation in ferroelectric thin films.* Applied Physics Letters, 2001. **79**(13): p. 2058.

24. Xu, G.Y., Z. Zhong, Y. Bing, Z.G. Ye, and G. Shirane, *Electric-field-induced redistribution of polar nano-regions in a relaxor ferroelectric.* Nature Materials, 2006. **5**(2): p. 134.

25. Cheng, Z.Y., R.S. Katiyar, X. Yao, and A.S. Bhalla, *Temperature dependence of the dielectric constant of relaxor ferroelectrics.* Physical Review B, 1998. **57**(14): p. 8166.

26. Zhang, Q.M. and J. Zhao, *Polarization responses in lead magnesium niobate based relaxor ferroelectrics.* Applied Physics Letters, 1997. **71**(12): p. 1649.

27. Viehland, D., J.F. Li, S.J. Jang, L.E. Cross, and M. Wuttig, *Dipolar-Glass Model for Lead Magnesium Niobate.* Physical Review B, 1991. **43**(10): p. 8316.

28. Damjanovic, D., *Ferroelectric, dielectric and piezoelectric properties of ferroelectric thin films and ceramics.* Reports on Progress in Physics, 1998. **61**(9): p. 1267.

29. Viehland, D. and J.F. Li, *Dependence of the Glasslike Characteristics of Relaxor Ferroelectrics on Chemical Ordering.* Journal of Applied Physics, 1994. **75**(3): p. 1705.

30. Cross, L.E., *Relaxor Ferroelectrics.* Ferroelectrics, 1987. **76**(3-4): p. 241.

31. Biegalski, M.D., Y. Jia, D.G. Schlom, S. Trolier-McKinstry, S.K. Streiffer, V. Sherman, R. Uecker, and P. Reiche, *Relaxor ferroelectricity in strained epitaxial $SrTiO_3$ thin films on $DyScO_3$ substrates.* Applied Physics Letters, 2006. **88**(19). 192907

32. Choi, K.J., M. Biegalski, Y.L. Li, A. Sharan, J. Schubert, R. Uecker, P. Reiche, Y.B. Chen, X.Q. Pan, V. Gopalan, L.Q. Chen, D.G. Schlom, and C.B. Eom, *Enhancement of ferroelectricity in strained $BaTiO_3$ thin films.* Science, 2004. **306**(5698): p. 1005.

33. Sutter, P., E. Sutter, P. Rugheimer, and M.G. Lagally, *Nanoscale strain and band structure engineering using epitaxial stressors on ultrathin silicon-on-insulator.* Surface Science, 2003. **532**: p. 789.

34. Li, Y.L., S. Choudhury, J.H. Haeni, M.D. Biegalski, A. Vasudevarao, A. Sharan, H.Z. Ma, J. Levy, V. Gopalan, S. Trolier-McKinstry, D.G. Schlom, Q.X. Jia, and L.Q. Chen, *Phase transitions and domain structures in strained pseudocubic (100) $SrTiO_3$ thin films.* Physical Review B, 2006. **73**(18). 184112

35. Parker, C.B., J.P. Maria, and A.I. Kingon, *Temperature and thickness dependent permittivity of $(Ba,Sr)TiO_3$ thin films.* Applied Physics Letters, 2002. **81**(2): p. 340.

36. Kelman, M.B., P.C. McIntyre, A. Gruverman, B.C. Hendrix, S.M. Bilodeau, and J.F. Roeder, *Origin and implications of the observed rhombohedral phase in nominally tetragonal $Pb(Zr_{0.35}Ti_{0.65})O_3$ thin films.* Journal of Applied Physics, 2003. **94**(8): p. 5210.

37. Zhang, Q.M., H.S. Xu, F. Fang, Z.Y. Cheng, F. Xia, and H. You, *Critical thickness of crystallization and discontinuous change in ferroelectric behavior with thickness in ferroelectric polymer thin films.* Journal of Applied Physics, 2001. **89**(5): p. 2613.

38. Zhou, C. and D.M. Newns, *Intrinsic dead layer effect and the performance of ferroelectric thin film capacitors.* Journal of Applied Physics, 1997. **82**(6): p. 3081.

39. Nino, J.C., H.J. Youn, M.T. Lanagan, and C.A. Randall, *Bi_2O_3 solubility of Bi-based pyrochlores and related phases.* Journal of Materials Research, 2002. **17**(5): p. 1178.

40. Lu, J.W., Z.Q. Chen, T.R. Taylor, and S. Stemmer, *Composition control and dielectric properties of bismuth zinc niobate thin films synthesized by radio-frequency magnetron sputtering.* Journal of Vacuum Science & Technology A, 2003. **21**(5): p. 1745.

41. Thayer, R.L., *Bismuth zinc niobate films for dielectric applications*, Master of Science thesis in Materials Science and Engineering. 2002, The Pennsylvania State University: University Park, PA, p. 79

42. Thayer, R.L., C.A. Randall, and S. Trolier-McKinstry, *Medium permittivity bismuth zinc niobate thin film capacitors.* Journal of Applied Physics, 2003. **94**(3): p. 1941.

43. Maria, J.P., *Deposition and Measurement of Epitaxial Barium Titante thin films using conductive epitaxial oxide electrodes prepared by pulsed laser deposition*, Master of Science thesis in Materials Science and Engineering. 1996, The Pennsylvania State University: University Park, PA, p. 145

44. Jaffe, B., W.R. Cook Jr., and H. Jaffe, *Piezoelectric Ceramics*. 1971, New York: Academic Press Ltd. 317.

45. Theis, C.D., *Investigation of growth and domain structure of epitaxial lead titanate thin films*, Master of Science thesis in Department of Materials Science and Engineering. 1996, The Pennsylvania State University: University Park, PA, p. 114

46. Maria, J.P., S. Trolier-McKinstry, D.G. Schlom, M.E. Hawley, and G.W. Brown, *The influence of energetic bombardment on the structure and properties of epitaxial $SrRuO_3$ thin films grown by pulsed laser deposition.* Journal of Applied Physics, 1998. **83**(8): p. 4373.

47. Inaguma, Y., A. Miyaguchi, M. Yoshida, T. Katsumata, Y. Shimojo, R.P. Wang, and T. Sekiya, *High-pressure synthesis and ferroelectric properties in perovskite-type $BiScO_3$-$PbTiO_3$ solid solution.* Journal of Applied Physics, 2004. **95**(1): p. 231.

48. *An American National Standard IEEE Standard Definitions of Terms Associated with Ferroelectric and Related Materials.* IEEE Transactions on Ultrasonics, Ferroelectrics, and Frequency Control, 2003. **50**(12): p. 1.

49. Noheda, B., J.A. Gonzalo, L.E. Cross, R. Guo, S.E. Park, D.E. Cox, and G. Shirane, *Tetragonal-to-monoclinic phase transition in a ferroelectric perovskite: The structure of $PbZr_{0.52}Ti_{0.48}O_3$.* Physical Review B, 2000. **61**(13): p. 8687.

50. Saito, Y., H. Takao, T. Tani, T. Nonoyama, K. Takatori, T. Homma, T. Nagaya, and M. Nakamura, *Lead-free piezoceramics.* Nature, 2004. **432**(7013): p. 84.

51. Nino, J.C. and S. Trolier-McKinstry, *Dielectric, ferroelectric, and piezoelectric properties of (001) $BiScO_3$-$PbTiO_3$ epitaxial films near the morphotropic phase boundary.* Journal of Materials Research, 2004. **19**(2): p. 568.

52. Seshadri, R. and N.A. Hill, *Visualizing the role of Bi 6s "Lone pairs" in the off-center distortion in ferromagnetic $BiMnO_3$.* Chemistry of Materials, 2001. **13**(9): p. 2892.

53. Ang, C. and Z. Yu, *Dielectric relaxor and ferroelectric relaxor: Bi-doped paraelectric $SrTiO_3$.* Journal of Applied Physics, 2002. **91**(3): p. 1487.

54. Samara, G.A., *Relaxor properties of compositionally disordered perovskites: Ba- and Bi-substituted $Pb(Zr_{1-x}Ti_x)O_3$.* Physical Review B, 2005. **71**(22).

55. Bahri, F., A. Simon, H. Khemakhem, and J. Ravez, *Classical or relaxor ferroelectric behaviour of ceramics with composition $Ba_{1-x}Bi_{2x/3}TiO_3$.* Physica Status Solidi a-Applied Research, 2001. **184**(2): p. 459.

56. Zhou, L.Q., P.M. Vilarinho, and J.L. Baptista, *Dielectric properties of bismuth doped $Ba_{1-x}Sr_xTiO_3$ ceramics.* Journal of the European Ceramic Society, 2001. **21**(4): p. 531.

57. Simon, A., J. Ravez, and M. Maglione, *Relaxor properties of $Ba_{0.9}Bi_{0.067}(Ti_{1-x}Zr_x)O_3$ ceramics.* Solid State Sciences, 2005. **7**(8): p. 925.

58. Tomashpolskii, I.J., Venevtse.In, and G.S. Zhdanov, *Electron Diffraction Study of $BiFeO_3$ Crystals.* Doklady Akademii Nauk Sssr, 1963. **153**(6): p. 1313.

59. Tomashpolskii.Yy, E.V. Zubova, K.P. Burdina, and Venevtse.Yn, *X-Ray Investigation of New Perovskites Formed at High Pressures.* Soviet Physics Crystallography, Ussr, 1969. **13**(6): p. 859.

60. Tomashpolskii, Y.Y. and Y.N. Venevtsev, *Electrical and Magnetic Properties of Perovskites Obtained at High Pressures.* Neoganicheskie Meterialy, 1969. **7**(7): p. 1279.

61. Venevtsev, Y.M., G.S. Zhdanov, S.N. Solov'ev, E.V. Bezus, V.V. Ivanov, S.A. Fedulov, and A.G. Kapyshev, *Crystal Chemical Studies of Substances with Perovskite Type Structure and Special Dielectric Properties.* Kristallografiya, 1960. **5**(4): p. 620.

62. Baettig, P., C.F. Schelle, R. LeSar, U.V. Waghmare, and N.A. Spaldin, *Theoretical prediction of new high-performance lead-free piezoelectrics.* Chemistry of Materials, 2005. **17**(6): p. 1376.

63. Buhrer, C.F., *Some Properties of Bismuth Perovskites.* Journal of Chemical Physics, 1962. **36**(3): p. 798.

64. Belik, A.A., T. Wuernisha, T. Kamiyama, K. Mori, M. Maie, T. Nagai, Y. Matsui, and E. Takayama-Muromachi, *High-pressure synthesis, crystal structures, and properties of perovskite-like $BiAlO_3$ and pyroxene-like $BiGaO_3$.* Chemistry of Materials, 2006. **18**(1): p. 133.

65. Belik, A.A., S.Y. Stefanovich, B.I. Lazoryak, and E. Takayama-Muromachi, *$BiInO_3$: A polar oxide with $GdFeO_3$-type perovskite structure.* Chemistry of Materials, 2006. **18**(7): p. 1964.

66. Belik, A.A., S. Iikubo, K. Kodama, N. Igawa, S. Shamoto, S. Niitaka, M. Azuma, Y. Shimakawa, M. Takano, F. Izumi, and E. Takayama-Muromachi, *Neutron powder diffraction study on the crystal and magnetic structures of $BiCoO_3$.* Chemistry of Materials, 2006. **18**(3): p. 798.

67. Belik, A.A., S. Iikubo, K. Kodama, N. Igawa, S. Shamoto, M. Maie, T. Nagai, Y. Matsui, S.Y. Stefanovich, B.I. Lazoryak, and E. Takayama-Muromachi, *$BiScO_3$: Centrosymmetric $BiMnO_3$-type oxide.* Journal of the American Chemical Society, 2006. **128**(3): p. 706.

68. Eerenstein, W., F.D. Morrison, J.F. Scott, and N.D. Mathur, *Growth of highly resistive $BiMnO_3$ films.* Applied Physics Letters, 2005. **87**(10).

69. Wang, J., J.B. Neaton, H. Zheng, V. Nagarajan, S.B. Ogale, B. Liu, D. Viehland, V. Vaithyanathan, D.G. Schlom, U.V. Waghmare, N.A. Spaldin, K.M. Rabe, M. Wuttig, and R. Ramesh, *Epitaxial $BiFeO_3$ multiferroic thin film heterostructures.* Science, 2003. **299**(5613): p. 1719.

70. Pradhan, A.K., K. Zhang, D. Hunter, J.B. Dadson, G.B. Loiutts, P. Bhattacharya, R. Katiyar, J. Zhang, D.J. Sellmyer, U.N. Roy, Y. Cui, and A. Burger, *Magnetic and electrical properties of single-phase multiferroic $BiFeO_3$.* Journal of Applied Physics, 2005. **97**(9).

71. Okada, M., T. Yoshimura, A. Ashida, and N. Fujimura, *Synthesis of $Bi(Fe_xAl_{1-x})O_3$ thin films by pulsed laser deposition and its structural characterization.* Japanese Journal of Applied Physics Part 1-Regular Papers Short Notes & Review Papers, 2004. **43**(9B): p. 6609.

72. Niitaka, S., M. Azuma, M. Takano, E. Nishibori, M. Takata, and M. Sakata, *Crystal structure and dielectric and magnetic properties of $BiCrO_3$ as a ferroelectromagnet.* Solid State Ionics, 2004. **172**(1-4): p. 557.

73. Hill, N.A., P. Battig, and C. Daul, *First principles search for multiferroism in $BiCrO_3$.* Journal of Physical Chemistry B, 2002. **106**(13): p. 3383.

74. Smith, D.L., *Thin-Film Deposition: Principles & Practice*. 1995: McGraw-Hill, Inc. 616.

75. Ohring, M., *Materials Science of Thin Films: Deposition & Structure*. 2002, San Diego, CA: Academic Press. 794.

76. Campbell, S.A., *The Science and Engineering of Microelectronic Fabrication*. 2nd ed. 2001, Oxford, New York: Oxford University Press. 603.

77. Seshan, K., ed. *Handbook of Thin Film Deposition Processes and Techniques.* 2nd ed. 2002, Noyes Publications: Norwich, New York, U.S.A. 629.

78. Chrisey, D.B. and G.K. Hubler, eds. *Pulsed Laser Deposition of Thin Films*. 1994, John Wiley & Sons, Inc.: New York. 613.

79. Geohegan, D.B., *Fast Intensified-CCD Photography of $YBa_2Cu_3O_{7-X}$ Laser Ablation in Vacuum and Ambient Oxygen.* Applied Physics Letters, 1992. **60**(22): p. 2732.

80. Edge, L.F., *Pulsed laser deposition of bismuth zinc niobate thin films for dielectric applications*, Master of Science thesis in Materials Science and Engineering. 2002, The Pennsylvania State University: University Park, PA, p. 116

81. Strikovsky, M.D., E.B. Klyuenkov, S.V. Gaponov, J. Schubert, and C.A. Copetti, *Crossed Fluxes Technique for Pulsed-Laser Deposition of Smooth* $YBa_2Cu_3O_{7-X}$ *Films and Multilayers.* Applied Physics Letters, 1993. **63**(8): p. 1146.

82. Jeong, Y.S., S.Y. Lee, H.K. Jang, I.S. Yang, S.H. Moon, and B. Oh, *Surface modification of laser ablated YBCO target.* Applied Surface Science, 1997. **110**: p. 424.

83. Mo, Y.W. and M.G. Lagally, *Scanning Tunneling Microscopy Studies of the Growth-Process of Ge on Si(001).* Journal of Crystal Growth, 1991. **111**(1-4): p. 876.

84. Fujikawa, Y., K. Akiyama, T. Nagao, T. Sakurai, M.G. Lagally, T. Hashimoto, Y. Morikawa, and K. Terakura, *Origin of the stability of Ge(105) on Si: A new structure model and surface strain relaxation.* Physical Review Letters, 2002. **88**(17). 176101

85. Li, C.L., D.F. Cui, Y.L. Zhou, H.B. Lu, Z.H. Chen, D.F. Zhang, and F. Wu, *Asymmetric rocking curve study of the crystal structure orientations for* $BaTiO_3$ *thin films grown by pulsed laser deposition.* Applied Surface Science, 1998. **136**(3): p. 173.

86. Emelyanov, A.Y., N.A. Pertsev, and A.L. Kholkin, *Effect of external stress on ferroelectricity in epitaxial thin films.* Physical Review B, 2002. **66**(21). 214108

87. Gruverman, A., B.J. Rodriguez, A.I. Kingon, R.J. Nemanich, A.K. Tagantsev, J.S. Cross, and M. Tsukada, *Mechanical stress effect on imprint behavior of integrated ferroelectric capacitors.* Applied Physics Letters, 2003. **83**(4): p. 728.

88. Viehland, D., *Effect of uniaxial stress upon the electromechanical properties of various piezoelectric ceramics and single crystals.* Journal of the American Ceramic Society, 2006. **89**(3): p. 775.

89. Taylor, T.R., P.J. Hansen, B. Acikel, N. Pervez, R.A. York, S.K. Streiffer, and J.S. Speck, *Impact of thermal strain on the dielectric constant of sputtered barium strontium titanate thin films.* Applied Physics Letters, 2002. **80**(11): p. 1978.

90. Vinci, R.P. and J.J. Vlassak, *Mechanical behavior of thin films.* Annual Review of Materials Science, 1996. **26**: p. 431.

91. Thompson, C.V., *Structure evolution during processing of polycrystalline films.* Annual Review of Materials Science, 2000. **30**: p. 159.

92. Kwok, H.S., H.S. Kim, D.H. Kim, W.P. Shen, X.W. Sun, and R.F. Xiao, *Correlation between plasma dynamics and thin film properties in pulsed laser deposition.* Applied Surface Science, 1997. **110**: p. 595.

93. Norton, D.P., C. Park, J.D. Budai, S.J. Pennycook, and C. Prouteau, *Plume-induced stress in pulsed-laser deposited CeO_2 films.* Applied Physics Letters, 1999. **74**(15): p. 2134.

94. Warren, B.E., *X-ray Diffraction*. 1990, Mineola, NY: Dover Publications Inc. 381.

95. Pietsch, U., V. Holy, and T. Baumbach, *High Resolution X-ray Scattering: From thin films to lateral nanostructures*. 2004, New York, NY: Springer-Verlag. 408.

96. Shannon, R.D., *Revised Effective Ionic-Radii and Systematic Studies of Interatomic Distances in Halides and Chalcogenides.* Acta Crystallographica Section A, 1976. **32**(Sep1): p. 751.

97. Speranskaya, E.I.S., V. M.; Safronov, G. M.; Gaidukov, E. N., *Bismuth oxide-aluminum oxide system.* Neorganicheskie Materialy, 1970. **6**(7): p. 1364.

98. Maffei, N., *Excimer laser ablated bismuth titante thin films for nondestructive readout nonvolatile memory applications*, Ph.D. thesis in Materials Science and Engineering. 1993, The Pennsylvania State University: University Park, PA, p. 169

99. Nelson, J.B. and D.P. Riley, *An Experimental Investigation of Extrapolation Methods in the Derivation of Accurate Unit-Cell Dimensions of Crystals.* Proceedings of the Physical Society of London, 1945. **57**(321): p. 160.

100. Hur, N., S.W. Cheong, S.N. Kale, S.B. Ogale, R. Choudhary, S.R. Shinde, and T. Venkatesan, *Substrate-induced epitaxial mixing of bulk-immiscible $La_{5/8}Sr_{3/8}MnO_3/LuMnO_3$ films.* Applied Physics Letters, 2005. **86**(11). 112507

101. Simon, W.K., E.K. Akdogan, and A. Safari, *Anisotropic strain relaxation in $(Ba_{0.6}Sr_{0.4})TiO_3$ epitaxial thin films.* Journal of Applied Physics, 2005. **97**(10). 103530

102. Chen, A., Z. Yu, J. Scott, A. Loidl, R. Guo, A.S. Bhalla, and L.E. Cross, *Dielectric polarization processes in Bi: $SrTiO_3$.* Journal of Physics and Chemistry of Solids, 2000. **61**(2): p. 191.

103. Ravez, J. and A. Simon, *New lead-free relaxor ceramics derived from $BaTiO_3$ by cationic heterovalent substitutions in the 12 CN crystallographic site.* Solid State Sciences, 2000. **2**(5): p. 525.

104. Stringer, C.J., T.R. Shrout, C.A. Randall, and I.M. Reaney, *Classification of transition temperature behavior in ferroelectric $PbTiO_3$-Bi(Me',Me'')O_3 solid solutions.* Journal of Applied Physics, 2006. **99**(2). 024106

105. Ohly, C., S. Hoffmann-Eifert, K. Szot, and R. Waser, *Electrical conductivity and segregation effects of doped $SrTiO_3$ thin films.* Journal of the European Ceramic Society, 2001. **21**(10-11): p. 1673.

106. Baniecki, J.D., J.S. Cross, M. Tsukada, and J. Watanabe, *H_2O vapor-induced leakage degradation of Pb(Zr,Ti)O_3 thin-film capacitors with Pt and IrO_2 electrodes.* Applied Physics Letters, 2002. **81**(20): p. 3837.

107. Lokhande, C.D. and C.H. Bhosale, *Characterisation of chemically converted sprayed Bi_2O_3 to Bi_2S_3 thin films.* Materials Chemistry and Physics, 1997. **49**(1): p. 46.

108. Harwig, H.A. and A.G. Gerards, *Electrical-Properties of Alpha, Beta, Gamma and Delta Phases of Bismuth Sesquioxide.* Journal of Solid State Chemistry, 1978. **26**(3): p. 265.

109. Haun, M.J., *Thermodynamic theory of the lead zirconate-titante solid solution system*, Ph.D. thesis in Solid State Science. 1988, The Pennsylvania State University: University Park, PA, p. 158

110. Donnelly, N.J., *Dielectric and electromechanical properties of PMN-PT thin films*, Ph. D. thesis in Department of Pure and Applied Physics. 2004, Queens University: Belfast, Ireland, p. 143

111. Viehland, D., S.J. Jang, L.E. Cross, and M. Wuttig, *Freezing of the Polarization Fluctuations in Lead Magnesium Niobate Relaxors.* Journal of Applied Physics, 1990. **68**(6): p. 2916.

112. Trolier-McKinstry, S., L.E. Cross, and Y. Yamashita, eds. *Piezoelectric Single Crystals and Their Applications*. 2004: University Park, PA.

113. Kamba, S., V. Bovtun, J. Petzelt, I. Rychetsky, R. Mizaras, A. Brilingas, J. Banys, J. Grigas, and M. Kosec, *Dielectric dispersion of the relaxer PLZT ceramics in the frequency range 20 Hz-100 THz.* Journal of Physics-Condensed Matter, 2000. **12**(4): p. 497.

114. Yu, Z., C. Ang, R.Y. Guo, and A.S. Bhalla, *Ferroelectric-relaxor behavior of* $Ba(Ti_{0.7}Zr_{0.3})O_3$ *ceramics.* Journal of Applied Physics, 2002. **92**(5): p. 2655.

115. Ang, C., Z. Jing, and Z. Yu, *Ferroelectric relaxor* $Ba(Ti,Ce)O_3$. Journal of Physics-Condensed Matter, 2002. **14**(38): p. 8901.

116. Lambert, M. and R. Comes, *Chain Structure and Phase Transition of* $BaTiO_3$ *and* $KNbO_3$. Solid State Communications, 1969. **7**(2): p. 305.

117. Zhao, Z., V. Buscaglia, M. Viviani, M.T. Buscaglia, L. Mitoseriu, A. Testino, M. Nygren, M. Johnsson, and P. Nanni, *Grain-size effects on the ferroelectric behavior of dense nanocrystalline* $BaTiO_3$ *ceramics.* Physical Review B, 2004. **70**(2).

118. Ring, K.M. and K.L. Kavanagh, *Substrate effects on the ferroelectric properties of fine-grained* $BaTiO_3$ *films.* Journal of Applied Physics, 2003. **94**(9): p. 5982.

119. Huang, G.F. and S. Berger, *Combined effect of thickness and stress on ferroelectric behavior of thin* $BaTiO_3$ *films.* Journal of Applied Physics, 2003. **93**(5): p. 2855.

120. Zembilgotov, A.G., N.A. Pertsev, H. Kohlstedt, and R. Waser, *Ultrathin epitaxial ferroelectric films grown on compressive substrates: Competition between the surface and strain effects.* Journal of Applied Physics, 2002. **91**(4): p. 2247.

121. Kretschmer, R. and K. Binder, *Surface Effects on Phase-Transitions in Ferroelectrics and Dipolar Magnets.* Physical Review B, 1979. **20**(3): p. 1065.

122. Vendik, O.G., S.P. Zubko, and L.T. Ter-Martirosayn, *Experimental evidence of the size effect in thin ferroelectric films.* Applied Physics Letters, 1998. **73**(1): p. 37.

123. Seshadri, R., *Lone pairs in insulating pyrochlores: Ice rules and high-k behavior.* Solid State Sciences, 2006. **8**(3-4): p. 259.

124. Tuttle, B.A., P. Yang, J.H. Gieske, J.A. Voigt, T.W. Scofield, D.H. Zeuch, and W.R. Olson, *Pressure-induced phase transformation of controlled-porosity* $Pb(Zr_{0.95}Ti_{0.05})O_3$ *ceramics.* Journal of the American Ceramic Society, 2001. **84**(6): p. 1260.

125. Brennecka, G.L., W. Huebner, B.A. Tuttle, and P.G. Clem, *Use of stress to produce highly oriented tetragonal lead zirconate titanate (PZT 40/60) thin films and resulting electrical properties.* Journal of the American Ceramic Society, 2004. **87**(8): p. 1459.

126. Naray-Szabo, I., *The Perovskite Structure Family.* Meugyetemi Kozlemenyek, 1947. **1**(30): p. 30.